COSMOLOGY USING GALAXY CLUSTER PECULIAR VELOCITIES

by

Suman Bhattacharya

B.Sc. in Physics, Calcutta University, India, 2000

M.Sc. in Physics, IIT Kanpur, India, 2003

Submitted to the Graduate Faculty of

the Department of Physics & Astronomy in partial fulfillment

of the requirements for the degree of

Doctor of Philosophy

University of Pittsburgh

2008

UNIVERSITY OF PITTSBURGH

DEPARTMENT OF PHYSICS & ASTRONOMY

This dissertation was presented

by

Suman Bhattacharya

It was defended on

August 14th 2008

and approved by

Arthur Kosowsky, University of Pittsburgh

David Turnshek, University of Pittsburgh

Vladimir Savinov, University of Pittsburgh

Daniel Boyanovsky, University of Pittsburgh

Andrew Zentner, University of Pittsburgh

Joseph Mohr, University of Illinois at Urbana-Champaign

Dissertation Director: Arthur Kosowsky, University of Pittsburgh

COSMOLOGY USING GALAXY CLUSTER PECULIAR VELOCITIES

Suman Bhattacharya, PhD

University of Pittsburgh, 2008

Future multi-frequency microwave background experiments with arcminute resolution and micro-Kelvin temperature sensitivity will be able to detect the kinetic Sunyaev-Zeldovich effect, providing a way to measure radial (line-of-sight) peculiar velocities of massive galaxy clusters. We show that measurement of cluster peculiar velocities have the potential to constrain several dark energy parameters. We also compare cluster peculiar velocities with other dark energy probes: the eventual constraints from radial peculiar velocity measurements on the dark energy parameters are comparable to constraints from supernovae measurements, and better than cluster counts and baryon acoustic oscillations; adding radial peculiar velocity to other dark energy probes improves constraints on the figure of merit by more than a factor of two.

We also study the impact of the mass-observable relation (i.e the relation between the observed Sunyaev-Zeldovich flux and the mass of the galaxy cluster) and other systematic errors on cluster radial peculiar velocities. We find that cluster radial peculiar velocities closely trace the large-scale peculiar velocity field independent of cluster mass. On the other hand, cluster radial peculiar velocity determinations are complicated by microwave emission from dusty galaxies and radio sources, which may be correlated with clusters. Systematic errors due to these factors can give substantial biases in determination of dark energy parameters, although radial peculiar velocity surveys will contain enough information that the errors can be modeled using the data itself, with little degradation in cosmological constraints.

An alternative to using the galaxy cluster radial peculiar velocity field directly is the

cluster momentum distribution. Dark-matter cosmological simulations can provide the total cluster momentum distribution, while the Sunyaev-Zeldovich effect gives the baryon momentum. Thus, to better understand the cluster momentum distribution, we study the effect of quasar feedback on the baryon fraction in galaxy groups using high-resolution numerical simulations. For a sample of ten galaxy group-sized dark matter halos , the total gas fraction in the two simulations generally differs by less than 10%. We conclude that the quasar feedback do not add any significant systematic errors to the cluster momentum.

keywords: Cosmology: theory, Cosmology: Sunyaev-Zeldovich effect, cosmological parameters, galaxies: clusters, velocity, statistics.

TABLE OF CONTENTS

LIST OF FIGURES

PREFACE

1.0 INTRODUCTION

One of the greatest triumphs of cosmology has been a precise determination of the parameters defining the standard cosmological model, primarily via the cosmic microwave background fluctuations combined with the large-scale distribution of galaxies and the distance-redshift relation of distant supernovae. Future datasets, with higher precision, will provide tighter constraints on the cosmological parameters, along with strong consistency checks of the cosmological model.

The current standard model of the universe consists of about 5% visible matter or baryons and the rest as "dark" components, namely the "dark matter" and the "dark energy". The dark matter is composed of matter which interacts only gravitationally, and possibly via weak interactions, with the visible matter, making their detection a rather stiff challenge. The dark energy is not even composed of matter but must explain the observed acceleration of the universe's expansion at recent epochs.

Understanding the cause of this acceleration is of fundamental importance to physics. It might be due to the presence of an exotic component of the universe's stress-enegy tensor exerting pressure to cause this acceleration, or it might be due to the breakdown of general relativity at cosmological scales. Given the lack of current theoretical understanding, it is imperative to understand the nature of dark energy or modified gravity in a phenomenological manner, namely constraining parameters that describe dark energy or modified gravity. Although the current data from the cosmic microwave background, large scale structure, and supernova distance measurements (Spergel et al., 2003, 2007; Dunkley et al., 2008; Tegmark et al., 2001) constrain many parameters, they do not yet provide tight constraints on the dark energy equation of state. The 1-σ constraint on the dark energy equation of state at the current epoch is around 10%, while the current observational data do not put

any meaningful constraints on the evolution of the dark energy equation of state.

1.1   DARK ENERGY PROBES

In order to refine our knowledge of the standard model of cosmology and in particular of dark energy, we want to measure both the expansion history of the universe and the growth of structures via gravitational instability. This is especially important for distinguishing between the dark energy and the modified gravity scenario: both dark energy and modified gravity can have the same expansion history, but they will then have different observational signatures from the growth of structure.

The expansion history of the universe is measured using type Ia supernovae as standard candles, or by measuring the baryon features imprinted on the matter power spectrum due to baryon oscillations in the early universe. On the other hand, probes for measuring the history of structure growth are mostly the matter power spectrum of galaxies, galaxy clusters, and hydrogen via the Lyman-alpha forest. The Lyman-alpha forest measures the clustering of baryons at smaller scales; the measurements depends somewhat on non-linear physics which is difficult to model. The galaxy power spectrum depends on the accuracy of the measurement of the mass-to-light ratio and the associated bias. Galaxy clusters probe mostly linear scales and hence are not prone to many of the systematics affecting galaxies, but because of their scarcity, the power spectrum measurement is dominated by shot noise. Weak gravitational lensing of background galaxies by the large scale structure is perhaps the most promising way to measure the growth history. Lensing is due to the deflection of light by the total matter distribution and hence is independent of the uncertainty in mass-to-light ratio. However, lensing is sensitive to uncertainty in the redshift distribution of source galaxies, and to baryonic effects in the matter power spectrum (Rudd et al., 2008).

1.2   THE SUNYAEV-ZELDOVICH EFFECT

The Sunyaev-Zeldovich Effect (SZ effect hereafter) (Sunyaev and Zeldovich, 1980) is another probe that can provide interesting constraints on a number of cosmological parameters. The SZ effect is a distortion of the primary cosmic microwave background radiation (CMB) caused by the inverse Thomson scattering of the CMB photons by hot electrons present in the large scale structure. The SZ effect has two components, the thermal SZ effect (tSZ effect hereafter) and the kinetic SZ effect (kSZ effect hereafter). The tSZ effect is a spectral distortion which is negative below 220 GHz, reaches a "null" at 218 GHz (in the limit of nonrelativistic electrons) and becomes positive above 220 GHz. The kSZ effect is essentially a Doppler shift caused by the bulk motion of the electrons with respect to the CMB rest frame and has a blackbody spectrum. Galaxy clusters, which have the largest concentrations of hot electrons in the universe, are the dominant sources of SZ distortions and the particular source focused on here.

Note that the "SZ null" is independent of cluster physics only under the assumption that the energy transfer between the CMB photons and the hot electrons are small, the electron distribution is non-relativistic and that the diffusion approximation is valid. However, even for massive clusters, the optical depth is small (≈ 0.01) and hence the diffusion approximation is not valid and also the electron velocities are near relativistic. Because of these reasons, the "SZnull" is known to depend on the cluster temperature.

The SZ distortion, both the kinetic and the thermal components, depends on redshift only via the angular diameter distance of the galaxy clusters, which is nearly constant for galaxy clusters with $z \geq 1$. This property makes the SZ effect an ideal tool for detecting galaxy clusters. One can essentially detect all the clusters larger than a certain mass limit over the entire cosmological volume via their SZ signature. Ongoing and future surveys like the Atacama Cosmology Telescope (ACT) (Kosowsky, 2006), the South Pole Telescope (SPT) (Ruhl et al., 2004) and the Planck satellite are going to detect thousands of galaxy clusters over a large sky area.

Cluster counts above a certain mass threshold as a function of redshift depend on the growth history and the expansion history of the universe (Holder et al., 2001). The cluster

mass function depends exponentially on the growth history of the universe, which makes cluster counts a promising dark energy probe. Most of the current microwave surveys of arcminute resolution are designed to detect clusters and constrain dark energy. Cluster counts, however, suffer from a potential systematic error, namely the "mass-observable" relation. An SZ experiment does not detect cluster mass directly; rather it measures the SZ flux due to the gas in the cluster, proportional to the product of electron optical depth and electron temperature. The relation between SZ flux and cluster mass is studied through simulations, which are only an approximation of the actual universe. The fraction of gas mass in clusters depends partly on complicated non-linear physics like star formation and quasar feedback. Moreover, the relation between the SZ flux and the mass needs to be understood to better than 5% in order to reduce the systematic error in dark energy parameters below the level of statistical errors for anticipated surveys (Francis et al., 2005).

1.3   CLUSTER RADIAL PECULIAR VELOCITIES

In the early universe, the matter distribution was smooth with tiny density fluctuations compared to the average density of matter. As the universe expanded, these fluctuations grew due to gravity and collapsed to form galaxies, galaxy clusters, filaments and other structures. The separation of these structures increase with the expansion of the universe, but they also have an extra component of velocity induced by gravitation known as peculiar velocity; this is the velocity with respect to the local rest frame of the microwave radiation.

Measurement of radial peculiar velocities can provide important information about the dynamics of structure formation complementary to probes of local matter density. If the amount of dark energy is greater in the late universe, then it will slow the growth of structure and reduce the radial peculiar velocities at which structures fall towards each other. Thus measuring the radial peculiar velocities of large-scale structures (galaxy clusters in the present context) in turn provides a handle on the amount of dark energy and its evolution.

So far, most of the work related to radial peculiar velocities has been focused on galaxies. One measures the redshift z of a galaxy, which is proportional to the Hubble flow plus

the velocity with which the galaxy is moving with respect to the local Hubble flow: $cz = H_0 d + v_{\mathrm{pec}}$ (valid for small z). So in order to measure the radial peculiar velocity v_{pec}, an independent measurement of the distance (d) to the galaxy is required. The radial peculiar velocity of the galaxy can then be measured by subtracting the Hubble flow component, determined by its distance, from the total redshift (assuming that the Hubble parameter $H_0 = 100h$ km/s/Mpc with $h = 0.7$ is known perfectly). However, the error in traditional galaxy distance measurements increases dramatically with redshift, restricting the galaxy radial peculiar velocity measurements only within the local Hubble flow of redshift ~ 0.1. Using supernovae standard candles to measure galaxy distances is more promising, but so far the samples of supernovae suitable for this purpose are too small to give statistically powerful measurements of galaxy velocities.

The kSZ effect, which is directly proportional to the radial peculiar velocity, provides an alternative way to measure the radial peculiar velocity field. The kSZ signal is independent of the redshift, so radial peculiar velocity derived from the measurement of the kSZ effect has a redshift-independent measurement error, unlike the distance measurements in the traditional redshift-based radial peculiar velocity surveys. However, kSZ is a small signal (typically a few μK) and spectrally indistinguishable from the primary CMB anisotropy (around 100 μK), which makes this measurement a challenging observational effort. The tSZ component, which is 10 times bigger than the kSZ, also acts as a dominant source of error for kSZ detection. However, the tSZ signal becomes zero at around 220 GHz, which makes it possible to separate the thermal and the kinetic components. The other sources of noise, which make the kSZ measurement difficult are high-redshift dusty galaxies and radio sources, which have significant emission at relevant microwave frequencies. These can be distinguished spectrally from the kSZ signal, but this requires challenging high-resolution and high-sensitivity observations. So far, only upper limits on cluster radial peculiar velocities have been established for a handful of clusters (Benson et al., 2003).

Current experiments like the ACT and the SPT have arcminute angular resolution and the nominal sensitivity to measure the kSZ effect. Numerical studies (Diaferio et al., 2005a; Knox et al., 2004) have shown that a multi-frequency SZ experiment with arcminute resolution and few μK sensitivity will be able to measure cluster radial peculiar velocities with

a typical error of 200-300 km/s. Internal motions of the intracluster medium give an irreducible random error of around 100 km/s (Nagai et al., 2003). The ACT collaboration foresees maps of sufficient raw sensitivity to measure the kSZ effect in many clusters, making detailed studies of the cosmological impact of future kSZ measurements timely. Some recent work has shown that the kSZ correlation function will put significant constraints on the dark energy equation of state (Hernández-Monteagudo et al., 2006), and cross-correlation of the kSZ signal with the galaxy density can constrain the redshift evolution of the equation of state (DeDeo et al., 2005). Cluster radial peculiar velocities alone can be used to constrain the matter density of the universe (Peel and Knox, 2003; Bhattacharya and Kosowsky, 2007), the primordial power spectrum normalization (Bhattacharya and Kosowsky, 2007), and the dark energy equation of state (Bhattacharya and Kosowsky, 2007).

In the following chapters we explore the merit of radial peculiar velocity as a dark energy probe and the systematic errors that would contaminate the signal. Each of the following chapters consist of the chapter summary at the conclusion of the chapter. This would allow the readers to get a quick grasp of the contents of the chapters without delving into details. In chapter 2, we begin by discussing various radial peculiar velocity statistics and determine how well they agree with the numerical simulation. Chapter 3 explores various sources of errors and the cosmological parameter constraints obtainable from the future radial peculiar velocity surveys and comparison of radial peculiar velocity statistics with other dark energy probes. Chapter 4 focuses on the systematic errors and how they may bias the cosmological parameter determination from the radial peculiar velocity statistics. In chapter 5, a numerical simulation study explores the impact of quasar feedback on various properties of galaxy group sized halos. Finally, in chapter 6, we summarize our results and discuss future prospects.

1.4 PUBLICATIONS

This thesis is based on the following refereed publications:

1. Bhattacharya, S. & Kosowsky, A. 2007, "Cosmological Constraints from Galaxy Cluster

Peculiar Velocities," ApJL, 659, L83, arXiv:astro-ph/0612555.

2. Bhattacharya, S. & Kosowsky, A. 2008, "Dark Energy Constraints from Galaxy Cluster Peculiar Velocities," Phys. Rev. D 77, 083004, arXiv:astro-ph/0712.0034.

3. Bhattacharya, S. & Kosowsky, A. 2008, "Systematic Errors in Sunyaev-Zeldovich Surveys of Galaxy Cluster Velocities," JCAP, 08, 030, arXiv:astro-ph/0804.2494.

4. Bhattacharya, S., Di Matteo, T. & Kosowsky, A. 2008, "Impact of Quasar Feedback in Galaxy Groups," MNRAS, 389, 34, arXiv:astro-ph/0710.5574.

Chapter 2 is based on publications 1 and 2 (section II and III). My contribution to this work consists of a broad review of the literature and writing the numerical codes to compute the radial peculiar velocity statistics for various cosmological models. I have also computed the radial peculiar velocity statistics using the halo catalog from the VIRGO simulation and then I compare with the theoretical model computed above. I wrote the first draft of both publications. Arthur Kosowsky originally suggested this line of inquiry; he checked my calculations and revised the original draft.

Chapter 3 is based on section IV through VII of publication 2. I have derived the expressions for error models for different radial peculiar velocity statistics, given in the Appendices of this thesis. I have also developed the numerical codes to calculate the merit of radial peculiar velocity surveys to constrain the dark energy parameters, and compared these with other dark energy probes. I acknowledge many useful discussions with Arthur Kosowsky that helped in the derivation of the error models given in the appendices; he also checked these calculations.

Chapter 4 is based on publication 3. I have developed the numerical codes to calculate the systematic errors and to calculate the theoretical uncertainty when nuisance parameters are included. Arthur Kosowsky has helped with editing the original paper draft I wrote and also with checking the results obtained.

Chapter 5 is based on publication 4. For this study, I have implemented various numerical codes for simulation analysis using IDL software; I have also used a numerical code provided by Tiziana Di Matteo. The simulation output used in this work was kindly provided by Tiziana Di Matteo. I acknowledge many helpful discussions with Tiziana Di Matteo throughout the study which helped in developing the numerical codes. Arthur Kosowsky suggested this study and initiated the collaboration with Tiziana Di Matteo; both of my collaborators helped revise the original draft of the paper I wrote.

Chapter 6 summarizes the conclusions from all the publications listed above.

2.0   THEORY

2.1   THE HALO MODEL FOR RADIAL PECULIAR VELOCITY STATISTICS

To study the potential of galaxy cluster radial peculiar velocity surveys to serve as a dark energy probe, we consider three different radial peculiar velocity statistics: the probability distribution function of the line-of-sight component of peculiar velocities n_v; the mean pairwise peculiar velocity $v_{ij}(r)$, which is the relative peculiar velocity along the line of separation of cluster pairs averaged over all pairs at fixed separation r; and the two-point radial peculiar velocity correlation function $\langle v_i v_j \rangle(r)$ as a function of separation r. In the halo model picture of the dark matter distribution (Cooray and Sheth, 2002; Zentner, 2007), these quantities can be written as the sum of the contribution from one-halo and two-halo terms. The one-halo term arises due to the correlation of objects residing in a single halo while the two-halo term arises due to the correlation of objects in two different halos. Typically the one-halo term becomes important at smaller scales (≤ 10 Mpc/h). At large scales the two-halo term becomes dominant. We are interested only in very massive clusters ($M > 10^{14} M_\odot/h$) which are rare objects. Their statistics are shot noise dominated at the smaller scales and hence the statistics only becomes important at much larger scales, so the one-halo term can be neglected.

Here we summarize the halo model ingredients which go into computing the values of these radial peculiar velocity statistics for given cosmological models. Define moments of the initial mass distribution with power spectrum $P(k)$ by Bardeen et al. (1986)

$$\sigma_j^2(m) \equiv \frac{1}{2\pi^2} \int_0^\infty dk (k^{2+2j}) P(k) W^2(kR(m)) \tag{2.1}$$

9

when smoothed on the scale $R(m) = (3m/4\pi\rho_0)^{1/3}$ with the top-hat filter $W(x) = 3[\sin(x) - x\cos(x)]/x^3$, and ρ_0 the present mean matter density. The spherical top-hat halo profile is adopted for simplicity. It could be replaced by a more realistic NFW profile; however, we are interested only in statistics of the most massive clusters at large scales where details of halo profiles make no significant difference. We also write $H(a)$ for the Hubble parameter as a function of scale factor a, and R_{local} for a smoothing scale with which the local background density δ is defined.

The number density of halos of a given mass $n(m)$ is taken as the Jenkins mass function (Jenkins et al., 2001)

$$\frac{dn}{dm}(m, z) = 0.315 \frac{\rho_0}{m^2} \frac{d\ln\sigma_0(m)}{d\ln m} \exp\left[-|0.61 - \ln(\sigma_0(m)D_a)|^{3.8}\right]. \tag{2.2}$$

This mass function is a fit to numerical simulations of cold dark matter gravitational clustering. The bias factor can be written as (Sheth et al., 2001a)

$$b(m, z) = 1 + \frac{\delta_{\text{crit}}^2 - \sigma_0^2(m)}{\sigma_0^2(m)\delta_{\text{crit}}D_a} \tag{2.3}$$

where D_a is the linear growth factor at scale factor a, normalized to 1 today. The growth factor D_a at a redshift $z = 1/a - 1$ (a=scale factor of the universe) is the ratio of the amount of matter density fluctuation at a linear mode k at the redshift z to the current ($z = 0$) amount of fluctuation at the same mode k. The critical overdensity $\delta_{\text{crit}} \approx 1.686$. Since clusters preferentially form at points in space of larger overdensity, the number density of clusters for a given mass and formed in a given local overdensity can be written as (Sheth and Diaferio, 2001)

$$n(m|\delta) \approx [1 + b(m)\delta]\,\bar{n}(m). \tag{2.4}$$

The matter power spectrum $P(k)$ at the present epoch can be well fit through a transfer function as

$$P(k) = \frac{Bk^n}{[1 + [\alpha k + (\beta k)^{3/2} + (\gamma k)^2]^\nu]^{2/\nu}} \tag{2.5}$$

where $\alpha = (6.4/\Gamma)h^{-1}$ Mpc, $\beta = (3.0/\Gamma)h^{-1}$ Mpc, $\gamma = (1.7/\Gamma)h^{-1}$ Mpc, $\nu = 1.13$ and $\Gamma = \Omega_m h$ (Bond and Efstathiou, 1984; Efstathiou et al., 1992).

B is the normalization of the primordial power spectrum and is fixed at large scales by normalizing to the amplitude of the microwave background temperature anisotropy fluctuation. The transfer function transforms the primordial matter power spectrum, which is a power law in k, to the matter power spectrum at the current epoch. The matter fluctuations on scales smaller than the horizon during the radiation dominated phase were roughly constant and did not grow. This is imprinted in the matter power spectrum today. The amplitude of fluctuations smaller than the scale given by the matter radiation equality is suppressed. The transfer function accounts for this suppresion through the shape parameter Γ to a good approximation. Note that we have assumed the cold dark matter paradigm here and hence the initial velocity dispersion is zero. This approximations is not valid in the presence of other dark matter candidates.

2.1.1 Probability Distribution Function

The probability $p(v \mid m, \delta, a)$ that a cluster of mass m located in an overdensity δ moves with a line-of-sight peculiar velocity v can be approximated by a normal distribution (Sheth and Diaferio, 2001),

$$p(v \mid m, \delta, a) = \left(\frac{3}{2\pi}\right)^{1/2} \frac{1}{\sigma_v(m,a)} \exp\left(-\frac{1}{2}\left[\frac{3v}{\sigma_v(m,a)}\right]^2\right) \tag{2.6}$$

with the three-dimensional peculiar velocity dispersion smoothed over a length scale $R(m)$ given by (Hamana et al., 2003)

$$\sigma_v(m,a) = [1 + \delta(R_{\text{local}})]^{2\mu(R_{\text{local}})} \, aH(a)D_a \frac{d\ln D_a}{d\ln a} \left(1 - \frac{\sigma_0^4(m)}{\sigma_1^2(m)\sigma_{-1}^2(m)}\right)^{1/2} \sigma_{-1}(m,a) \tag{2.7}$$

and (Sheth and Diaferio, 2001)

$$\mu(R_{\text{local}}) \equiv 0.6\sigma_0^2(R_{\text{local}})/\sigma_0^2(10\,\text{Mpc/h}). \tag{2.8}$$

Following Hamana et al. (2003), R_{local} is obtained empirically using N-body simulations via the condition $\sigma_0(R_{\text{local}}) = 0.5(1 + z)^{-0.5}$.

Then the probability density function of the line-of-sight peculiar velocity component at some redshift z is given by (Sheth and Diaferio, 2001)

$$f(v,a) = \frac{\int dm\, mn(m|\delta)p(v|m,\delta,a)}{\int dm\, mn(m|\delta,a)} \tag{2.9}$$

where $n(m|\delta)dm$ is the number density of halos that have mass between m and $m+dm$ in a region with overdensity δ. The dependence of these quantities on redshift is left implicit.

Finally, in order to connect to a readily observable quantity, we write the fraction of clusters that have radial peculiar velocity between v and $v + \delta v$ as

$$n_v(v,\delta v,a) = \int_{\delta v} dv f(v,a). \tag{2.10}$$

2.1.2 Mean Pairwise Peculiar Velocity

The mean pairwise peculiar velocity $v_{ij}(r)$ between all pairs of halos at comoving separation r and scale factor a can be related to the linear two-point correlation function for dark matter, $\xi DM(r,a)$, using large-scale bias of the halos compared to the underlying dark matter distribution, $b_{\text{halo}}(a)$, and the pair conservation equation (Sheth et al., 2001a; Davis and Peebles, 1977):

$$v_{ij}(r,a) = -\frac{2}{3}H(a)a\frac{d\ln D_a}{d\ln a}b_{\text{halo}}(a)\frac{r\bar{\xi}^{\text{DM}}(r,a)}{1+b_{\text{halo}}(a)^2\xi^{\text{DM}}(r,a)}. \tag{2.11}$$

The two-point density correlation ξ of the dark matter fluctuations δ at a separation r is given by $\xi(r) = \langle\delta(x)\delta(x+r)\rangle$ where the $\langle..\rangle$ denotes the average over all pairs that are at a fixed separation.

The linear two-point correlation function of the dark matter fluctuations can be computed via

$$\xi^{\text{DM}}(r,a) = \frac{D_a^2}{2\pi^2 r}\int_0^\infty dk k\sin kr P(k), \tag{2.12}$$

while the two-point correlation function of the dark matter fluctuations averaged over a sphere of radius r can be written as

$$\bar{\xi}^{\text{DM}}(r,a) = \frac{D_a^2}{2\pi^2 r^2}\int_0^r dr r\int_0^\infty dk k\sin kr P(k) \tag{2.13}$$

where average halo bias factors are given by

$$b_{\text{halo}}(a) \equiv \frac{\int dm\, mn(m)b(m,a)W^2[kR(m)]}{\int dm\, mn(m)W^2[kR(m)]}.$$ (2.14)

Direct evaluation of the above expression for mean pairwise peculiar velocity requires knowledge of all three velocity components for both halos. In practice, it is only possible to determine the radial peculiar velocity component, so we need an estimator v_{ij}^{est} which depends only on the radial peculiar velocities. Consider two clusters at positions $\mathbf{r}_i$ and $\mathbf{r}_j$ moving with peculiar velocities $\mathbf{v}_i$ and $\mathbf{v}_j$. The radial component of peculiar velocities can be written as $v_i^r = \hat{\mathbf{r}}_i \cdot \mathbf{v}_i$ and $v_j^r = \hat{\mathbf{r}}_j \cdot \mathbf{v}_j$. Following Ferreira et al. (1999), $\langle v_i^r - v_j^r \rangle = v_{ij}^{\text{est}} \hat{\mathbf{r}} \cdot [\hat{\mathbf{r}}_i + \hat{\mathbf{r}}_j]/2$ where $\mathbf{r}$ is the unit vector along the line joining the two clusters and $\hat{\mathbf{r}}$ is the unit vector in the direction $\mathbf{r}$. Then minimizing χ^2 gives

$$v_{ij}^{\text{est}} = 2\frac{\Sigma(v_i^r - v_j^r)p_{ij}}{\Sigma p_{ij}^2}$$ (2.15)

where $p_{ij} \equiv \mathbf{r} \cdot (\mathbf{r}_i + \mathbf{r}_j)$ and the sum is over all pairs of clusters with separation r.

2.1.3 Radial Peculiar Velocity Correlation Function

In addition to the mean relative peculiar velocity between two halos, we can also consider correlations of these radial peculiar velocities. Assuming statistical isotropy, the only non-trivial correlations will be of the peculiar velocity components along the line connecting the clusters and of the peculiar velocity components perpendicular to the line connecting the clusters; furthermore, these correlations will only depend on the separation $r = |\mathbf{r}_i - \mathbf{r}_j|$. Geometrically, the correlation of radial peculiar velocities must be of the form (Peel, 2006)

$$\Psi_{ij} = \Psi_\perp \cos\theta + (\Psi_\parallel - \Psi_\perp)\frac{(r_i^2 + r_j^2)\cos\theta - r_i r_j(1 + \cos^2\theta)}{r_i^2 + r_j^2 - 2r_i r_j \cos\theta}$$ (2.16)

where $\theta = \hat{\mathbf{r}}_i \cdot \hat{\mathbf{r}}_j$ is the angle between the two cluster positions; $\Psi_\perp(r)$ and $\Psi_\parallel(r)$ denotes the correlations perpendicular to the line of separation $\mathbf{r}$ and parallel to it, respectively. Including the fact that high-density regions have lower rms radial peculiar velocities than

random patches and allowing the two halos to have different masses, the expressions for correlations can be written as (Sheth et al., 2001b; Gorski, 1988)

$$
\begin{aligned}
\Psi_{\perp,\parallel}(m_i, m_j | r) &= \frac{\sigma_0(m_i)\sigma_0(m_j)}{\sigma_{-1}(m_i)\sigma_{-1}(m_j)} a^2 \frac{H(a)^2}{2\pi^2} \left[\frac{d\ln D_a}{d\ln a}\right]^2 D_a^2 \\
&\times \int dk P(k) W[kR(m_i)] W[kR(m_j)] K_{\perp,\parallel}(kr)
\end{aligned}
\tag{2.17}
$$

where

$$
K_{\perp} = \frac{j_1(kr)}{kr}, \qquad K_{\parallel} = j_0(kr) - 2\frac{j_1(kr)}{kr}
\tag{2.18}
$$

and $j_0(kr)$ and $j_1(kr)$ are the spherical Bessel functions.

With all the above ingredients, the correlation function for the radial peculiar velocity component perpendicular to the line connecting the clusters can be written as (Sheth et al., 2001b)

$$
\langle v_i v_j \rangle_{\perp}(r, a) = \left[H(a)a\frac{d\ln D_a}{d\ln a}D_a\right]^2 \int dm_i \frac{m_i n(m_i)}{\bar{\rho}} \int dm_j \frac{m_j n(m_j)}{\bar{\rho}} \frac{1 + b(m_i)b(m_j)\xi^{DM}(r)}{[1 + \xi^{DM}(r)]} \Psi_{\perp}
\tag{2.19}
$$

where $\Psi_{\perp} = \Psi_{\perp}(m_i, m_j | r)$ and $\bar{\rho} = \int dm\, m\, n(m)$. Note that the above expression is a slight modification from Eq. (23) of Sheth et al. (2001b). The expression for the correlation of the parallel radial peculiar velocity component is obtained simply by replacing $\Psi_{\perp}$ with $\Psi_{\parallel}$. Performing the average over all pairs that are at a separation r yields

$$
\langle v_i v_j \rangle_{\perp}(r, a) = a^2 H(a)^2 \left(\frac{d\ln D_a}{d\ln a}\right)^2 D_a^2 \frac{1}{1 + \xi^{DM}(r, a)} \frac{1}{\bar{\rho}^2} \left[I_1 + \xi^{DM}(r, a)I_2\right]
\tag{2.20}
$$

where

$$
I_1 = \int dk K_{\perp}(kr) P(k) \left[\int dm\, m\, n(m) \frac{\sigma_0(m)}{\sigma_{-1}(m)} W[kR(m)]\right]^2,
\tag{2.21}
$$

and

$$
I_2 = \int dk K_{\perp}(kr) P(k) \left[\int dm\, m\, n(m) b(m, a) \frac{\sigma_0(m)}{\sigma_{-1}(m)} W[kR(m)]\right]^2.
\tag{2.22}
$$

Although the above expression holds for both the parallel and perpendicular components, in simulations $\Psi_{\parallel}$ is mostly negative or zero due to the heavy influence of infall at large separations (Peel, 2006). However, this anticorrelation is not seen in linear perturbation theory or in the halo model, which both predict positive correlation for pair comoving separations less than 40 Mpc; for separations larger than 40 Mpc, the theory and simulations are consistent,

but the parallel component correlation is essentially zero. Given this discrepancy between known analytical models and simulations for the parallel correlation function in the region where the signal is non-negligible, we only consider $\langle v_i v_j \rangle_\perp (r, z)$ in the rest of this chapter.

2.2 COMPARISON WITH SIMULATIONS

The statistics computed in the previous section are based on the halo model of structure formation combined with linear perturbation theory. Since galaxy clusters are rare objects and their distribution can be described well in the quasi-linear regime of structure formation, we expect that these approximations for radial peculiar velocity statistics should be reasonably accurate. Here we verify that they are good approximations to the actual galaxy cluster radial peculiar velocity statistics extracted from the the VIRGO dark matter simulation (Evrard et al., 2002). We use the octant sky survey lightcone output of Lambda Cold Dark Matter (LCDM) cosmology, with $\sigma_8 = 0.9$, $n_s = 1$, $\Omega_m = 0.3$, $\Omega_\Lambda = 0.7$ and $h = 0.7$. The maximum redshift of the light cone is $z_{\mathrm{max}} = 1.46$ and the radius of extent is $R_{\mathrm{max}} = 3000$ Mpc/h. The data is binned in redshift slices of width $\delta z = 0.2$ from $z = 0$ to $z = 1.4$

The statistics defined in the previous section apply to infinitesimal intervals in redshift. When comparing with data binned in redshift, it is necessary to normalize the radial peculiar velocity statistics properly to reflect this binning. We do this by averaging the above theoretical expressions for the statistics over a given bin in z to obtain a binned estimator of the underlying statistic. Additionally, for the case of the radial peculiar velocity probability distribution function, a realistic measurement will provide numbers of clusters in a set of line-of-sight peculiar velocity bins. In this case, the relevant statistic for comparison becomes the theoretical probability that the radial peculiar velocity of a given cluster is in a particular radial peculiar velocity bin; the above expression for probability density in infinitesimal radial peculiar velocity bins must be integrated over the width of the radial peculiar velocity bin. This gives the correct relative probability between any two radial peculiar velocity bins, but all should then be renormalized by a constant factor to enforce the condition that the sum of the probabilities for all bins be unity. All comparisons with simulations below use

these binned versions of the underlying statistics defined in the previous section.

Figure 2.1 shows n_v in the redshift slice between $z = 0$ and $z = 0.2$ both from the simulation and using Eq. (2.10) for the radial peculiar velocity probability distribution function. The analytical model agrees fairly well with the simulation; the error bars denote the 1σ errors including Poisson error and errors due to cosmic variance. Error modeling is discussed in detail in the next section. Note that the error bars shown in Figure 2.1 are for a large future 5000 square degree radial peculiar velocity survey (one octant of the sky). Figures 2.2 and 2.3 compare the simulation with Eq. (2.11) for the mean pairwise peculiar velocity (using the estimator Eq. (2.15)) and Eq. (2.20) for the radial peculiar velocity correlation function, respectively. The plots shows that the halo model agrees well with the simulated data at separations greater than 30 Mpc/h for radial peculiar velocity correlation, and greater than 40 Mpc/h for mean pairwise peculiar velocity with a discrepancy somewhat larger than 1σ for r between 30 and 40 Mpc/h. For the radial peculiar velocity probability distribution function, we find a good fit when the radial peculiar velocity data is smoothed over a scale of 10 Mpc. The smoothing on this scale reduces the effect of nonlinear physics, which is difficult to model semi-analytically.

Figure 2.4 displays a comparison between the estimated mean pairwise peculiar velocity v_{ij}^{est} obtained only from the radial component of peculiar velocity using Eq. (2.15) and the full v_{ij} obtained from all three components of peculiar velocity in the simulation. For an ideal estimator, these quantities would be exactly the same; the actual estimator in general does quite well, except for a 1σ discrepancy at separations below 30 Mpc/h. The error range is the same as for Figure 2.2.

2.3   CHAPTER SUMMARY

Future multifrequency microwave background experiments with arcminute resolution and micro-Kelvin temperature sensitivity will be able to detect the kSZ effect, providing a way to measure radial peculiar velocities of massive galaxy clusters. In order to asses the power of future radial peculiar velocity statistics as a dark energy probe, we need to develop the
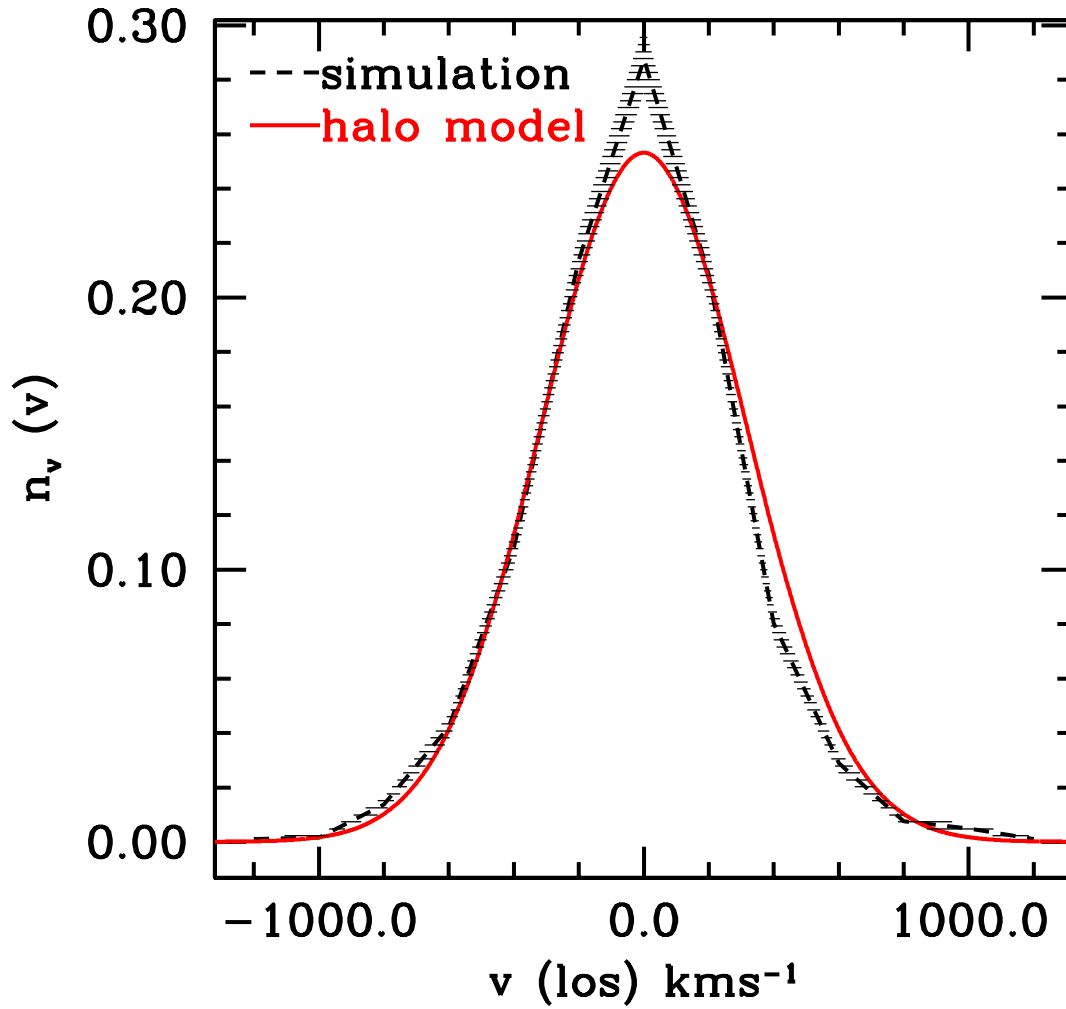
Figure 2.1 A comparison between the probability distribution function n_v evaluated directly using the Virgo lightcone numerical simulation (dotted curve with error bars) and approximated using the analytic halo model formula, Eq. (2.10) (solid red curve). Error bars are Poisson plus cosmic variance errors for one octant sky coverage.
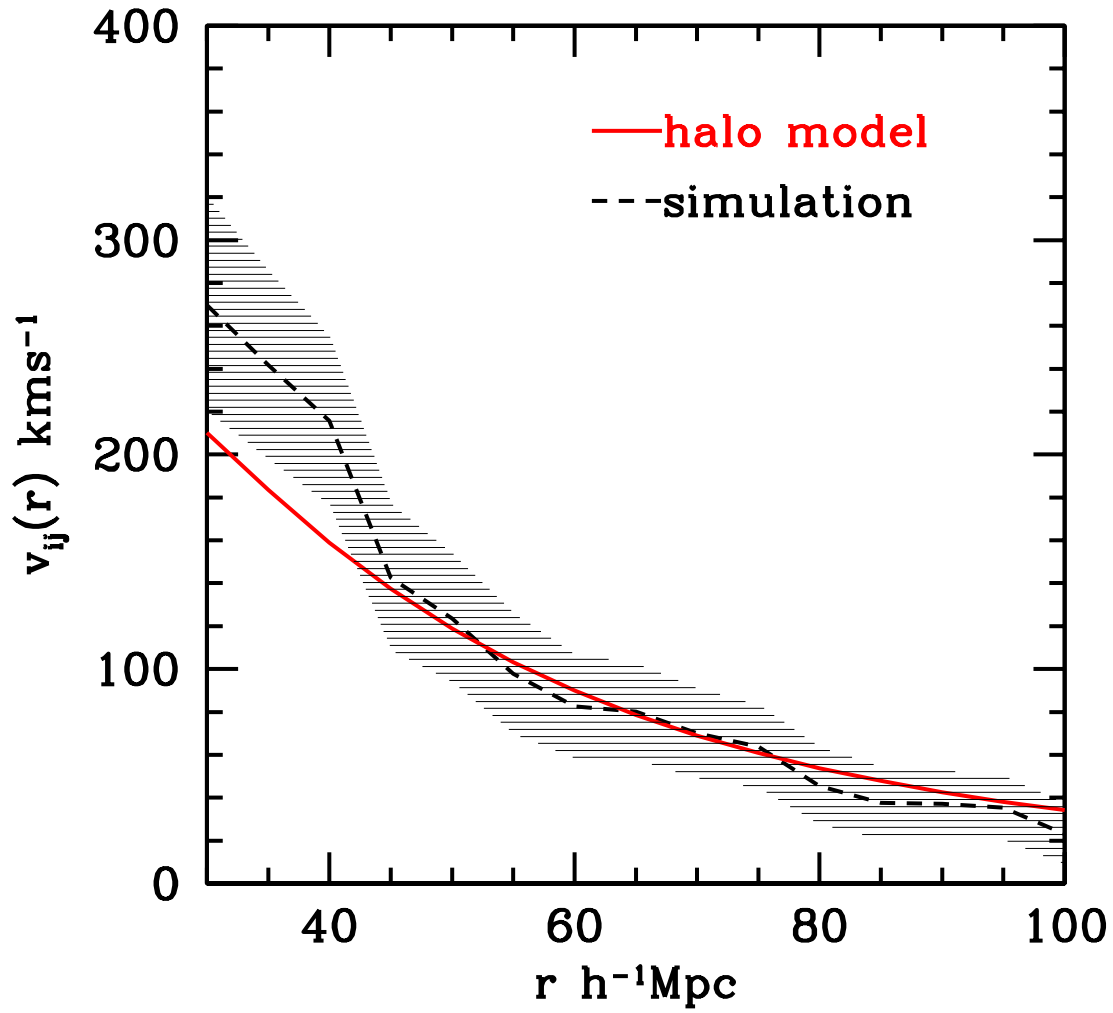
Figure 2.2 A comparison between the mean pairwise peculiar velocity $v_{ij}(r)$ evaluated directly using the Virgo lightcone numerical simulation (dashed line with 1σ errors given by the blue dotted lines) and approximated using the analytic halo model formula, Eq. (2.11) (red solid curve). The error range includes Poisson and cosmic variance errors for one octant sky coverage, plus random measurement errors of 100 km/s.
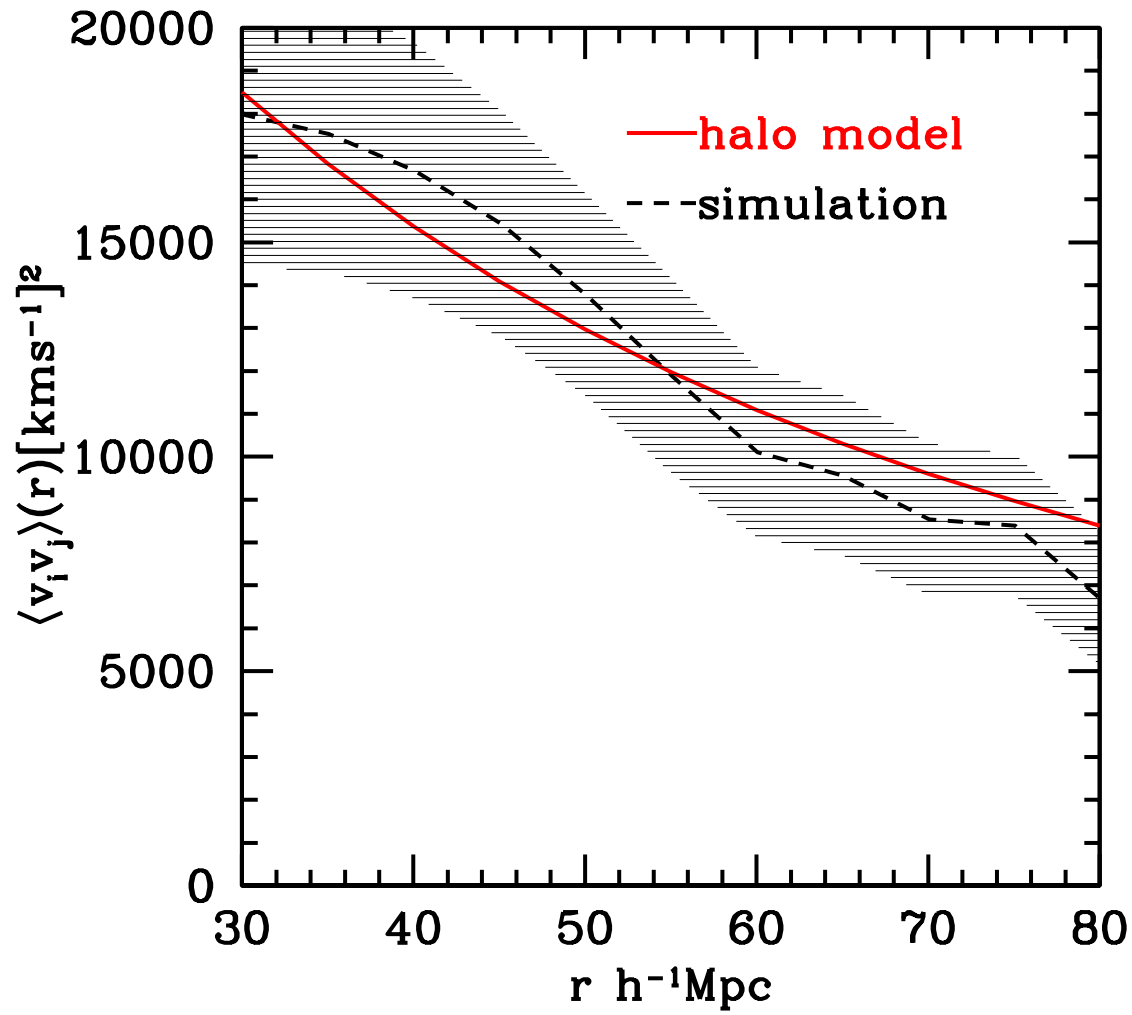
Figure 2.3 Same as Figure 2.2 except for the radial peculiar velocity correlation $\langle v_i v_j \rangle_\perp(r)$ and the analytic formula Eq. (2.20).
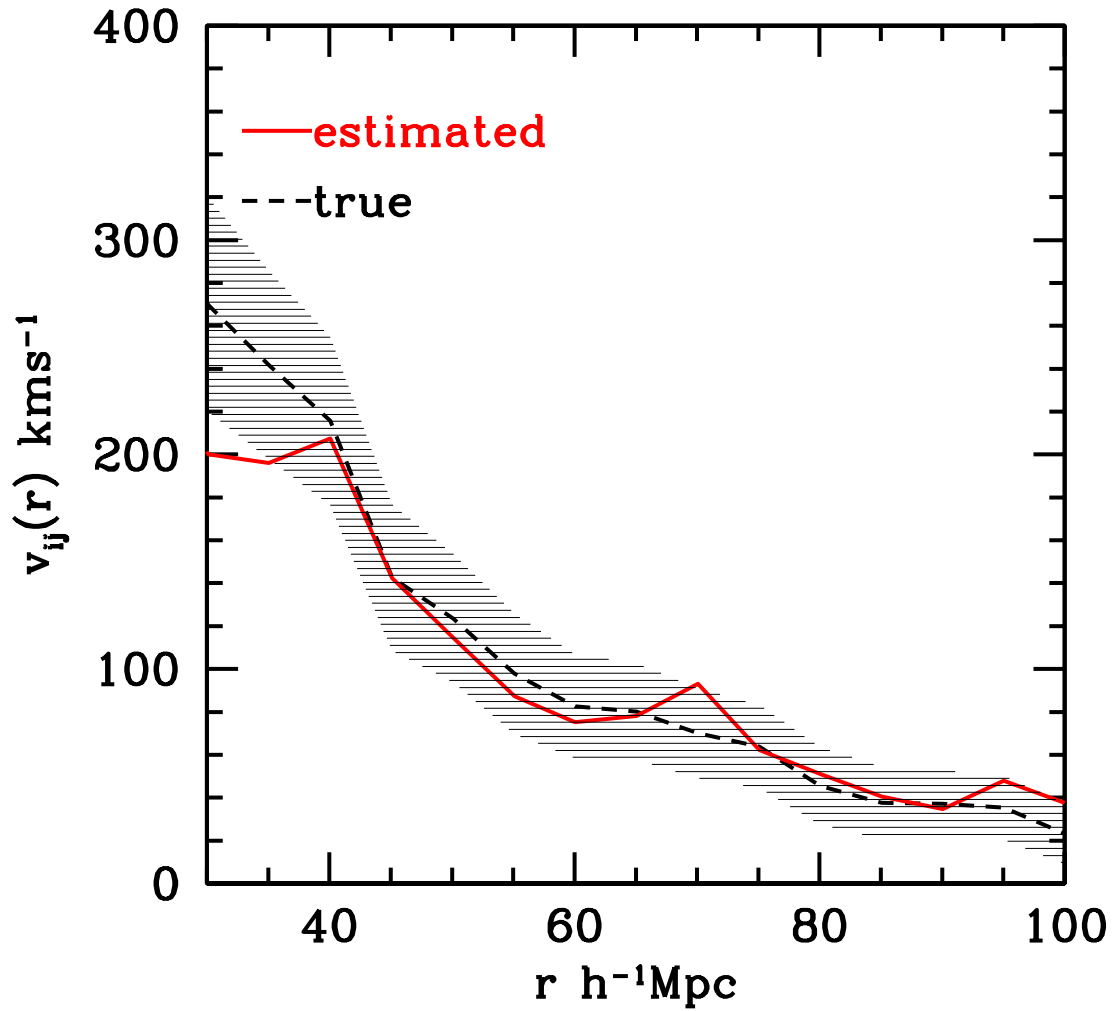
Figure 2.4 The solid red line shows v_{ij}^{est} computed from the Virgo simulation using only the radial peculiar velocities, Eq. (2.15), while the dashed line shows v_{ij} and shaded 1σ errors computed using all three peculiar velocity components, the same as in Fig. 2.2
.

theoretical model for various radial peculiar velocity statistics. To this end, we have summarized the theoretical expressions obtained using the halo model. We have also discussed the estimator used in the context of the mean pairwise peculiar velocity statistics that is used to compute the statistics from the line-of-sight components of peculiar velocities. Using the halo catalog from the Virgo simulation, we have numerically computed the radial peculiar velocity statistics. The result shows that the theoretical model agrees fairly accurately with the simulation results at scales larger than 30 Mpc/h.

3.0 DARK ENERGY CONSTRAINTS FROM GALAXY CLUSTER RADIAL PECULIAR VELOCITIES

The aim of this chapter is to address error analysis in detail, and compare the relative merits of various radial peculiar velocity statistics in constraining dark energy parameters. We use a Fisher matrix calculation to compare the power of various radial peculiar velocity statistics as dark energy probes over a range of radial peculiar velocity errors.

We also compare the merit of radial peculiar velocity as a dark energy probe with other dark energy probes proposed by the Dark Energy Task Force (DETF) report (Albrecht et al., 2006). The DETF report considers four potential probes of dark energy: baryon acoustic oscillations, weak gravitational lensing of galaxies, the distance-redshift relation using Type Ia supernovae as standard candles, and galaxy cluster counts as a function of redshift. The DETF report forecasts constraints on two dark energy parameters (describing the dark energy equation of state and its redshift evolution) for each of the proposed probes, obtainable from current and future observations. The assumed characteristics of various surveys considered in the task force report are given in Table 3.5.

We find that for a sufficiently large radial peculiar velocity catalog, the dark energy parameter constraints degrade only by a factor of two when the radial peculiar velocity errors increase by a factor of five. Comparing with other dark energy probes, cluster radial peculiar velocities from a large survey can provide dark energy constraints that are comparable to weak lensing and supernovae and a factor of two to three better than cluster counts and baryon acoustic oscillations. Combining cluster radial peculiar velocities with other dark energy probes improves the total constraint on the dark energy density by 10-15% and the Dark Energy Task Force Figure of Merit by a factor of 1.4 to 2.5. Cluster radial peculiar velocities can be competitive with other proposed techniques for probing dark energy, with

completely different systematic errors.

Throughout this chapter, we assume a cluster radial peculiar velocity catalog with some normal radial peculiar velocity error; we consider errors from 200 km/sec to 1000 km/sec, representing a range from optimistic to conservative based on current experimental sensitivities and anticipated astrophysical complications. Using this range of errors, we then evaluate the statistical constraints on dark energy parameters, assuming a cluster catalog with a given number of cluster radial peculiar velocities. In practice, constraints from cluster radial peculiar velocities may well be dominated by systematic, rather than statistical, errors, like all other methods of probing dark energy. When analyzing real data to constrain dark energy, understanding these systematic errors is obviously crucial in getting the right answers. Note that systematic errors will tend to bias parameter constraints but will not generally change the size of the statistical errors significantly. A discussion of various relevant systematics is given in the last section of the chapter; we will address this issue in more detail in the next chapter. However, in order to compare with the dark energy probes proposed by the DETF report, we simply increase the range of statistical errors that future radial peculiar velocity surveys are expected to have.

This chapter is organized as follows. Section 3.1 discusses various sources of errors for each of the statistics and presents analytic expressions for the errors; detailed derivations of these expressions are given in three Appendices. Using these expressions for the values of the radial peculiar velocity statistics and their errors in hypothetical surveys of given sky area and radial peculiar velocity errors, section 3.2 uses standard Fisher matrix techniques to compute constraints on dark energy parameters from the various radial peculiar velocity statistics. Section 3.3 studies the complementarity of cluster radial peculiar velocities with cluster counts. Section 3.4 then compares the cosmological constraints obtainable from cluster radial peculiar velocities with those from the probes analyzed by the Dark Energy Task Force.

3.1 ERROR SOURCES

Measurement of the radial peculiar velocities of individual clusters via their kSZ signal is affected by various error sources, including detector noise in the microwave maps, separating the small signal from other larger signals at the same frequencies (particularly the tSZ signal, infrared point sources, and gravitational lensing by the cluster), the internal velocity dispersion of the intracluster medium, and X-ray temperature measurement errors. In this section, we call the total error from all of these sources "measurement error." We also consider separately the errors arising from cosmic variance and Poisson noise; both of these error sources are independent of the measurement errors for any individual cluster.

3.1.1 Radial Peculiar Velocity Measurement Errors

Upcoming multi-frequency SZ measurements with arcminute resolution and few μK sensitivity have the potential to obtain galaxy cluster radial peculiar velocities. However, the kSZ signal is small compared to the tSZ signal, and is spectrally indistinguishable from the primary microwave blackbody fluctuations or their gravitational lensing. In addition, radio and infrared galaxies contribute substantial signal in the microwave bands, and are expected to be spatially correlated with galaxy cluster positions (Coble et al., 2007). Comparatively modest error sources can substantially hinder cluster radial peculiar velocity measurements if they are not well understood and accounted for.

Major potential sources of error in measuring the radial peculiar velocities of individual galaxy clusters include internal cluster gas velocities, the confusion-limited noise from point sources, uncertainties in extrapolating measured point sources to the frequencies of a particular experiment, instrumental noise, and the particular frequency bands available. Previous studies shows that primary microwave background fluctuations plus point sources set a confusion limited radial peculiar velocity error of around 200 km/s for an experiment with arcminute resolution and few μK sensitivity (Knox et al., 2004; Aghanim et al., 2001; Haehnelt and Tegmark, 1996), provided no other point source follow-up observations are utilized. The bulk flow of the gas in the intracluster medium contributes to an irreducible

error of 100 to 150 km/s (Nagai et al., 2003; Diaferio et al., 2005a). Also, Sehgal et al. (2005) shows that to extract radial peculiar velocity from SZ observations at the three ACT frequency channels (145, 220, and 280 GHz), a followup measurement of X-ray temperature of the cluster is needed to break a spectrum degeneracy between cluster gas radial peculiar velocity, optical depth, and temperature. While Diaferio et al. (2005a) studied over 100 simulated clusters, the rest of these studies use only a few. All of these error sources require detailed simulations of particular experiments observing realistic simulated clusters and optimal algorithms for extracting cluster radial peculiar velocities from measurements in particular frequency bands and at given instrumental noise levels. The ultimate distribution of radial peculiar velocity errors is still uncertain and future study in this direction is needed. In order to study the effect of measurement errors on parameter estimation, we make the simple assumption that radial peculiar velocity errors have a normal distribution with a magnitude between 100 and 500 km/s. Directly adding all of the known sources of error from previous studies gives radial peculiar velocity measurement errors typically in the range of 400 to 500 km/s; however, with further understanding of systematic errors and point sources, the error budget may be reduced.

3.1.2 Systematic Errors in the Radial Peculiar Velocity Surveys

As will be discussed in detail in the next chapter, galaxy cluster radial peculiar velocity will be prone to various sources of systematic errors, namely the mass-selection bias, the mismatch of the temperature of the clusters derived from the SZ experiment with the X-ray temperature, and the contamination due to radio and infrared point sources. The nature of how some of these errors will affect future radial peculiar velocity surveys is not precisely known, and further studies are required in this direction. Previous simulation studies (Knox et al., 2004) indicated the statistical error for the radial peculiar velocity will be in the range of 200-400 km/s. In order to compare with the DETF probes, we incorporate systematic errors by simply extending the upper limit of statistical measurement error by roughly a factor of 2 in the pessimistic limit at all the DETF stages. In the optimistic limit we assume any systematic errors can be well understood to a level smaller than the impact of statistical

errors using follow-up observations and numerical simulations. Thus for assesing the merit of radial peculiar velocity as a dark energy probe, we consider a range of statistical measurement errors from 200 km/s to 1000 km/s, assuming that the range includes the effect of systematic errors (i.e. missestimate of dark energy parameters) as well.

3.1.3 Redshift Errors

In addition to cluster radial peculiar velocity, we must measure cluster redshift to construct the estimators of the mean pairwise peculiar velocity and the radial peculiar velocity correlation, which involve knowledge of the separation vector between the two clusters. For clusters at cosmological distances, the Hubble contribution to its redshift will typically be much larger than its radial peculiar velocity contribution, which we can also correct for with a direct radial peculiar velocity measurement, so the direct error in the cluster redshift will be the largest contributor to the cluster position error. Typically, we will be concerned with cluster separations larger than 30 Mpc/h, for which the cluster radial peculiar velocity field is in the mildly nonlinear regime and can be well described by the halo model approximation.

A redshift error of 500 km/sec corresponds to a direct Hubble distance error of around 5 Mpc/h, typically only 25% of the closest cluster separation of interest; even for redshift errors of 1000 km/sec, most pair separations will not be dominated by this error. For the remainder of this chapter, we assume that the cluster sample for which radial peculiar velocities are determined also have spectroscopic redshifts from which their distances are determined, and we assume that the distance error effect on the cosmological parameters will be negligible compared to the direct radial peculiar velocity errors. For spectroscopic measurements of many galaxy clusters, the distance to lowest order is simply determined by the average of the galaxy redshifts, with an error given roughly by the cluster galaxy velocity dispersion divided by the square root of the number of clusters' galaxies. Cluster line-of-sight velocity dispersions will typically be 500 km/sec, so multi-object spectroscopy can clearly provide adequate redshift measurements. The systematic error is induced because not all clusters are virialized. This error is potentially important, although beyond the scope of this chapter.

Spectroscopic redshifts for a galaxy cluster at $z = 1$ requires roughly an hour of obser-

vation on an 8-m class telescope. Spectroscopic follow-up of hundreds of clusters per year is a large program for a single telescope; spectroscopic redshifts for thousands of clusters will comprise a multi-year program on more than one telescope. This is likely to be a significant portion of the effort and expense in building a cluster radial peculiar velocity survey with thousands of clusters. Note that cluster galaxy spectroscopic redshifts are also valuable for dynamical mass estimates (see, e.g., Diaferio et al. (2005b); Rines et al. (2003)). The ACT collaboration has plans for spectroscopic follow-up observations of SZ-detected clusters using the Southern African Large Telescope (SALT), a new 10-meter class instrument. If only photometric redshifts are available, typically giving a distance accuracy of one to two percent times $1 + z$, cosmological constraints must be re-evaluated. In general, constraints will be less stringent, although it is not immediately clear whether the resulting distance errors will have an effect which is significant compared to the radial peculiar velocity errors. In our case, redshift errors propagate only into the geometric portions of the mean pairwise peculiar velocity and radial peculiar velocity correlation estimators, but the radial peculiar velocity errors are unaffected.

3.1.4 Cosmic Variance and Poisson Noise

In addition to measurement errors for individual cluster radial peculiar velocities, cosmological quantities are also subject to errors from cosmic variance (any particular region observed may have different statistical properties from the average of the entire universe) and Poisson errors due to the finite size of the cluster radial peculiar velocity sample used to estimate the radial peculiar velocity statistics. Here we discuss these errors for each of the three radial peculiar velocity statistics. Detailed derivations of the expressions in the rest of this section are given in the Appendices.

3.1.4.1 Probability Distribution Function Consider a cluster radial peculiar velocity survey with a measured redshift for each cluster. For the probability distribution function, we write cosmic covariance between two different radial peculiar velocity–redshift bins $[v, z]_i$

and $[v, z]_j$ as $C_{ij}^{n_v}$, which can be expressed as

$$C^{n_v}(ij) = \frac{3 D_{a_i} D_{a_j}}{R_\Omega} n_i n_j \int dk k^2 P(k) j_1(k R_\Omega) \tag{3.1}$$

where

$$n_v(v, z) = \frac{\int dm m b(m, a) \bar{n}(m) p(v|m, \delta, a)}{\int dm m \bar{n}(m)} \tag{3.2}$$

and R_Ω is the comoving length of the redshift bin within the sky survey region (Hogg, 1999).

For Poisson errors, let N_i be the total number of clusters in bin i. We are interested in the error in $n_i = N_i/N_z$ with N_z the total number of clusters in a particular redshift bin summed over all radial peculiar velocities; the measured n_i corresponds to the theoretical quantity $n_v(v, z)$, Eq. (2.10), integrated over the radial peculiar velocity–redshift bin $[v, z]_i$. The expression for Poisson errors can be written as

$$\delta n_i = (\sqrt{n_i} + n_i)/\sqrt{N_z} \tag{3.3}$$

where the first term is from the error in N_i and the second from the error in N_z.

Random radial peculiar velocity measurement errors will smear out the radial peculiar velocity probability distribution function. We quantify the effect of measurement errors by convolving the probability distribution function with a normal distribution of radial peculiar velocity errors,

$$n_v^{\text{obs}}(v, \delta v, z) = \int_{\delta v} dv \int_{v_l}^{v} dv' f(v', z) \exp[-(v' - v)^2/2\sigma_v^2] \tag{3.4}$$

where σ_v is the dispersion of the normally distributed radial peculiar velocity errors and the integral is over the radial peculiar velocity bin. Then the expression for the total covariance can be written as

$$C_t^{n_v}(v_i, z_i; v_j, z_j) = C^{n_v}(ij) + (\delta n_i)^2 \delta_{ij} \tag{3.5}$$

The various curves in Fig. 3.1 show the effect of random radial peculiar velocity errors of different sizes, Eq. (3.4), while the top dotted curve with shaded error region gives the actual value for the probability distribution function from the VIRGO simulation with Poisson plus cosmic variance errors. Smearing the distribution by random radial peculiar velocity errors is largely degenerate with the effect of varying cosmological parameters. This means that the radial peculiar velocity probability distribution function as a probe of cosmology is limited by how well the measurement error can be understood from simulated measurements.
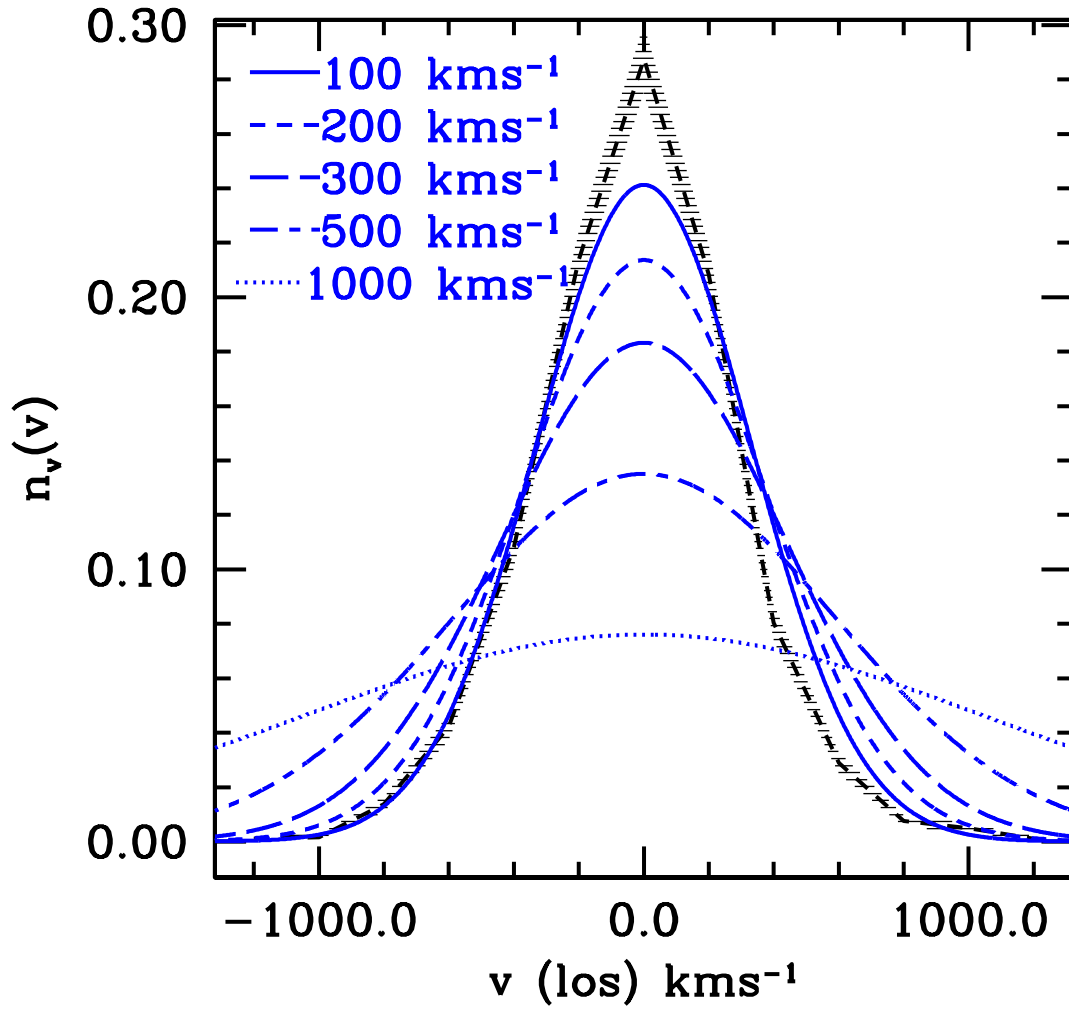
Figure 3.1 The effect of measurement errors on the radial peculiar velocity probability distribution function: from top to bottom, radial peculiar velocity measurement errors of $\sigma_v =$100, 200, 300, 500, and 1000 km/s. Also shown are the probability distribution function evaluated directly using the Virgo lightcone numerical simulation (dotted curve with error bars) from Figure 2.1

3.1.4.2   Mean Pairwise Peculiar Velocity   The mean pairwise peculiar velocity statistic is binned in pair separation and redshift. The cosmic covariance between two bins $[r, z]_p$ and $[r, z]_q$ can be written as

$$
\begin{aligned}
C^{v_{ij}}(pq) &= \frac{32\pi}{9V_\Omega} \frac{H(a_p)a_p b_{\mathrm{halo}}(a_p)}{1 + b_{\mathrm{halo}}(a_p)^2 \xi^{\mathrm{DM}}(r_p, a_p)} \frac{H(a_q)a_q b_{\mathrm{halo}}(a_q)}{1 + b_{\mathrm{halo}}(a_q)^2 \xi^{\mathrm{DM}}(r_q, a_q)} \left(\frac{d\ln D_a}{d\ln a}\right)_{a_p} \left(\frac{d\ln D_a}{d\ln a}\right)_{a_q} \\
&\times \int dk k^2 |P(k)|^2 j_1(kr_p)j_1(kr_q)
\end{aligned}
\tag{3.6}
$$

We add in quadrature the Poisson error and measurement error for n_{pair} cluster pairs and write the total covariance as

$$
C^{v_{ij}}(r_p, z_p; r_q, z_q) = C^{v_{ij}}_{\mathrm{cosmic}}(pq) + \left(\frac{v_{ij}^2}{n_{\mathrm{pair}}} + \frac{2\sigma_v^2}{n_{\mathrm{pair}}}\right)\delta_{pq}
\tag{3.7}
$$

Figure 3.2 plots fractional errors for v_{ij} as a function of pair separation for a survey area of 5000 deg^2. For a survey area f_{sky}, fractional errors scales as roughly $\sqrt{f_{\mathrm{sky}}}$. Note that the Poisson error decreases for larger separation since more clusters pairs are available to average over, whereas cosmic variance has an increasing effect at larger separation. The combined effect of cosmic variance plus Poisson errors dominates the error budget when radial peculiar velocity measurement errors are below 200 km/s. Note that even when the measurement errors are as high as $\sigma_v = 500$ km/s, the total error is typically 50% of the magnitude of mean pairwise peculiar velocity. We will show in sec. 3.2 that this fact makes mean pairwise peculiar velocity a potentially useful probe to study cosmology.

3.1.4.3   Radial Peculiar Velocity Correlation Function   Similarly for the radial peculiar velocity correlation function, the expression for cosmic covariance can be written as

$$
\begin{aligned}
C^{\langle v_i v_j \rangle}_{\mathrm{cosmic}}(pq) &= \frac{8\pi}{V_\Omega \bar{\rho}^2(p)\bar{\rho}^2(q)} \left[\frac{d\ln D_a}{d\ln a}\right]^2_{a_p} \left[\frac{d\ln D_a}{d\ln a}\right]^2_{a_q} \frac{a_p^2 D_{a_p}^2 H^2(a_p)}{1 + \xi^{\mathrm{DM}}(r_p, a_p)} \frac{a_q^2 D_{a_q}^2 H^2(a_q)}{1 + \xi^{\mathrm{DM}}(r_q, a_q)} \\
&\times \int dk j_1(kr_p)j_1(kr_q)[P(k)]^2 \langle p \rangle_m^2 \langle q \rangle_m^2
\end{aligned}
\tag{3.8}
$$

using the notational abbreviation

$$
\langle x \rangle_m \equiv \int dm\, m \frac{dn}{dm} W(kR(m)) \frac{\sigma_0(m)}{\sigma_{-1}(m)} x.
\tag{3.9}
$$
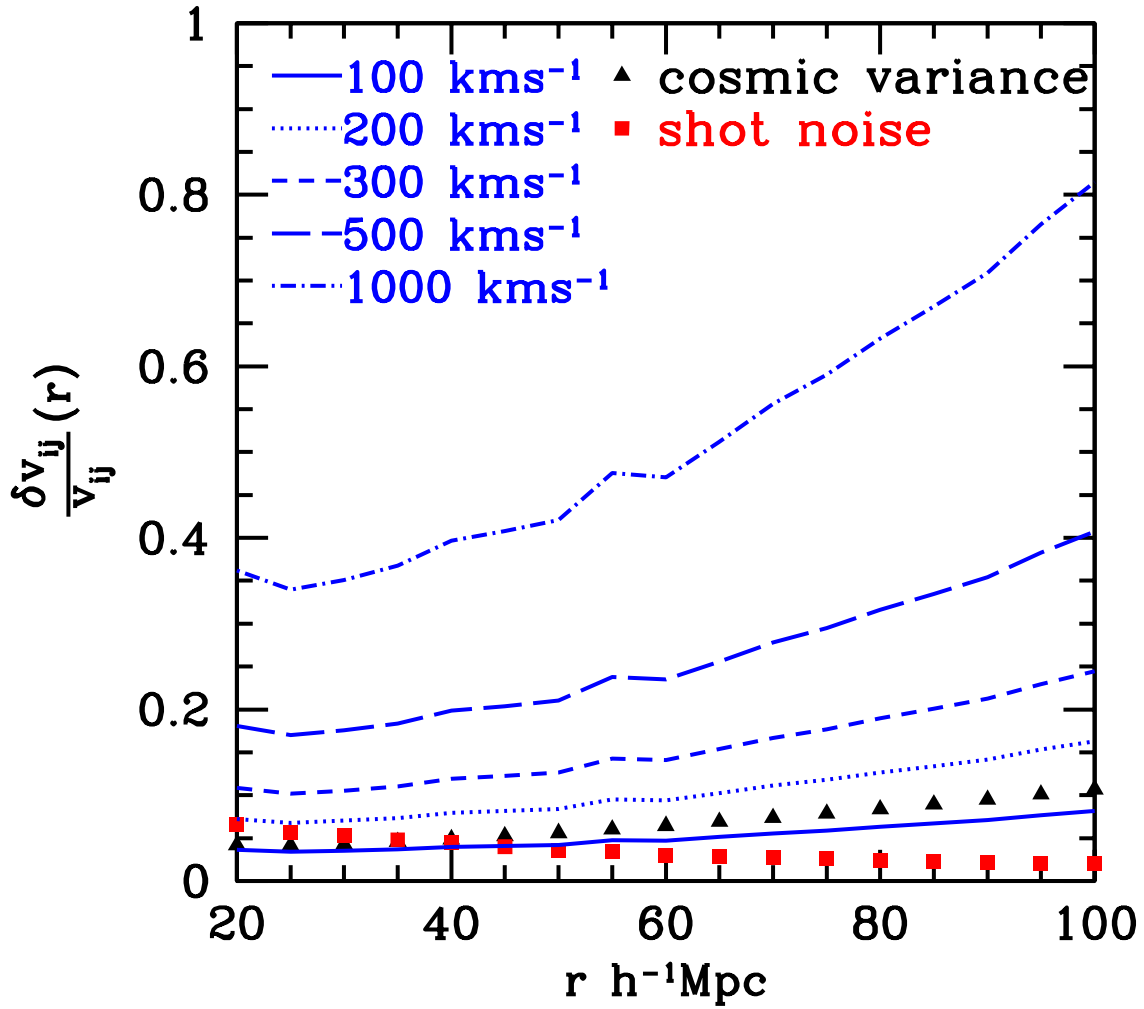
Figure 3.2 Fractional errors $\delta v_{ij}/v_{ij}$ for a cluster radial peculiar velocity survey covering 5000 square degrees: the red square points represents the Poisson error; black triangles represents cosmic variance and the Blue lines represents measurement errors (from bottom to top σ_v=100, 200, 300, 500 and 1000 km/s). Note that all the errors scales as $\sqrt{f}_{sky}$ for other survey areas.

In Eq. (3.8) we have ignored the contribution of the second (I_2) term in Eq. (2.20). At larger separations relevant here, this term, being weighted by $\xi^{DM}(r)$, is an order of magnitude smaller than the first term and hence has negligible contribution to the cosmic variance.

Again we add in quadrature the Poisson error and measurement error for n_{pair} cluster pairs and write the total covariance as

$$C_t^{\langle v_i v_j \rangle}[r_p, z_p | r_q, z_q] = C^{\langle v_i v_j \rangle}(pq) + \left[\frac{\langle v_i v_j \rangle(r,z)}{\sqrt{n^{pair}(r,z)}} \right]^2 + \left[\frac{1}{n^{pair}} \Sigma[\delta(v^2) + (\delta v)^2] \right]^2 \qquad (3.10)$$

Figure 3.3 shows the various errors in the radial peculiar velocity correlation function. The trends are similar to those for mean pairwise peculiar velocity. Measurement errors dominate the error budget for $\sigma_v > 200$ km/s. Note however the fractional errors increase with the increase in measurement errors. For $\sigma_v = 500$ km/s, the contribution of measurement errors to the total error is almost 90%, nearly double that for the case of mean pairwise peculiar velocity.

3.2 CONSTRAINTS ON DARK ENERGY PARAMETERS

Now we consider constraints on dark energy parameters for various survey areas and over a range of radial peculiar velocity errors. Following the Dark Energy Task Force report (DETF), we describe the dark energy in terms of three phenomenological parameters: its current energy density Ω_Λ, and two parameters w_0 and w_a describing the redshift evolution of its equation of state $w(a) = w_0 + (1-a)w_a$. Assuming a spatially flat universe, the set of cosmological parameters $\mathbf{p}$ on which the peculiar velocity field depends are the normalization of the matter power spectrum σ_8 (or equivalently the normalization constant B in Eq. (2.5)), the power law index of the primordial power spectrum n_S, and the Hubble parameter in units of 100 km/s/Mpc h, plus the dark energy parameters. We perform a simple Fisher matrix analysis to find constraints on these parameters obtained from the measurements of the three radial peculiar velocity statistics described in sec. 2.1.

We consider a fiducial model similar to that assumed in the DETF report (Albrecht et al., 2006) with $\sigma_8 = 0.9$, $n_S = 1$, $h = 0.7$, $\Omega_\Lambda = 0.72$, $w_0 = -1$, $w_a = 0$. To make quantitative
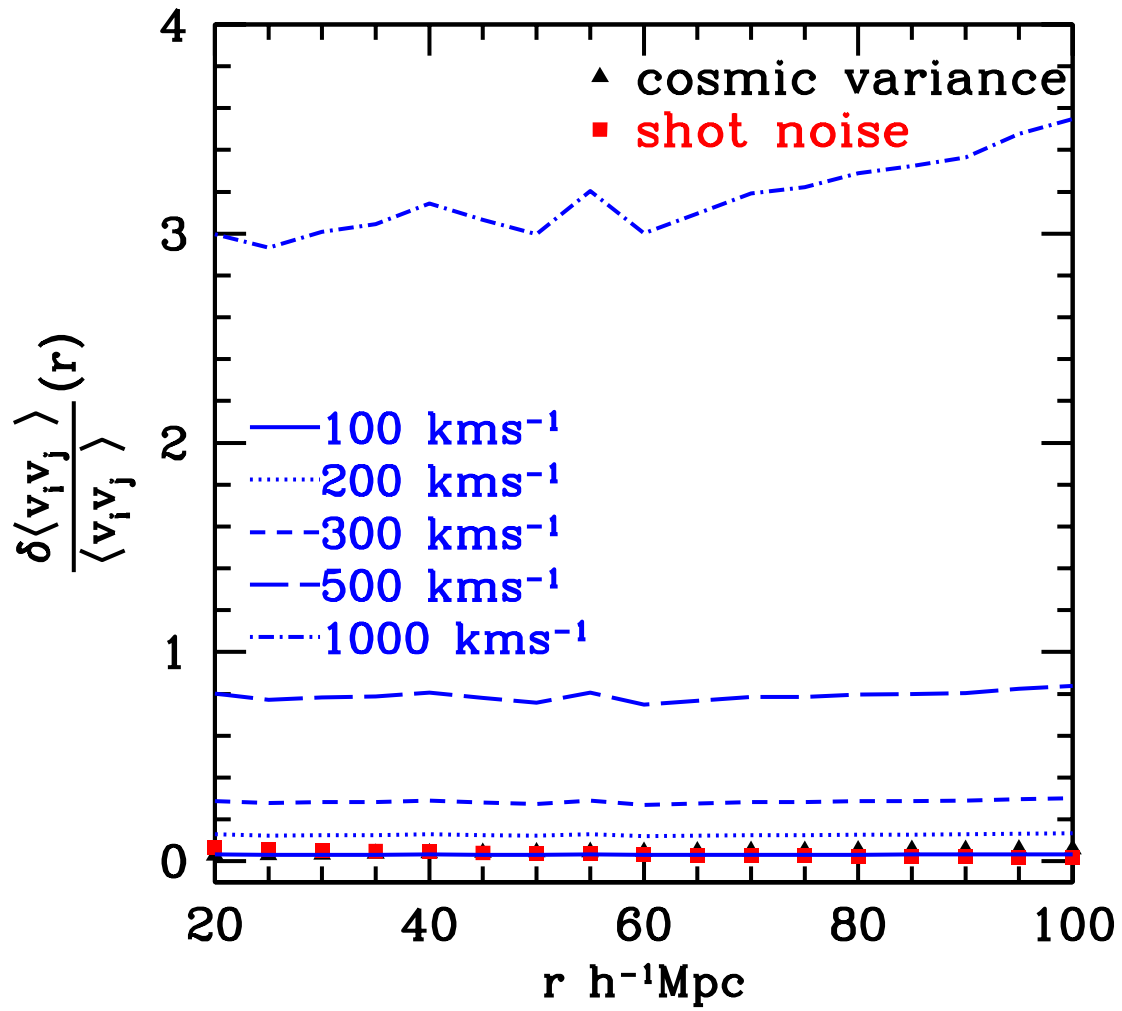
Figure 3.3 Same as in Figure 3.2 for the fractional error $\delta(\langle v_i v_j \rangle)/\langle v_i v_j \rangle$.

comparisons with the conclusions of the DETF report, we compute values for the expression $[\sigma(w_0)\sigma(w_p)]^{-1}$, which is listed in the DETF summary tables. We refer to this as the "Figure of Merit" (FOM) for convenience, although this term refers to a slightly different quantity (inverse area of the ellipse of 95% confidence limit in the $w_p - w_a$ plane) in the DETF report. Here w_p is the equation of state at the pivot point defined as $w_p = w_0 + (1 - a_p)w_a$ with $a_p = 1 + [F^{-1}]_{w_0 w_a}/[F^{-1}]_{w_a w_a}$ and F the Fisher information matrix for a given experiment.

The Fisher information matrix for each of the three statistics is

$$F_{\alpha\beta} = \sum_{i,j} \frac{\partial \phi(i)}{\partial p_\alpha} [C_t^\phi(ij)]^{-1} \frac{\partial \phi(j)}{\partial p_\beta} \qquad (3.11)$$

where ϕ stands for either n_v, $v_{ij}(r, z)$ or $\langle v_i v_j \rangle(r, z)$, $C^\phi(ij)$ is the total covariance matrix in each bin for the statistic ϕ, Eqs. (3.5), (3.7), and (3.10), and the partial derivatives are evaluated for the fiducial values of the cosmological parameters. The values i and j index the bins $[r, z]_i$ and $[r, z]_j$ for the mean pairwise peculiar velocity and radial peculiar velocity correlation function, while for $\phi = n_v$, i and j refer to $[v, z]_i$ and $[v, z]_j$. The inverse of the Fisher matrix has diagonal elements which are estimates for the variances of each cosmological parameter marginalized over the values of the other parameters, and the non-diagonal elements give the correlations between parameters.

Figure 3.4 shows the degradation of parameter constraints with increasing radial peculiar velocity error σ_v for a 4000 deg^2 survey area. It is evident that parameter constraints from v_{ij} are more robust to increases in radial peculiar velocity error than those from n_v and $\langle v_i v_j \rangle$. This is because δv_{ij} depends linearly on σ_v, while $\delta \langle v_i v_j \rangle$ varies as σ_v^2 and for n_v the distribution gets smeared with increases in σ_v. Constraints on w_0, w_a and Ω_Λ change roughly by a factor of two and the constraint on the FOM by a factor of three, for the factor of five increase in σ_v from 200 to 500 km/s. Compare this to the corresponding change for $\langle v_i v_j \rangle$: w_0, w_a and Ω_Λ constraints change roughly by a factor of 6 to 8 and the figure of merit constraint by a factor of 30 for a similar change in σ_v. For n_v, the corresponding degradation in constraints are roughly by a factor 1.5 to 3 for w_0, w_a and Ω_Λ while the figure of merit constraint degrades by roughly a factor of 4. Table 3.1 lists the constraints as a function of radial peculiar velocity error for a 4000 deg^2 survey area, while Tables 3.2 and 3.3 give constraints for 2000 deg^2 and 400 deg^2 respectively.
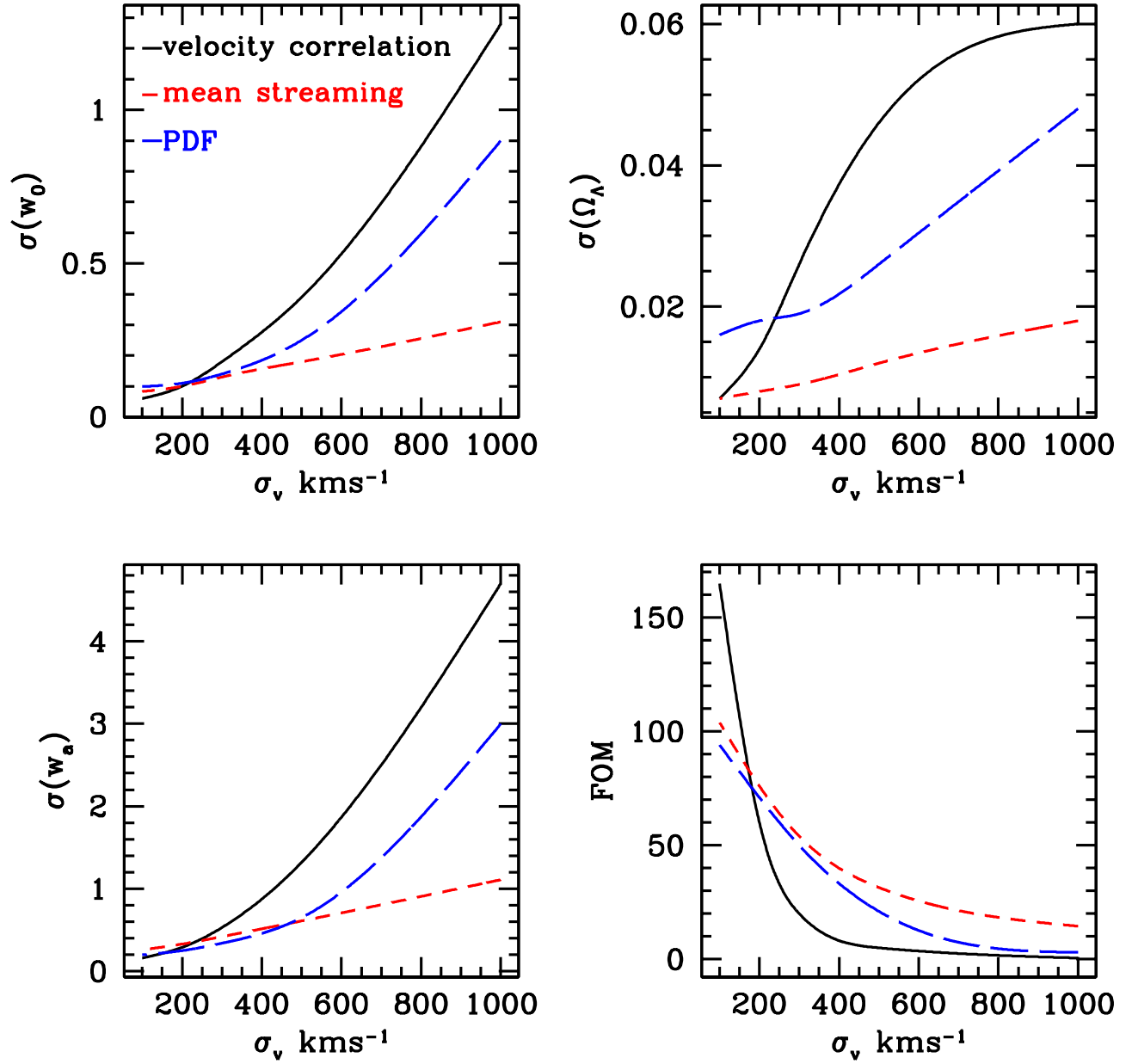
Figure 3.4 The change in 1σ parameter constraints with radial peculiar velocity error (normal distribution of width σ_v) for a 4000 $\deg^2$ survey area, for the three statistics n_v (blue dashed), v_{ij} (red short dashed) and $\langle v_i v_j \rangle$ (black solid). The four panels are for the parameters w_0 (top left), Ω_Λ (top right), w_a (bottom left), and the Figure of Merit (bottom right).

σ_v	w_0			w_a			Ω_Λ			FOM		
	$\langle v_i v_j \rangle$	v_{ij}	n_v	$\langle v_i v_j \rangle$	v_{ij}	n_v	$\langle v_i v_j \rangle$	v_{ij}	n_v	$\langle v_i v_j \rangle$	v_{ij}	n_v
100	0.06	0.083	0.099	0.16	0.26	0.2	0.007	0.007	0.016	165	104	94
200	0.1	0.1	0.11	0.29	0.33	0.25	0.014	0.008	0.018	60	76	71
300	0.18	0.13	0.14	0.53	0.42	0.34	0.026	0.009	0.019	20	54	50
500	0.39	0.18	0.25	1.32	0.61	0.65	0.046	0.012	0.026	5	31.5	21
1000	1.28	0.31	0.9	4.7	1.11	3.0	0.060	0.018	0.048	0.5	14.5	3.0

Table 3.1 Errors on dark energy parameters for a 4000 deg^2 survey area plus cosmological priors from the future CMB experiment namely, Planck and the prior on the Hubble constant $\Delta h = \pm\, 0.08$ (Freedman et al., 2001), assuming a spatially flat cosmology. Note that the figure of merit for dark energy is defined as $FOM = [\sigma(w_a)\sigma(w_p)]^{-1}$

σ_v	w_0			w_a			Ω_Λ			FOM		
	$\langle v_i v_j \rangle$	v_{ij}	n_v	$\langle v_i v_j \rangle$	v_{ij}	n_v	$\langle v_i v_j \rangle$	v_{ij}	n_v	$\langle v_i v_j \rangle$	v_{ij}	n_v
100	0.08	0.12	0.12	0.26	0.41	0.28	0.011	0.010	0.018	80	53	59
200	0.13	0.14	0.15	0.43	0.51	0.35	0.011	0.011	0.020	31	39	47
300	0.25	0.18	0.19	0.77	0.63	0.47	0.035	0.013	0.022	11	29	32
500	0.52	0.25	0.33	1.83	0.89	0.9	0.052	0.016	0.032	3	18	13
1000	1.8	0.42	1.26	6.7	1.48	4.2	0.061	0.022	0.061	0.75	7.9	1.6

Table 3.2 Same as Table 3.1, for a 2000 deg^2 survey area.

σ_v	w_0			w_a			Ω_Λ			FOM		
	$\langle v_i v_j \rangle$	v_{ij}	n_v	$\langle v_i v_j \rangle$	v_{ij}	n_v	$\langle v_i v_j \rangle$	v_{ij}	n_v	$\langle v_i v_j \rangle$	v_{ij}	n_v
100	0.13	0.20	0.2	0.45	0.72	0.51	0.019	0.015	0.023	30	22	29
200	0.24	0.25	0.24	0.76	0.92	0.64	0.034	0.017	0.026	11	16	21
300	0.41	0.31	0.31	1.39	1.15	0.85	0.048	0.020	0.031	4.0	11	14
500	0.92	0.6	0.53	3.4	1.66	1.53	0.058	0.024	0.044	1.4	0.7	5.2
1000	3.6	0.78	2.42	13.3	3.0	8.0	0.061	0.033	0.061	0.38	3.3	0.7

Table 3.3 Same as Table 3.1, for a 400 deg^2 survey area.

Note that the radial peculiar velocity correlation function $\langle v_i v_j \rangle$ provides the best constraints on the dark energy equation of state (w_0, w_a, and figure of merit) for $\sigma_v < 200$ km/s. It might be possible to achieve such values of errors in future surveys with better understanding of point source contamination and other systematics. However for more realistic near-term errors of 500 km/s, the mean pairwise peculiar velocity v_{ij} provides better constraints on dark energy parameters, and this statistic will be used in the following sections which consider how cosmological constraints will be improved by using cluster radial peculiar velocity information.

3.3 COMPLEMENTARITY OF CLUSTER RADIAL PECULIAR VELOCITIES WITH CLUSTER NUMBER COUNTS

For a given SZ survey, we can potentially obtain both cluster counts and cluster radial peculiar velocities. Given these two different data sources from the same survey, what is the joint constraint on dark energy parameters they provide? Consider a fiducial Stage II survey of 4000 galaxy clusters proposed by the DETF report (Albrecht et al., 2006) (see Table 3.5 for details), plus the addition of cluster radial peculiar velocities with measurement error $\sigma_v = 1000$ km/s, along with cosmic variance and Poisson errors to estimate the mean pairwise peculiar velocity statistic v_{ij}. This is not a particularly stringent radial peculiar velocity error, and it is likely obtainable with currently planned surveys with foreseeable follow-up observations or theoretical assumptions about cluster properties. Table 3.4 gives the constraint on the dark energy parameters derived considering cluster counts only, considering cluster radial peculiar velocities only, and the joint constraint from both. We have assumed cosmological priors from future measurements of the microwave background primary temperature fluctuations, namely the Planck satellite, a prior on the Hubble parameter $\Delta h = \pm 0.08$ (Freedman et al., 2001) and a flat spatial geometry. We find cluster radial peculiar velocities provide a better constraint on Ω_Λ and w_0 than cluster counts, even for a measurement error of $\sigma_v = 1000$ km/s. The constraint on w_a is comparable for the two probes. The combined constraint is a factor of two better than the counts-only case for Ω_Λ, w_0 and the figure of

merit, and at least a 60% improvement for w_a. The relative complementarity between the two probes is shown in Figure 3.5.

We have assumed that the cluster radial peculiar velocity and cluster density observables are statistically uncorrelated. As they will likely be obtained from the same set of clusters, it is reasonable to ask whether this is actually true. A straightforward analytic calculation shows that the cross-correlation between radial peculiar velocity and density will be proportional to the matter bispectrum, so we expect it to be small compared to the signal from the radial peculiar velocity correlations, which are proportional to the matter power spectrum. We intend to confirm this prediction from sets of large-volume numerical simulations when these are available.

3.4   COMPARISON WITH DETF PROPOSED EXPERIMENTS

The Dark Energy Task Force report (Albrecht et al., 2006) considers four different potential probes to study dark energy parameters: weak lensing(WL), baryon acoustic oscillations (BAO), cluster counts (CL) and SNIa (SN) luminosity distance measurements. The relative merits of these probes have been discussed in detail in the DETF report both for ongoing and future projects. In this section we compare our fiducial radial peculiar velocity survey with each of the four DETF probes. To assess the advantage of adding cluster mean pairwise peculiar velocity v_{ij} as a dark energy probe, we have considered only the most optimistic forecasts for the DETF surveys (i.e. survey assumptions that provide maximum constraint to the figure of merit assuming a flat universe plus the cosmological priors from the future CMB experiment, namely Planck and the prior on the Hubble constant $\Delta h = \pm 0.08$ (Freedman et al., 2001)) for each stage in the DETF report. Table 3.5 gives a brief description of the DETF surveys considered here and our corresponding assumed cluster radial peculiar velocity surveys. We have used the actual Fisher matrices used by the DETF team along with their priors for the following comparisons.
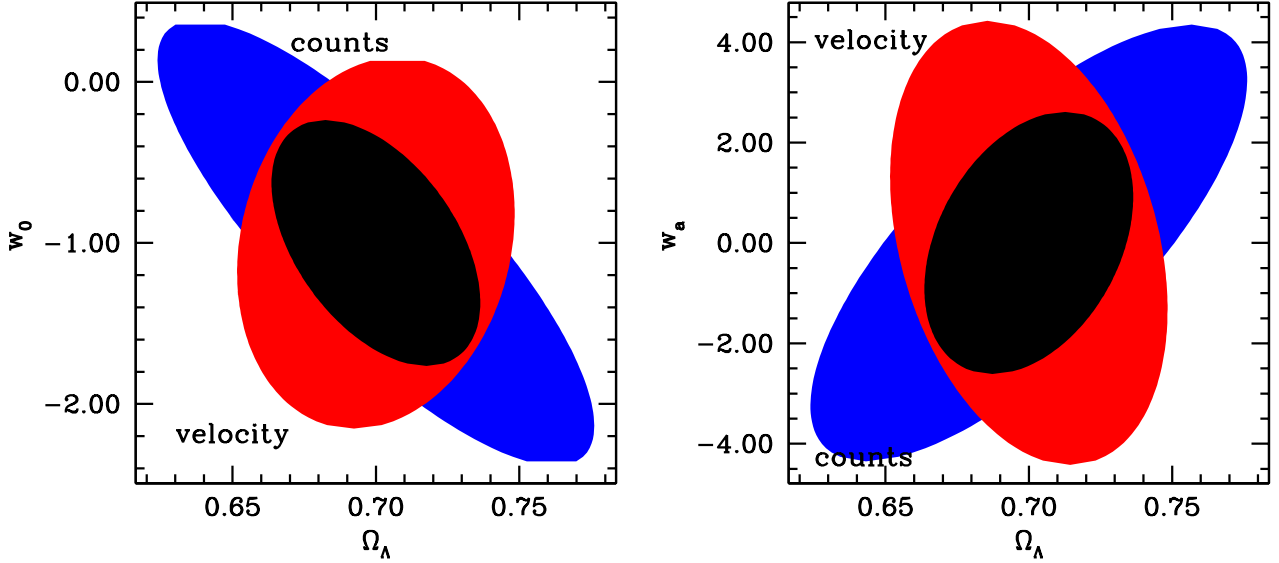
Figure 3.5 The relative complementarity of radial peculiar velocity and cluster counts. Shown are 1σ error ellipses in the $w_0 - \Omega_\Lambda$ plane (left) and the $w_a - \Omega_\Lambda$ plane (right) for 4000 clusters with normally-distributed radial peculiar velocity errors of $\sigma_v = 1000km/s$. The three ellipses are for cluster radial peculiar velocities (red), cluster counts (blue) and the combination of both (black). The cosmological priors from the Planck satellite measurement of the microwave background temperature fluctuations, a prior on the Hubble constant $\Delta h = \pm 0.08$ (Freedman et al., 2001), and a spatially flat cosmology are assumed.

Parameters	Priors	Counts	Radial Peculiar Velocity	Combined
$\Omega_\Lambda[0.7]$	0.062	0.052	0.033	0.025
$w_0[-1]$	–	0.94	0.78	0.52
$w_a[0]$	–	2.95	3.0	1.8
FOM	–	2.8	3.0	7.0

Table 3.4 Constraints for dark energy parameters for a fiducial cluster survey of 4000 clusters with radial peculiar velocity errors $\sigma_v = 1000$ km/s, for cluster number counts, cluster radial peculiar velocities, and the two combined. The cosmological priors from the Planck satellite measurement of the microwave background temperature fluctuations, a prior on the Hubble constant $\Delta h = \pm 0.08$ (Freedman et al., 2001), and a spatially flat cosmology are assumed.

3.4.1 Fiducial Radial Peculiar Velocity Surveys

In order to compare with the DETF proposed surveys, we assume three fiducial radial peculiar velocity surveys. Each survey corresponds to a particular stage of the DETF surveys. As will be shown in chapter 4, the precise estimation of the minimum mass limit of the galaxy cluster surveys is not necessary for the radial peculiar velocity surveys. The error budget of the radial peculiar velocity statistics is determined by the total number of clusters observed in the survey. At each stages, we have considered $\approx 2 \times 10^{14}$ Mpc/h as the minimum mass threshold for the galaxy cluster radial peculiar velocity surveys (except for Stage II which requires $M_{\min} > 1.7 \times 10^{14} M_\odot/h$ to obtain 4000 clusters). The other parameter to consider in a fiducial radial peculiar velocity survey is the sky coverage. As shown in Knox et al. (2004), a survey with at least three frequency meseasurements, $2 - 10\mu k$ sensitivity and arc-minute resolution will require one hour integration time for 48 sq arcmin of sky coverage to obtain a typical radial peculiar velocity error of $\approx 200 - 400$ km/s. At Stage II, we have considered a survey area of 400 deg^2. With approximately 600 hr of observation time per year, a 400 deg^2 area can be covered in 1-2 years of observation. Similarly a stage III, 2000 deg^2 will require about 5 years of observations and a Stage IV will require 10 years of observations. Note that the numbers quoted here should be considered as a rough estimate. The ultimate cluster radial peculiar velocity survey strategy will be determined by a detailed analysis of the measurement errors and advancement in detector technology.

To be consistent with the DETF report, the total number of clusters for each survey corresponds to $\sigma_8 = 0.9$. If $\sigma_8 = 0.76$ (Spergel et al., 2007) is used, then the corresponding number of clusters decreases by a factor of 30%. However, a radial peculiar velocity survey is sensitive to only the number of detected clusters and not the volume of the survey. So our conclusions will still be valid if the survey area is increased to compensate for a lower value of σ_8. Note that in going from Stage II to Stage IV the dark energy constraints do not improve by a factor of $\sqrt{f_{sky}}$. This is because the other cosmological parameters (which are marginalized over) are strongly correlated with the dark energy parameters.

Stages	VEL	WL	SNIa	Cl	BAO
II	$N_{cl} = 4000$, $f_{\rm sky} = 0.01$ $M_{min} > 1.7 \times 10^{14} M_\odot/h$ z=0.1-1.4	$f_{\rm sky} = 0.0042$	SNLS 700 SNIa z=0.1-1.0	$N_{cl} = 4000$ $f_{\rm sky} = 0.005$	None
III	$N_{cl} = 15000$, $f_{\rm sky} = 0.05$ $M_{min} > 2.0 \times 10^{14} M_\odot/h$ z=0.1-1.4	DES $f_{\rm sky} = 0.1$	2000 SNIa Spectroscopy	$N_{cl} = 30000$	$f_{\rm sky} = 0.1$
IV	$N_{cl} = 30000, f_{\rm sky} = 0.1$ $M_{min} > 2.0 \times 10^{14} M_\odot/h$ z=0.1-1.4	SKA-o $f_{\rm sky} = 0.5$ $z = 0.1–1.7$	Space 2000 SNIa	$N_{cl} = 30000$ $f_{\rm sky} = 0.5$ $z = 0–1.5$	SKA-o $f_{\rm sky} = 0.5$

Table 3.5 Parameters defining various surveys discussed in the DETF report, plus various cluster radial peculiar velocity surveys discussed here.
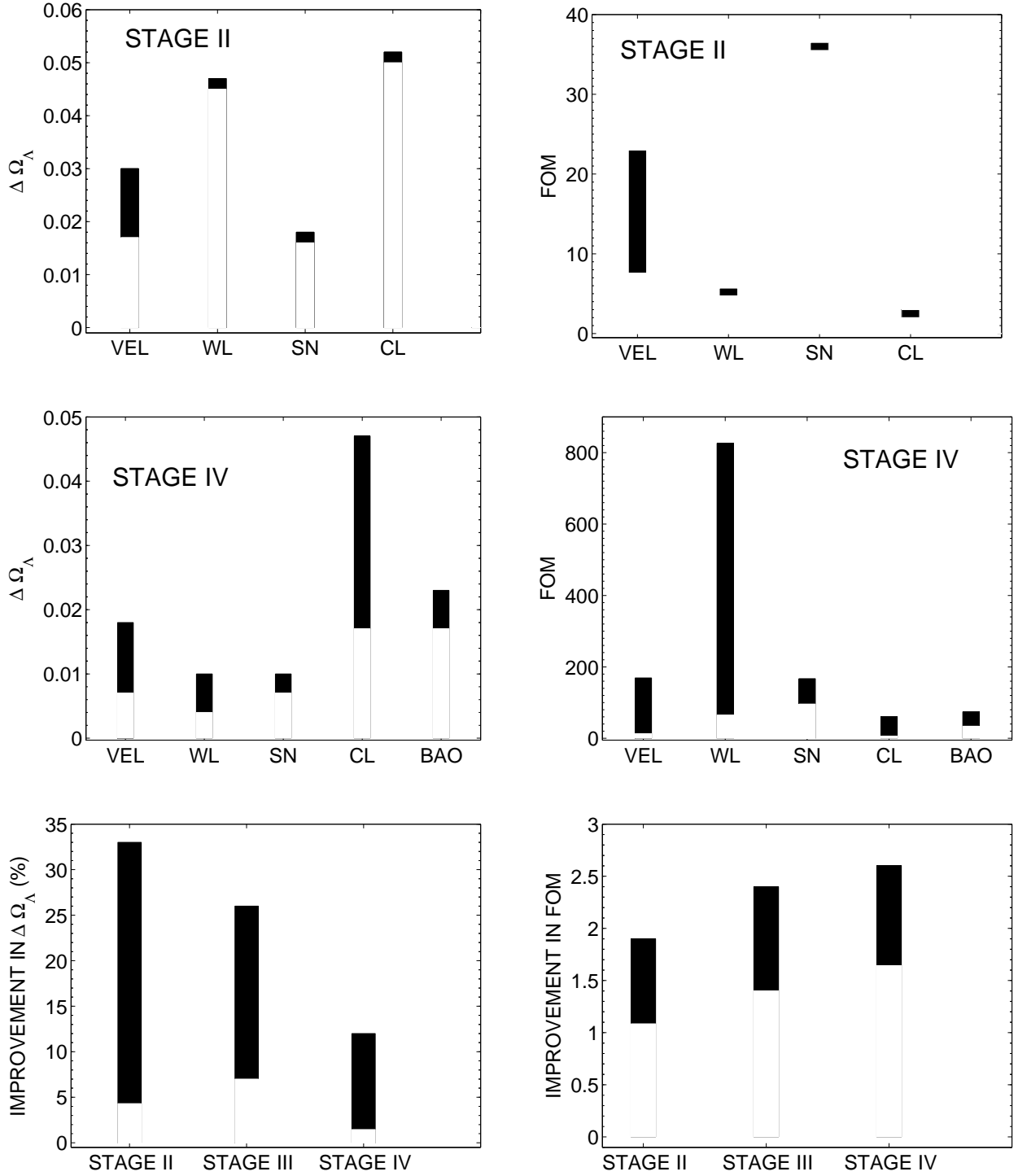
Figure 3.6 A comparison of the error in the dark energy density $\delta\Omega_\Lambda$ and the dark energy figure of merit obtained from radial peculiar velocity statistics with that from DETF probes. The top two panels are for Stage II experiments; the dark region shows the range in the parameter error for the DETF- assumed ranges in the measurement errors. For cluster radial peculiar velocities we assume a range from $\sigma_v = 200$ to 1000 km/sec. The middle panels show the results for Stage IV measurements. The bottom panels show the relative improvement in parameter measurements at Stage IV when cluster radial peculiar velocities are combined with all of the other DETF probes.

42

3.4.2 Results

A comparison of radial peculiar velocity with other probes is shown in Figure 3.6. The cosmological priors from the future CMB experiment namely, Planck and the prior on the Hubble constant $\Delta h = \pm 0.08$ (Freedman et al., 2001) and a spatially flat cosmology are assumed for all the probes. Each plot shows a range of parameter errors for each experiment, corresponding to cluster radial peculiar velocity measurement errors ranging between 200 and 1000 km/sec, and other measurement errors as in the DETF report. At Stage II, radial peculiar velocity measurements provides a competitive constraint on Ω_Λ compared to SNIa, and much better constraints than weak lensing or cluster number counts. Even a modest radial peculiar velocity survey would yield a factor of two better constraints on Ω_Λ than cluster counts or weak lensing. Cluster radial peculiar velocities also provide two to three times better constraints to the figure of merit compared to weak lensing or cluster counts at Stage II. Ultimately at Stage IV, however, weak lensing provides the most accurate measurements of dark energy density and best the figure of merit. But constraints from radial peculiar velocity are competitive with those from supernovae and better than those from cluster counts or baryon acoustic oscillations. Stage II and III experiments yield an average 20% improvement in cosmological parameter determination, and Stage IV about a 7% improvement, when radial peculiar velocity information is combined with the rest of the dark energy experiment results. This corresponds to an improvement by factors of 1.5 to 2.5 in the dark energy figure of merit. These types of statistical comparisons of course assume zero systematic errors; cluster radial peculiar velocities will ultimately be more valuable than these numbers indicate, due to their completely different systematic errors from the other challenging techniques. All of these methods will in the end be dominated by systematic and not statistical errors.

3.5 CHAPTER SUMMARY

In this chapter, we have assesed the merit of radial peculiar velocities as a dark energy probe. We have used the theoretical models of various radial peculiar velocity statistics described in chapter 2 and have assumed various fiducial radial peculiar velocity surveys for this purpose. The results show that cluster radial peculiar velocities have the potential to constrain several dark energy parameters. We compare three radial peculiar velocity statistics (the distribution of radial velocities, the mean pairwise peculiar velocity, and the radial peculiar velocity correlation function) and analyze the relative merits of these statistics in constraining dark energy parameters. Of the three statistics, mean pairwise peculiar velocity provides constraints that are least sensitive to radial peculiar velocity errors: the constraints on parameters degrades only by a factor of two when the random error is increased from 100 to 500 km/s. We also compare cluster velocities with other dark energy probes proposed in the Dark Energy Task Force report. For cluster radial peculiar velocity measurements with realistic priors, the eventual constraints on the dark energy density, the dark energy equation of state and its evolution are comparable to constraints from supernovae measurements, and better than cluster counts and baryon acoustic oscillations; adding radial peculiar velocity to other dark energy probes improves constraints on the figure of merit by more than a factor of two. For upcoming SZ galaxy cluster surveys, even radial peculiar velocity measurements with errors as large as 1000 km/s will substantially improve the cosmological constraints compared to using the cluster number density alone.

4.0 SYSTEMATIC ERRORS IN SUNYAEV-ZELDOVICH SURVEYS OF GALAXY CLUSTER RADIAL PECULIAR VELOCITIES

Cluster radial peculiar velocities trace the large-scale radial peculiar velocity field arising from structure formation in the universe, and their radial peculiar velocities are expected to be only weakly dependent on cluster mass. Therefore we expect that dark energy constraints based on cluster radial peculiar velocities will be far less sensitive to systematic errors in estimating the mass limit of any particular cluster catalog. We verify this expectation here. While changing a cluster catalog mass cutoff by 20% can change the total number of clusters by a factor of two, it only changes cluster radial peculiar velocity statistics by a few percent. The bias on cosmological parameters from uncertainties in cluster selection will be much milder for cluster radial peculiar velocity statistics than cluster number counts, and the power of radial peculiar velocities to constrain dark energy is significant, even for modest radial peculiar velocity errors as large as 500 km/sec as already shown in chapter 3.

The kinematic SZ signal measures the total cluster baryon momentum, not directly the cluster radial peculiar velocities. Extracting the radial peculiar velocities from SZ measurements will require additional data to estimate the cluster baryon mass (Sehgal et al., 2005); cluster X-ray temperatures are one likely route, while another route is a suspected tight correlation between tSZ flux and gas temperature. But these measurements have potential systematic errors of their own; previous studies (Diaferio et al., 2005a; Knox et al., 2004) have shown that X-ray temperature systematically overestimates electron temperature by 20% to 40% (this particular systematic difference arises because while X-ray temperature is luminosity weighted, electron temperature is mass weighted), while correlations seen in numerical simulations may not incorporate all of the relevant physical effects in real galaxy clusters. Observing the SZ signal will also be complicated by point source contamination,

which may induce a different systematic error. Using simple models for these errors, we show that they give potentially significant biases to cosmological parameters if not properly accounted for.

In this work, we focus on two particular galaxy cluster radial peculiar velocity statistics: the correlation function of the radial peculiar velocity components perpendicular to the line connecting a cluster pair, $\langle v_i v_j \rangle_\perp (r)$, and the mean pairwise peculiar velocity $v_{ij}(r)$; each is a function of the separation between two galaxy clusters r and redshift z. The theoretical model for these statistics have been discussed in chapter 2 and both of these statistics are considered as probes of dark energy in chapter 3. (We drop the perpendicular subscript from the correlation function for convenience). Sections 4.1 and 4.2 consider the systematic errors arising from uncertainty in the cluster mass selection function, and from systematic errors in radial peculiar velocity estimates due to misestimates in galaxy cluster physics or contamination by foreground emission. Section 4.3 then computes the resulting biases in determining dark energy parameters for each source of error, while section 4.4 briefly considers self-calibration techniques in the context of cluster radial peculiar velocities.

4.1   SYSTEMATIC ERRORS FROM MASS MISESTIMATES

Cluster number counts above a given mass are prone to systematic errors in the inferred mass lower limit $M_{\min}$. As pointed out in Francis et al. (2005), a 20% systematic error in the measurement of cluster masses leads to more than 2σ systematic bias in the estimation of cosmological parameters. In this section, we address the issue of mass selection in the context of cluster radial peculiar velocities. The radial peculiar velocity statistics depend on $M_{\min}$ through the normalization term in theoretical halo models.

In order to model the effect of mass selection, we assume that for a given survey, cluster masses are all mis-estimated by a constant fraction. This leads to a corresponding difference in the inferred cluster mass threshold for number statistics and the resulting systematic bias in dark energy parameters studied in Francis et al. (2005). However, clusters of any mass generally trace the large-scale radial peculiar velocity field, so biased cluster mass estimates

should have little effect on cluster radial peculiar velocity statistics. The two statistics $\langle v_i v_j \rangle_\perp (r)$ and $v_{ij}(r)$ can both be estimated accurately with analytic approximations based on the halo model and on nonlinear perturbation theory (Sheth et al., 2001b; Sheth and Diaferio, 2001; Sheth et al., 2001a); a summary of these approximations is given in chapter 2. To approximate the effect of cluster mass mis-estimates, assume that for a given sample of galaxy clusters detected via the SZ effect, all of the inferred masses are off by 40%. We compute the radial peculiar velocity statistics for clusters with both the actual mass cutoff and the inferred one using the halo model, and find that this large change in mass selection has minimal effect: a 40% offset in minimum mass estimate gives only 2% to 4% change for both radial peculiar velocity statistics. Fig. 4.1 displays the difference. Therefore, even if the mass determination of clusters is uncertain at this level, it will result in only small changes in the underlying cosmological models selected by the data. We emphasize that this is in marked contrast to the case for cluster number counts. (Although self-calibration techniques provide a possible remedy to the cluster count mass-selection bias (Majumdar and Mohr, 2004; Lima and Hu, 2005, 2004), it requires at minimum a determination of the scatter and bias in cluster photometric redshifts to better than 0.03 and 0.003 respectively in order for self-calibration to work (Lima and Hu, 2007). The evolution of cluster properties with redshift also must be of an assumed form.)

4.2   SYSTEMATIC ERRORS FROM RADIAL PECULIAR VELOCITY MISESTIMATES

Aside from errors in the inferred cluster mass, which the previous section shows has little effect on cluster radial peculiar velocity statistics, the cluster radial peculiar velocities themselves are also subject to systematic errors. The state of some small volume of gas is characterized by its temperature, density, and bulk velocity. Measurements of the SZ distortions of the radiation passing through this gas at three frequencies often have a physical degeneracy which enable measurement of only two of these gas quantities (Aghanim et al., 2003; Holder, 2004; Sehgal et al., 2005); in particular, this is true for the ACT frequency
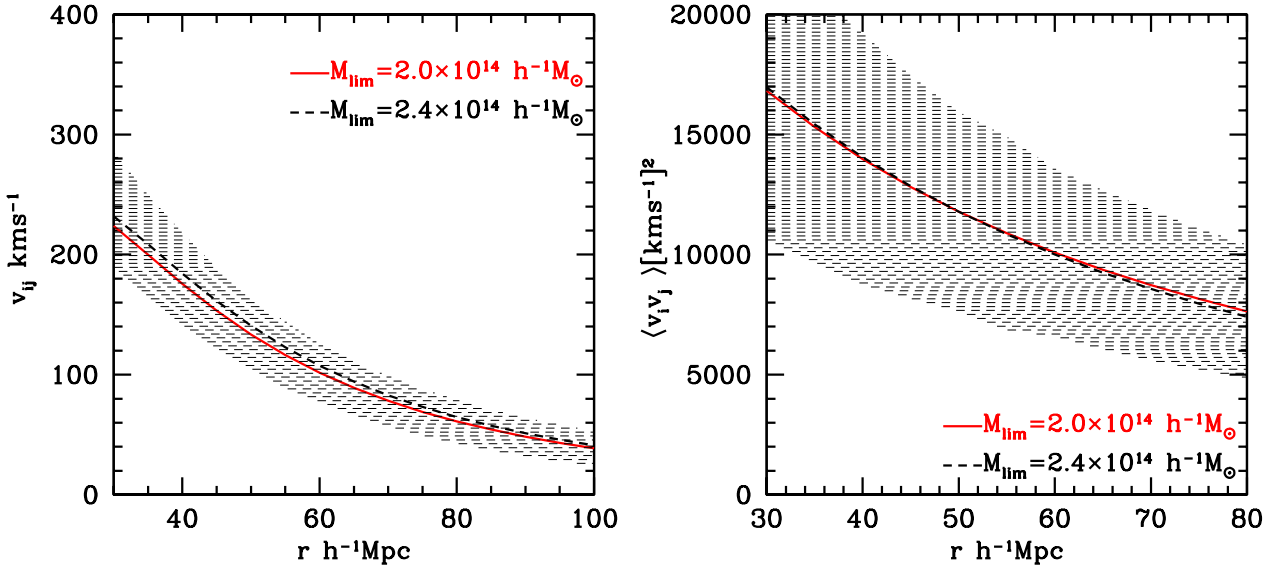
Figure 4.1 Radial Peculiar Velocity statistics for all clusters larger than a minimum mass $M_{\min}$, evaluated for two values of $M_{\min}$ differing by 40%. (a) The mean pairwise peculiar velocity and (b) the perpendicular radial peculiar velocity correlation function.

bands at 145, 220, and 280 GHz. To get the third (typically the gas radial peculiar velocity, the quantity of interest here), additional information must be obtained. The most convenient source is a direct determination of gas temperature, either through X-ray observations or through a theoretical correlation of gas temperature and total tSZ distortion. In addition, extracting the SZ signal accurately in the presence of foreground emission, particularly from infrared point sources (Borys et al., 2003; Coppin et al., 2006; Scott et al., 2008), can also lead to systematic errors in inferred radial peculiar velocities if the point sources are not adequately characterized.

Typically the X-ray temperature T_X of galaxy clusters differs appreciably from the electron gas temperature T_e. Numerical simulations (Diaferio et al., 2005a; Hansen, 2004) indicates that using T_X as a proxy for T_e leads to over-estimation of radial peculiar velocities inferred from SZ measurements by 10 to 40%. This bias is because the estimate of radial peculiar velocity gets weighted by the ratio of pressure-weighted temperature to mass-weighted temperature (Knox et al., 2004). In order to quantify the effect of the difference between T_X and T_e in the estimation of radial peculiar velocity, we use the relation $\langle v \rangle_{\theta_b} \propto \langle T_e \rangle_{\theta_b}$

for an unresolved cluster (Diaferio et al., 2005a). The quantities $\langle .. \rangle$ indicates the average quantities over the beam size θ_b; for brevity we drop the average symbols and assume beam-averaged quantities in this section. We assume the X-ray temperature T_X and the electron temperature T_e are simply related through a linear relation $T_e \equiv a + bT_X$. Numerical studies find $(a, b) = (0.17\,\text{keV}, 0.69)$ when averaged within the virial radius for a cluster and $(0.18\,\text{keV}, 0.53)$ when averaged within three times the virial radius (Diaferio et al., 2005a). The relation between the radial peculiar velocity derived from the X-ray temperature and from the electron temperature is just

$$v_{\text{true}} = (a/T_X + b)v_{\text{obs}}, \tag{4.1}$$

where v_{true} is the radial peculiar velocity inferred from the electron temperature and v_{obs} is the radial peculiar velocity inferred from the X-ray temperature; SZ cluster radial peculiar velocity measurements will be correct when using the electron temperature. For a cluster of temperature $T_X = 3$ keV, the first term is around 10% of the second term, and the relative contribution decreases further for more massive clusters; we thus neglect the first term, leaving the true radial peculiar velocity proportional to the observed radial peculiar velocity,

$$v_{\text{obs}} = \beta v_{\text{true}} \tag{4.2}$$

with $\beta \equiv 1/b$. For the given values of $b = 0.69$ and 0.53, the cluster radial peculiar velocity derived using a measured X-ray temperature will be 1.4 and 1.9 times larger than the true radial peculiar velocity derived from the gas temperature. To the extent that we will not know perfectly the T_X–T_e relation, our inferred cluster radial peculiar velocities will be dominated by our fractional mis-estimate of β: a 10% overestimate of β gives about a 10% overestimate of the cluster radial peculiar velocity. Note that for a sample of clusters, b (and thus β) will likely be easier to infer than a since it represents the slope of the T_e–T_X relation, rather than an extrapolation of this relation to $T_X = 0$.

Point sources can be modeled in the same way; Aghanim et al. (2005) discusses the fact that systematic errors in radial peculiar velocity from point sources can be significant even though their contribution to statistical error may be small. We again assume an observed

radial peculiar velocity proportional to the true radial peculiar velocity; we also add a constant offset, $v_{\text{true}} = \beta v_{\text{obs}} - v_{\text{off}}$. Numerical simulations with large numbers of clusters suggest the value $\beta = 2$, perhaps slightly larger than that expected from X-ray temperatures.

Fig. 4.2 shows the effect of systematic errors on the pairwise mean peculiar velocity and the perpendicular radial peculiar velocity correlation function, as determined from the lightcone output of the VIRGO simulation (Evrard et al., 2002). The dashed line surrounded by the shaded region shows the actual value of the statistics as drawn from the simulation, with inferred statistical errors assuming a radial peculiar velocity error of $\sigma_v = 300$ km/s, plus cosmic variance and Poisson noise for a 5000 deg^2 sky area; see chapter 2 for details. The higher offset solid lines show the same quantities except with the individual cluster radial peculiar velocities biased using $\beta = 1.7$ and $\beta = 2$, while the dot-dash line shows a constant radial peculiar velocity offset corresponding to $v_{\text{off}} = 30$ km/s. Note that a constant offset has no effect on the mean pairwise peculiar velocity, and a relatively small effect on the correlation function compared to the shift due to β. Constant radial peculiar velocity offsets would also be evident in the radial peculiar velocity distribution function, since the entire cluster radial peculiar velocity sample should have zero mean as shown in the probability distribution function galaxy cluster radial peculiar velocities in chapter 2. For the mean pairwise peculiar velocity, a bias corresponding to $\beta = 1.7$ shifts the radial peculiar velocity statistic by about 1σ statistical error, while the effect is substantially larger in the radial peculiar velocity correlation function.

In the case of X-ray temperature, we already have reasonable estimates of the difference in X-ray and electron temperatures, from both analytic and numeric calculations; the actual bias in radial peculiar velocity statistics will be due only to our error in understanding this relation, which should be much smaller than the size of the effect displayed in Fig. 4.2. The extent to which we can characterize and understand the effect of the point source population is currently under investigation and requires a better observational characterization of the relevant sources and their correlation with galaxy clusters. Ultimately the point sources can be spatially resolved by observations at sub-millimeter wavelengths, but doing this over a survey region of several hundred square degrees is likely impractical in the foreseeable future.

The numbers presented here are a worst-case scenario, should we have a gross misunder-

standing of cluster physics, or completely fail to recognize a substantial source of systematic error in cluster radial peculiar velocity estimates. We have simply assumed that we do not account for systematic offsets in X-ray temperature compared to electron temperature, or systematic errors in cluster radial peculiar velocity estimates due to point source contamination. We already have detailed estimates of the former, based on simulations, and the latter is under active study (Lin and Mohr, 2007; Righi et al., 2008; Scott et al., 2008; Wilson et al., 2008). We can also hope to measure these systematic effects directly from the cluster radial peculiar velocity data; such "self-calibration" will be considered below.

4.3   BIAS IN DARK ENERGY PARAMETERS

In order to study the bias induced in dark energy parameters from systematic errors in the radial peculiar velocity statistics, we consider a fiducial cosmology described by the set of cosmological parameters $\mathbf{p}$ on which the radial peculiar velocity field depends: the normalization of the matter power spectrum σ_8, the power law index of the primordial power spectrum n_S, and the Hubble parameter h, plus the dark energy parameters namely, Ω_Λ and two parameters w_0 and w_a describing the redshift evolution of its equation of state $w(a) = w_0 + (1-a)w_a$. We assume Gaussian priors with variances of $\Delta\sigma_8 = 0.09$, $\Delta n_S = 0.015$ (Spergel et al., 2007) and $\Delta h = 0.08$ (Freedman et al., 2001). We then perform a simple Fisher matrix analysis to find the bias on these parameters from measurements of our two radial peculiar velocity statistics with small systematic errors.

The Fisher information matrix for each of the two statistics is

$$F_{\alpha\beta} = \sum_{i,j} \frac{\partial \phi(i)}{\partial p_\alpha} [C_t^\phi(ij)]^{-1} \frac{\partial \phi(j)}{\partial p_\beta} \tag{4.3}$$

where ϕ stands for either $v_{ij}(r,z)$ or $\langle v_i v_j \rangle(r,z)$, $C^\phi(ij)$ is the total covariance matrix in each bin. A detail description of the statistics is given in chapter 2 and its covariance calculation are given in the appendices- B & C. Assuming the systematic offsets in the radial peculiar

velocity statistics are small so that the Gaussian assumption is valid, the bias in parameter p can be written as (Rudd et al., 2008)

$$\delta p_\alpha = \sum_\beta [F^{-1}]_{\alpha\beta} \sum_{i,j} \phi(i)_{\text{sys}} [C_t^\phi(ij)]^{-1} \frac{\partial \phi(j)}{\partial p_\beta} \tag{4.4}$$

where $\phi_{\text{sys}} = \delta\phi$ the difference between the biased and the true value. Note that the assumption of small offsets may not be valid in our case; nevertheless it gives us an estimate of the magnitude of the bias.

Tables 4.1 and 4.2 show the dark energy parameter biases for each of the two radial peculiar velocity statistics, and for each of two survey areas. Assuming a measurement error normally distributed with $\sigma_v = 300$ km/s, both v_{ij} and $\langle v_i v_j \rangle$ put tight constraints on dark the energy density and relatively weak constraints on its equation of state in the absence of any systematic bias. The systematic bias for w_0 and w_a is only marginally greater than the no-bias statistical error for $\beta = 2$, for both the statistics and the survey areas considered. Except for v_{ij} for a 4000 deg^2 survey, the systematic bias for w_a is 3 times greater than the statistical error. However for Ω_Λ the bias is substantial for all survey areas and both the statistics; v_{ij} generally gives a smaller bias on Ω_Λ than $\langle v_i v_j \rangle$. While Ω_Λ is strongly constrained by other measurements, one virtue of a radial peculiar velocity survey is a completely independent constraint on Ω_Λ. Introducing prior cosmological constraints consistent with projections for the Planck satellite, radial peculiar velocity statistics will also provide competitive constraints on w_0 and w_a as shown in chapter 3. Hence it is important to determine whether self-calibration of unknown systematic errors will help reduce the bias in determining these parameters.

4.4   SELF-CALIBRATION OF SYSTEMATIC OBSERVABLES

One potential method for dealing with systematic errors is to adopt some reasonable parameterized model for the errors, then solve for these systematic error parameters along with the cosmological parameters of interest, given the data in hand. This technique has been investigated extensively in the case of galaxy cluster number counts (Majumdar and Mohr,

survey deg²	p	$\sigma(p)$	$\delta(p)$ $\beta = 1.4$	$\delta(p)/\sigma(p)$ $\beta = 1.4$	$\delta(p)$ $\beta = 1.7$	$\delta(p)/\sigma(p)$ $\beta = 1.7$	$\delta(p)$ $\beta = 2.0$	$\delta(p)/\sigma(p)$ $\beta = 2.0$
	$\Omega_\Lambda\,[0.7]$	0.03	0.04	1.46	0.075	2.56	0.11	3.7
4000	$w_0\,[-1]$	0.35	0.15	0.43	0.35	0.75	0.37	1.1
	$w_a\,[0]$	0.56	0.65	1.15	1.13	2.0	1.6	2.9
	$\Omega_\Lambda\,[0.7]$	0.034	0.07	2.0	0.12	3.5	0.17	5.1
400	$w_0\,[-1]$	0.84	0.07	0.08	0.12	0.14	0.17	0.2
	$w_a\,[0]$	1.5	0.7	0.5	1.24	0.8	1.8	1.2

Table 4.1 The statistical errors $\sigma(p)$ in dark energy parameters Ω_Λ, w_0, and w_a, and the bias $\delta(p)$ in these parameters due to systematic error in cluster radial peculiar velocity estimates, using the mean pairwise peculiar velocity $v_{ij}(r)$. The fiducial cosmological model has $n_s = 1$, $\sigma_8 = 0.9$, $h = 0.7$, $\Omega_\Lambda = 0.7$, $w_0 = -1$, and $w_a = 0$, with prior normal errors of $\Delta n_s = 0.015$, $\Delta\sigma_8 = 0.09$ and $\Delta h = 0.08$ and a spatially flat universe assumed. No priors on dark energy parameters are included. Cluster radial peculiar velocity normal errors of $\sigma_v = 300$ km/s are assumed.

survey deg²	p	$\sigma(p)$	$\delta(p)$ $\beta = 1.4$	$\delta(p)/\sigma(p)$ $\beta = 1.4$	$\delta(p)$ $\beta = 1.7$	$\delta(p)/\sigma(p)$ $\beta = 1.7$	$\delta(p)$ $\beta = 2.0$	$\delta(p)/\sigma(p)$ $\beta = 2.0$
	$\Omega_\Lambda\,[0.7]$	0.038	0.22	5.7	0.43	11.5	0.68	17.8
4000	$w_0\,[-1]$	0.41	0.09	0.22	0.17	0.43	0.28	0.69
	$w_a\,[0]$	0.71	0.31	0.43	0.6	0.85	0.96	1.35
	$\Omega_\Lambda\,[0.7]$	0.08	0.2	2.7	0.4	5.3	0.7	8.4
400	$w_0\,[-1]$	0.96	0.11	0.12	0.22	0.23	0.35	0.36
	$w_a\,[0]$	1.9	0.5	0.27	1.01	0.54	1.6	0.86

Table 4.2 The same as in Table 4.1, but for the radial peculiar velocity correlation function.
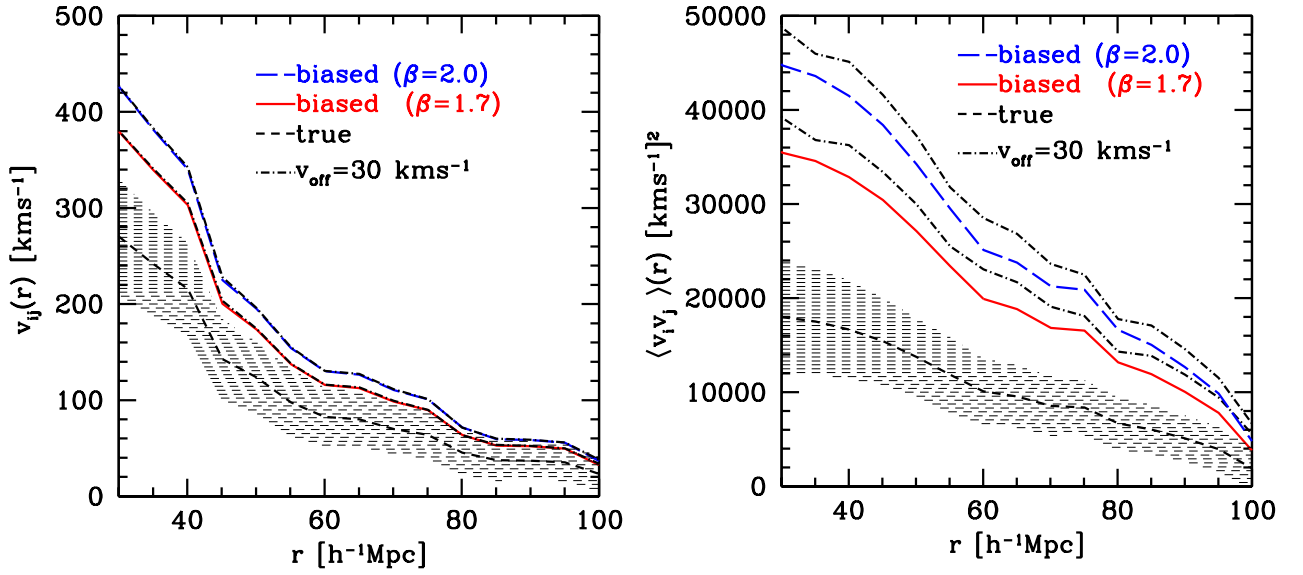
Figure 4.2 The effect of systematic errors for the mean pairwise peculiar velocity (left) and the radial peculiar velocity correlation function (right). The shaded region with the dashed line shows each statistic obtained from the Virgo dark-matter simulation. The effect of unmodeled systematic bias between estimated and actual gas temperature are shown with the red solid line ($\beta = 1.7$) and the blue dashed line ($\beta = 2$). Also shown as dot-dashed black lines are the effects of a constant radial peculiar velocity offset $v_{\mathrm{off}} = 30$ km/sec. Note that v_{ij} has the advantage of being insensitive to radial peculiar velocity offsets.

2004; Lima and Hu, 2004, 2005); in this context it is often referred to as "self calibration". For cluster number counts, the number count data itself is not sufficient to constrain the systematic errors, but the addition of cluster spatial correlations is, providing the parameterized model of the systematic errors is realistic.

In this section we study the self-calibration of the variable that models systematic radial peculiar velocity errors due to X-ray temperature offset or imperfect point-source subtraction. To this end, we allow β to co-vary with the cosmological parameters. To allow for redshift evolution of β, we write $\beta = \beta_0/(1+z)^\gamma$ with β_0 being the value of β at $z = 0$. We choose a fiducial value of $\gamma = 0$, while fiducial values of $\beta_0 = 1.4$, 1.7, and 2 correspond to the three values of β considered in sec. 4.3. We also assume a mild normal distribution prior on these parameters with a variance of 50% . We envisage such moderate priors can be obtained using numerical simulation studies and follow-up observations. We perform a Fisher matrix analysis using Eq. (4.3) with the cosmological parameters plus the two systematic parameters β_0 and γ, then marginalize over β_0 and γ to get the dark energy parameter constraints. Cosmological parameters will necessarily have their constrains weakened, but if the model for the systematic errors is an accurate representation of the actual systematic errors, the bias in cosmological parameters will be reduced.

Results are shown in Table 4.3 and 4.4 for the two statistics v_{ij} and $\langle v_i v_j \rangle$ and two survey areas. For v_{ij}, the degradation in the constraint on Ω_Λ varies from 3% to 10% for $\beta = 1.4$ to 2.0. For w_0, the degradation varies from 6% to 18% and for w_a it is 27% to 40% for a 4000 deg^2 survey area. For 400 deg^2 the relative degradation of the constraints is smaller since the statistical error is larger than for greater sky area. For $\langle v_i v_j \rangle$ the degradation is larger than for v_{ij} since it varies as β^2. Table 4.5 gives the constraints on the parameters β_0 and γ that are used to describe the systematic radial peculiar velocity errors: v_{ij} gives 20% and 30% constraints on β_0 and 20% and 40% constraint on γ for the two survey areas 4000 and 400 deg^2 respectively.

survey	p	$\sigma(p)$	$\Delta_s(p)$	$\Delta_s(p)/\sigma(p)$	$\Delta_s(p)$	$\Delta_s(p)/\sigma(p)$	$\Delta_s(p)$	$\Delta_s(p)/\sigma(p)$
deg^2			$\beta = 1.4$	$\beta = 1.4$	$\beta = 1.7$	$\beta = 1.7$	$\beta = 2.0$	$\beta = 2.0$
	$\Omega_\Lambda\,[0.7]$	0.029	0.03	1.03	0.031	1.07	0.032	1.10
4000	$w_0\,[-1]$	0.35	0.37	1.06	0.38	1.08	0.41	1.175
	$w_a\,[0]$	0.56	0.71	1.27	0.75	1.35	0.78	1.4
	$\Omega_\Lambda\,[0.7]$	0.034	0.036	1.06	0.036	1.06	0.037	1.07
400	$w_0\,[-1]$	0.84	0.87	1.04	0.89	1.06	0.93	1.11
	$w_a\,[0]$	1.5	1.7	1.13	1.9	1.27	2.2	1.46

Table 4.3 Constraints with the self-calibration of the systematic parameters β_0 and γ for v_{ij}. A 50% prior on both the systematic parameters is assumed. Note that $\Delta_s(p)$ & $\sigma(p)$ denotes the $1 - \sigma$ statistical error on dark energy parameters when nuisance parameters are included and not included respectively

survey	p	$\sigma(p)$	$\Delta_s(p)$	$\Delta_s(p)/\sigma(p)$	$\Delta_s(p)$	$\Delta_s(p)/\sigma(p)$	$\Delta_s(p)$	$\Delta_s(p)/\sigma(p)$
deg^2			$\beta = 1.4$	$\beta = 1.4$	$\beta = 1.7$	$\beta = 1.7$	$\beta = 2.0$	$\beta = 2.0$
	$\Omega_\Lambda\,[0.7]$	0.038	0.042	1.09	0.044	1.15	0.047	1.23
4000	$w_0\,[-1]$	0.41	0.65	1.6	0.8	1.97	1.0	2.4
	$w_a\,[0]$	0.71	2.64	3.7	3.1	4.4	3.6	5.2
	$\Omega_\Lambda\,[0.7]$	0.08	0.088	1.09	0.095	1.18	0.11	1.31
400	$w_0\,[-1]$	0.96	1.6	1.69	1.97	2.0	2.42	2.52
	$w_a\,[0]$	1.9	5.3	2.8	6.7	3.6	8.3	4.4

Table 4.4 Same as Table 4.3 but for $\langle v_i v_j \rangle$.

Survey	v_{ij}			$\langle v_i v_j \rangle$		
deg^2	$\beta = 1.4$	$\beta = 1.7$	$\beta = 2.0$	$\beta = 1.4$	$\beta = 1.7$	$\beta = 2.0$
4000	0.24 [0.25]	0.21 [0.23]	0.18 [0.22]	0.09 [0.2]	0.085 [0.16]	0.08 [0.13]
400	0.32 [0.42]	0.3 [0.4]	0.27 [0.39]	0.16 [0.38]	0.17 [0.33]	0.17 [0.29]

Table 4.5 Constraints on the parameters β_0 and γ used to model the systematic offset. Constraints are shown as $\Delta\beta_0\,[\Delta\gamma]$.

4.5   CHAPTER SUMMARY

We have shown in chapter 3 that galaxy cluster surveys compiled via the SZ Effect have the potential to place strong constraints on cosmology, and in particular the nature of dark energy. In this chapter, we study some of the obvious potential systematic errors associated with such surveys. Cluster radial peculiar velocities closely trace the large-scale radial peculiar velocity field independent of cluster mass; we demonstrate that two useful cluster radial peculiar velocity statistics are nearly independent of cluster mass, in marked contrast to cluster number count statistics. On the other hand, cluster radial peculiar velocity determinations from three-band observations of SZ distortions can require additional cluster data or assumptions, and are complicated by microwave emission from dusty galaxies and radio sources, which may be correlated with clusters. Systematic errors in radial peculiar velocity due to these factors can give substantial biases in determination of dark energy parameters, although large cluster radial peculiar velocity surveys will contain enough information that the errors can be modeled using the data itself, with little degradation in cosmological constraints.

5.0 EFFECTS OF QUASAR FEEDBACK IN GALAXY GROUPS.

Understanding properties of the Universe is a challenging task, and different observational techniques are being used as a cosmology probe. These probes provide complementary information about various cosmological parameters. Also, different probes have different systematic errors, and hence serve as an important consistency check. The galaxy clusters considered in this thesis are complex bound objects, subject to a variety of physical effects which are difficult to model. Here we study the effects of quasar feedback in galaxy groups to determine how much effect it will have on the baryon mass fraction of clusters. If the mass fraction is constant, then kinematic SZ measurements are directly proportional to the cluster total momentum, which is straightforward to extract from cosmological simulations. But the mass fraction can be substantially affected by feedback processes which can remove baryons from the galaxy cluster potential well. Then comparing the cluster baryon momentum distribution, measured via the kSZ effect, with the cluster total momentum distribution, determined via simulations or analytic models, becomes more challenging.

The majority of baryons in clusters and groups are in the form of hot intracluster gas rather than than individual galaxies. Properties of the Intracluster Medium (ICM) have been studied through a combination of X-ray and radio observations (Nulsen et al., 2005; Heinz et al., 2002; Fabian et al., 2000). Although the dark matter distribution in galaxy clusters follows a self-similar relation (Pointecouteau et al., 2005; Vikhlinin et al., 2006), the hot gas does not (Sanderson et al., 2003; Popesso et al., 2005). Additional non-gravitational sources of heating are required to explain the observations. One interesting and plausible possibility is the energy radiated from quasars or Active Galactic Nuclei (AGN) and deposited into the ICM (Kaiser, 1991; Valageas and Silk, 1999; Nath and Roychowdhury, 2002; Scannapieco et al., 2005; Thacker et al., 2006), which we study in this work.

The best arena in which to study the impact of various feedback mechanisms is galaxy groups. Massive clusters with deeper gravitational potential wells are likely to have their global thermodynamic and morphological properties less affected by feedback. In comparison, galaxy groups have shallower potential wells while still having enough gas to display the effect of feedback on the ICM. Galaxy groups have recently been observed in X-rays at redshifts as large as $z = 0.6$ (Willis et al., 2005). In the optical band, Tago et al. (2008) have compiled group catalogs from the SDSS Data Release 5 catalog. Evidence for heating by a central AGN or radio source in galaxy groups and clusters has been the subject of several recent papers (Croston et al., 2005; Jetha et al., 2006; Sanderson et al., 2005). These observations show excess entropy in cluster cores, which suggests that some heating process must act to offset cooling.

In recent years, cosmological simulations including dark matter and gas have been able to follow the evolution of individual galaxy groups and clusters. A number of studies have investigated the cluster baryon fraction and its evolution in numerical simulations. Adiabatic simulations that do not include radiative cooling find cluster baryon fractions around 0.85 of the universal baryon fraction (Evrard, 1990; Metzler and Evrard, 1994; Navarro et al., 1995; Lubin et al., 1996; Eke et al., 1998; Frenk et al., 1999; Mohr et al., 1999; Bialek et al., 2001). Preheating the gas reduces the fraction further (Bialek et al., 2001; Borgani et al., 2002; Muanwong et al., 2002; Kay et al., 2003). When cooling, star formation and other feedback processes are included, the baryon fraction is higher than that obtained from adiabatic simulations (Muanwong et al., 2002; Kay et al., 2003; Valdarnini, 2003; Ettori et al., 2004; Nagai et al., 2007). This leads to an "overcooling" problem and indicates an additional feedback mechanism.

In the current study, we analyze the effect of quasar feedback on the baryon distribution and thermodynamics of hot gas in galaxy groups. We also study its implication for the SZ angular power spectrum, which receives a dominant contribution from high-redshift halos. Komatsu and Seljak (2002) showed that the tSZ angular power spectrum provides a strong constraint on the normalization of the matter power spectrum, σ_8. Upcoming SZ surveys like ACT or SPT will have sufficient sensitivity to determine σ_8 with an accuracy limited by uncertainty in the theoretical model. Also, the kinematic SZ effect is a measure of bulk

motions in the universe and may be a competitive probe for studying cosmology (Sehgal et al., 2005; Bhattacharya and Kosowsky, 2007; Hernández-Monteagudo et al., 2006; DeDeo et al., 2005; Maturi et al., 2007; Roncarelli et al., 2007). But one of the major sources of uncertainty in modeling the kSZ effect is the gas fraction and its evolution. So understanding both the thermal and kinematic SZ signals requires detailed understanding of feedback mechanisms in galaxy clusters and groups. The mechanisms and effects of feedback are also a long-standing question in astrophysics, with particular bearing on the process of galaxy formation.

To this end, we have analyzed a sample of ten galaxy groups at $z = 1$ from numerical cosmological simulations of gas and dark matter which have been extended to include a self-consistent model for the evolution of massive black holes and their baryon feedback. At redshift $z > 1$, the quasar mode of black hole accretion is expected to be the dominant feedback mechanism, compared to the radio-loud accretion mode which becomes important at lower redshifts (Sijacki et al., 2007). The size of our simulations prevents studying feedback in galaxy clusters, but rather restricts us to less massive galaxy groups. But as already mentioned, galaxy groups with shallow potential wells provide the best place to study non-gravitational heating and its implications for the properties of hot gas. High-redshift galaxy groups are also a major contributor to the tSZ power spectrum, which peaks around $z \approx 1$, when galaxy groups are more numerous than massive clusters (Komatsu and Seljak, 2002).

Following this introduction, section 5.1 describes our simulation and its implementation of quasar feedback. In section 5.2 we study the effect of numerical resolution on our results; in section 5.3 we describe our results and compare them with a simulation that do not include quasar feedback.

5.1 SIMULATION

The cosmological simulations used in this study are described in detail in Di Matteo et al. (2008). They use an LCDM cosmological model with parameters consistent with the Wilkinson Microwave Anisotropy Probe first-year results (Spergel et al., 2003): $\Omega_0 = 0.3$, $\Omega_\Lambda = 0.7$, primordial power spectral index $n = 1$, Hubble parameter $h = 0.7$ with $H_0 = 100h$

Run	Box size	N_p	m_{DM}	m_{gas}	ϵ	z_{end}
	$h^{-1}\mathrm{Mpc}$		$h^{-1}M_\odot$	$h^{-1}M_\odot$	h^{-1} kpc	
D4	33.75	2×216^3	2.75×10^8	4.24×10^7	6.25	0.00
D6	33.75	2×486^3	2.75×10^7	4.24×10^6	2.73	1.00

Table 5.1 Numerical parameters of cosmological simulations (D4 & D6).

km/s/Mpc, and matter power spectrum normalization $\sigma_8 = 0.9$. A Gaussian random initial condition for this cosmology is evolved from high redshifts to the current epoch using a modified version of the parallel Tree Particle Mesh Smoothed Particle Hydrodynamics (TreePM-SPH) code GADGET2 (Springel, 2005), which manifestly conserve entropy and energy. Gas dynamics is implemented with the Lagrangian smoothed-particle hydrodynamics (SPH) technique (Monaghan, 1992). Radiative cooling and heating processes are computed with a spatially uniform photoionizing UV background (Katz et al., 1996). For modeling star formation and its associated supernova feedback the code uses a sub-resolution multiphase model for the interstellar medium developed by Springel and Hernquist (2003a). In this model, a thermal instability is assumed to operate above a critical density threshold ρ_{th}, producing a two phase medium consisting of cold clouds embedded in a tenuous gas at pressure equilibrium. Stars form from the cold clouds, and short-lived stars supply an energy of 10^{51} ergs to the surrounding gas as supernovae. This energy heats the diffuse phase of the ISM and evaporates cold clouds, thereby establishing a self-regulation cycle for star formation. The ρ_{th} is determined self-consistently in the model by requiring that the equation of state (EOS) is continuous at the onset of star formation. The cloud evaporation process and the cooling function of the gas then determine the temperatures and the mass fractions of the two hot and cold phases of the ISM, such that the EOS of the model can be directly computed as a function of density. The latter is encapsulating the self-regulated nature of star formation owing to supernovae feedback in a simple model for a multiphase ISM. As in Springel and Hernquist (2003a), we have included a model for supernova-driven galactic winds with an initial wind speed of $v \sim 480$km/s.

A unique aspect of the simulations is their inclusion of super-massive black holes and the resulting energy feedback from mass accretion (Di Matteo et al., 2008). Black holes are represented as collisionless "sink" particles which grows from a seed black hole through accretion of mass from its immediately surrounding gas or through merger with another black hole. Seed black holes of mass $M = 10^5 h^{-1} M_\odot$ are placed into the centers of halos whenever they reach a mass threshold of $10^{10} h^{-1} M_\odot$. The subsequent gas accretion rate onto the black hole is estimated using the Bondi-Hoyle-Lyttleton parametrization (Bondi, 1952; Bondi and Hoyle, 1944; Hoyle and Lyttleton, 1939). We assume a fixed value $\eta = 0.1$ for the radiative efficiency $\eta \equiv L_r/(\dot{M}_{BH} c^2)$, where L_r is the radiated luminosity and $\dot{M}_{\mathrm{BH}}$ is the mass accretion rate. This efficiency value is the mean value of a radiatively efficient accretion disk onto a Schwarzschild black hole (Shakura and Syunyaev, 1973). We further assume that a fraction ϵ_f of L_r couples to the surrounding gas in the form of feedback energy E_f deposited isotropically, i.e. $\dot{E}_f = \epsilon_f L_r$. A fixed value of $\epsilon_f = 0.05$ is adopted here to fit current data on the normalization of the $M_{\mathrm{BH}} - \sigma$ relation between black hole mass and stellar velocity dispersion (Di Matteo et al., 2005).

We use three different simulation runs, each of box size $33.75\,\mathrm{Mpc}/h$. The box size is a compromise between the requirements of sufficient spatial resolution to resolve physical processes in high-density regions surrounding black holes and sufficient volume to allow formation of halos with galaxy group masses. We study halos at $z = 1$: below this redshift, the fundamental modes in the cosmological box become nonlinear and the simulations become unreliable on scales of their largest objects (Di Matteo et al., 2003). We name the runs D4 (with and without black holes) and D6 (include black holes) following the naming scheme adopted in Springel and Hernquist (2003b). Runs D4 and D6 include black hole accretion along with cooling, star formation and supernova feedback, while the run-D4 (no black holes) leaves out black holes but includes all other physical processes. We use D4 (no black holes) as a baseline comparison simulation to analyze the effects of quasar feedback on galaxy groups for the run D4. We also compare D4 and D6 to understand the issues of resolution and convergence. The numerical parameters of the runs, including particle number and mass resolution, are listed in Table 5.1.

Table 5.2 lists the radius and mass of the galaxy groups formed in these simulations (the

Groups	R_{200m}	R_{500m}	M_{200m}	M_{500m}
	Mpc/h	Mpc/h	$10^{13} M_{\odot}/h$	$10^{13} M_{\odot}/h$
0	0.80	0.56	4.71	3.08
1	0.77	0.57	4.40	3.10
2	0.75	0.45	2.97	1.57
3	0.68	0.46	2.14	1.64
4	0.65	0.41	1.89	1.21
5	0.63	0.36	1.780	0.82
6	0.63	0.37	1.783	0.84
7	0.60	0.36	1.47	0.80
8	0.57	0.34	1.23	0.67
9	0.53	0.36	1.13	0.76

Table 5.2 Properties of galaxy groups in the simulations at $z = 1$

bulk group properties are essentially same for all the three simulations). Masses are defined as the amount of matter contained within a spherical region of overdensity 200 (M_{200m}) or 500 (M_{500m}) times the mean density of the universe at $z = 1$ (Di Matteo et al., 2003). Figure 5.1 shows gas density and star density for the most massive halo ($M_{200m} = 4.7 \times 10^{13} h^{-1} M_{\odot}$) in the simulation. The left panel shows the map for each of the properties when black hole feedback is included while the right panel gives the map with no quasar feedback. Note the gas density maps are color coded by temperature- the brightness shows the density and the color represents the temperature. It is evident that the gas is hotter when the feedback is included compared to when not included. Also the distribution of stars has changed significantly when quasar feedback is included.
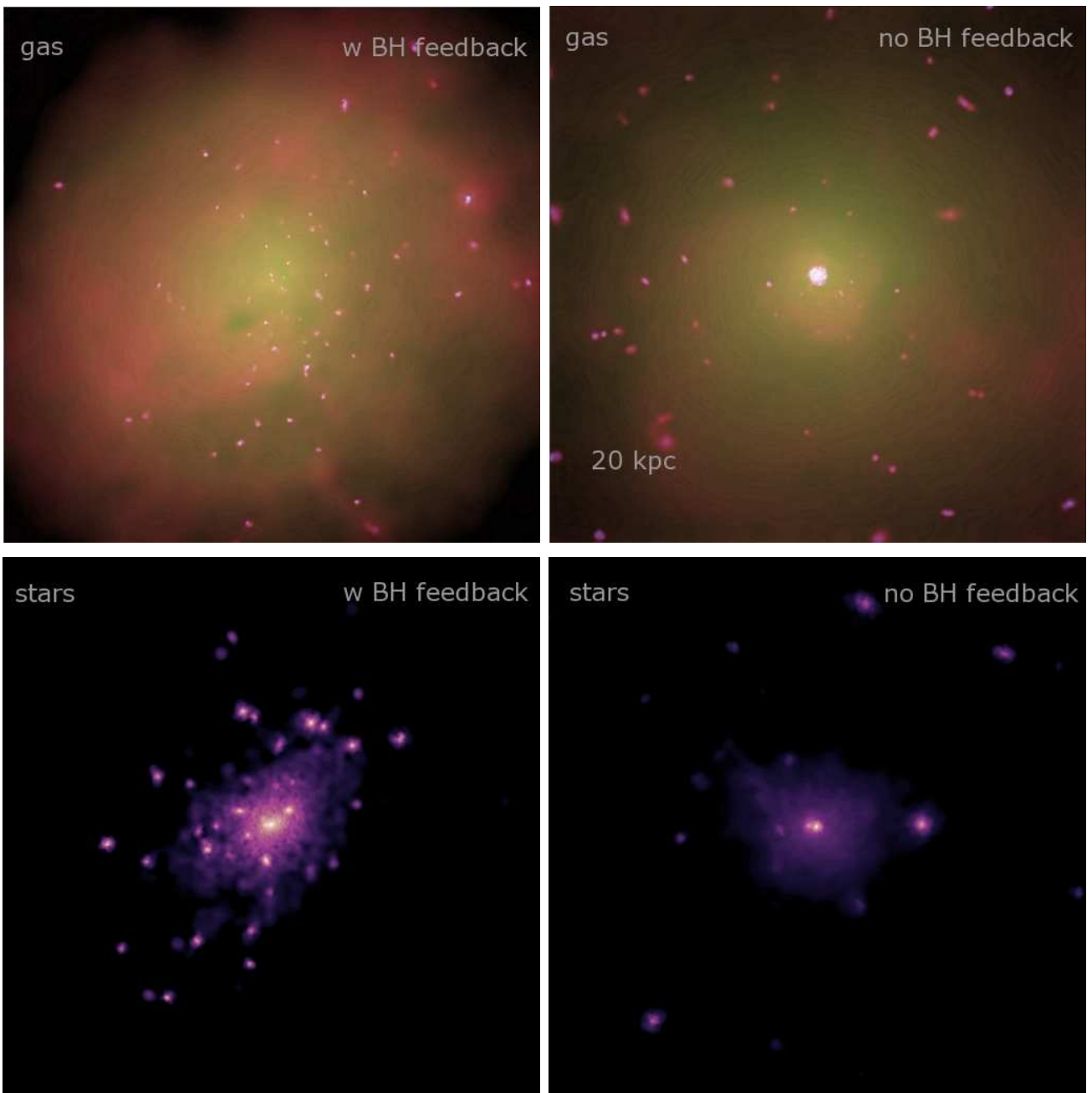
Figure 5.1 The gas distribution (top) and star distribution (bottom), both with quasar feedback (left column) and without (right column), for a halo of mass $M = 4.6 \times 10^{13} M_\odot$ at $z = 1$. The gas density maps are color coded by temperature (brightness shows density and color represents temperature). Note the qualitative difference in the distribution of stars between the two simulations.

5.2   EFFECTS OF NUMERICAL RESOLUTION

To study the effect of quasar feedback, we need to resolve quasars and surrounding gas at kiloparsec scales while simultaneously following the formation and evolution of galaxy groups at megaparsec scales. Given this huge dynamic range, it is worthwhile to check how numerical resolution affects our results. We have run two simulations, namely "D4" and "D6," with the same cosmological parameters, initial conditions and simulation volume. The lower-resolution D4 run uses 2×216^3 total particles, while D6 uses 2×486^3 particles. The corresponding mass resolution of the gas is $4.24 \times 10^7 M_\odot/h$ and $4.24 \times 10^6 M_\odot/h$. Their spatial resolution is characterized by gravitational softening lengths of $6.25 \, \text{kpc}/h$ and $2.73 \, \text{kpc}/h$ respectively.

We have studied the difference in the star and gas distributions at redshift $z = 1$, with comparisons displayed in Fig. 5.2. These plots show the average differential profile in the simulations.

On average, both star and gas distributions agree within 10% for the D4 and D6 runs for $R > 0.1 R_{200m}$. Beyond $R = R_{200m}$, statistical fluctuations causes star distributions to vary. Note that most of the star formation occurs in the inner region of the halo, so these statistical variations in the outer parts do not affect any of the conclusions about star fraction.

The temperature profile shows roughly $10 - 15\%$ difference between the simulations D4 and D6 in the inner region of the cluster, dropping to 5% for $R > 0.2 R_{200m}$. The pressure profile shows relatively more robustness to numerical resolution: a 10%-15% difference in the inner region drops to only 5% to 3% for $R > 0.2 R_{200m}$. Numerical resolution should thus have a minimal effect on the tSZ flux, since most of the signal comes from outside the core. Finally, the entropy profile shows a difference of 20% in the inner region and a 5% difference for $R > 0.3 R_{200m}$.

As already shown in Springel and Hernquist (2003b) and Hernquist and Springel (2003) using a large number of cosmological simulations, simulation including star formation and cooling converge reasonably well in the resolution range between D4 and D6.

Given this rough quantification of the effect of increased resolution, we proceed to analyze the lower-resolution D4 simulation in the rest of the chapter and compare with the same

resolution run without black holes, noting where errors due to numerical resolution limits might be a significant fraction of the effects being discussed. In the following sections, we study the differential and cumulative profile for each physical quantity with two lower resolution D4 runs both with and without including black holes. For each physical quantity we also calculate the difference in the profiles for each halo between the two runs with and without black holes and then show the mean of the difference. Also we find there are atleast 3 mergers namely 2nd, 5th and 8th most massive halos(in the group of 10 halos) we considered here. While studying the average profiles, we have excluded these halos from the averaging process so that the profiles do not get biased. However we have reported properties of all the halos when they are studied as a function of mass.

5.3 RESULTS

5.3.1 Thermodynamics of the Intracluster Medium

In this section we study the impact of quasar feedback on thermodynamics of the ICM, namely on the three quantities pressure, temperature and entropy. Figure 5.3 gives the average temperature profile with scatter around the mean. In the inner region ($R < 0.2R_{200m}$) of the halo, the temperature is enhanced by about 15-20% and by 5-10% in the region $0.2R_{200m} < R < 0.5R_{200m}$. This is physically reasonable as quasar feedback is coupling part of its radiated thermal energy to the surrounding ICM. We do not see any change in temperature due to quasar feedback at radii outside the halo core. For comparison we also show the average mean profile from the D6 run.

Note however, that the temperature profile inside the halo core becomes steeper when the feedback is included, whereas the observations at low redshift shows a rather flat profile inside the core. This disagreement might be either due to the inability of the feedback mechanism to explain the observed temperature profile and an improved model is needed or that one needs to include other sources of feedback in the simulations. Observations of group size halos at high redshift will be needed in order to understand whether the temperature
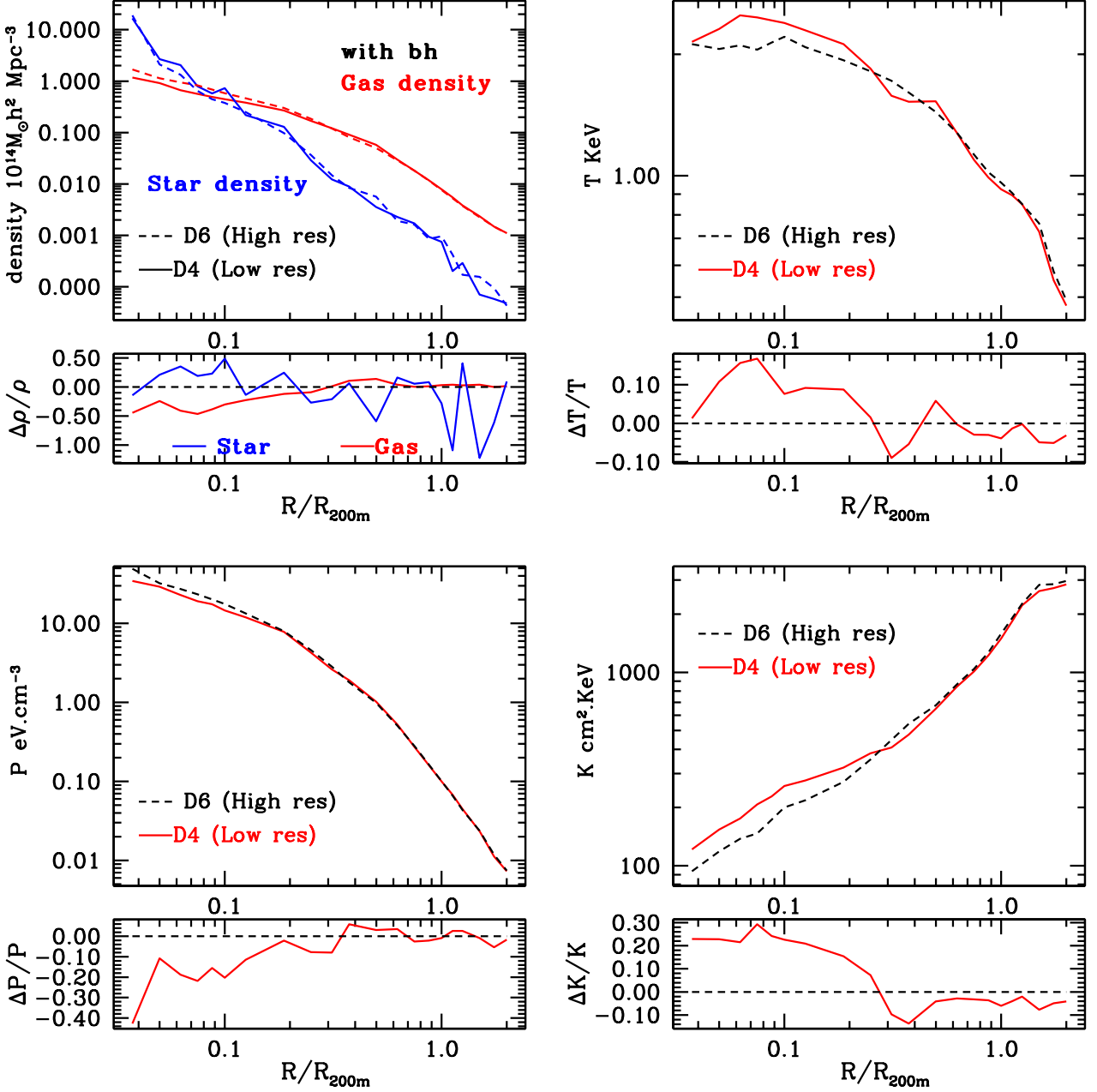
Figure 5.2 The effect of numerical resolution on various quantities as functions of radius: baryons, both gas and stars (top left), temperature (top right), pressure (bottom left) and entropy (bottom right). In each panel, dotted lines represents higher resolution (D6) and solid lines represent lower resolution(D4).

profile indeed gets steeper at higher redshift or a better feedback mechanism is required to explain the flatness of the temperature profile.

The temperature of the system agrees fairly well with previous studies made using halos of similar mass (Borgani et al., 2004; Khalatyan et al., 2008; Finoguenov et al., 2001). For example, a halo of mass $4.7 \times 10^{13} M_\odot h^{-1}$ is expected to have a temperature of around 1 keV at z=0. We find a temperature of 1.5 keV for a similar system at z=1. If a virial scaling relation is assumed this translates to a temperature of about 1 keV at z=0 which is consistent with previous studies.

The corresponding average pressure profile is shown in Fig. 5.4. We find that the pressure decreases for $R < 0.3\,\mathrm{Mpc}/h$, beyond which quasar feedback clearly leads to a pressure enhancement of 15% to 20% out to radius of R_{200m}. The entropy profile is shown in Fig. 5.5. The excess entropy near the core region is 50% larger than the no feedback case. The observational finding for the entropy profile for small groups (Ponman et al., 2003) agrees fairly well with the current study when virial scaling is assumed to translate the entropy profile at z=1 in the current study to z=0. The scatter around the mean profile for each of these quantities is large, so we need a larger sample size to confirm these systematic deviations. The entropy and pressure profile indicates that the quasar feedback has driven the gas out from the inner region and redistributed in the outer region. The lower panels of the figures show the fractional difference for each quantity. As shown, in the inner region the difference in the profiles is significant; far in excess of the numerical resolution error. Similar differences can be seen in the outside region where the numerical resolution error is few percent.

5.3.2   Baryon Fraction of the Intracluster Medium

A particularly important issue for interpreting future SZ measurements is the gas fraction in a given halo. Here we consider the effect of quasar feedback on both baryonic components, stars and hot gas. The ten most massive objects formed in the simulations have masses ranging from 1 to $5 \times 10^{13} M_\odot /h$. Each object is binned in spherical shells, and the mass fractions of stars, gas and dark matter within each shell are normalized to the primordial baryon fraction
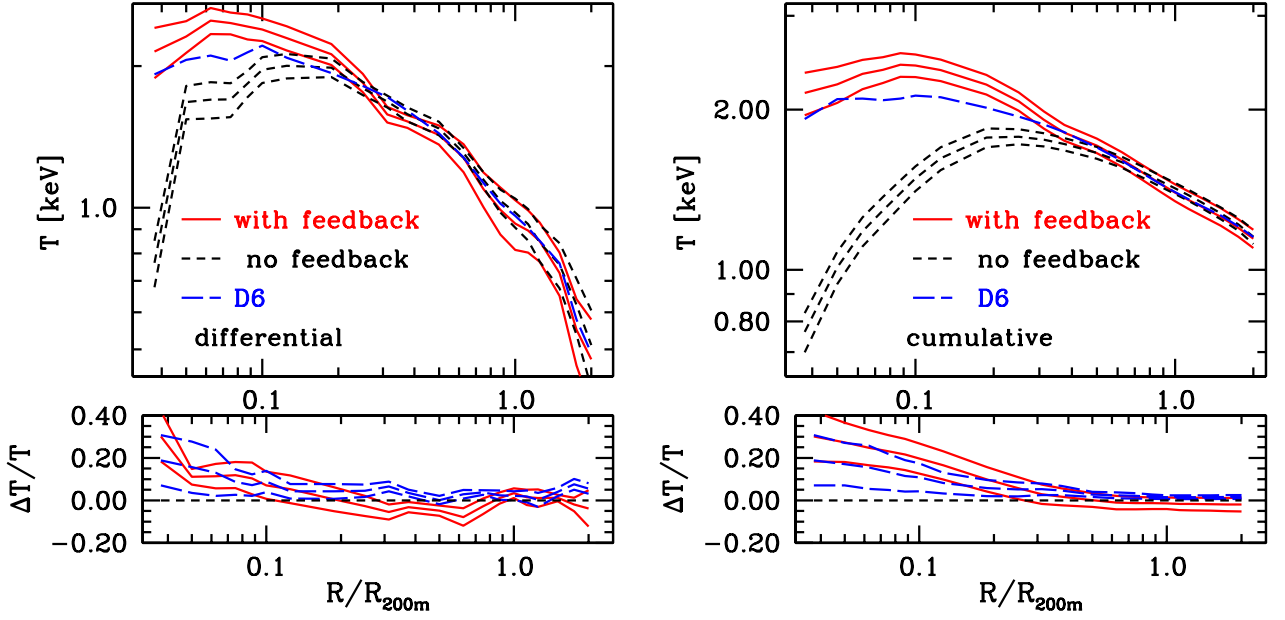
Figure 5.3 The mean differential (left) and cumulative (right) temperature profile of gas averaged over seven halos. For each top panel, solid lines represent the mean and scatter around the mean profile for simulation D4 including quasar feedback, while the dotted lines represents the same quantities for simulation D4 with no quasar feedback. Also shown is the mean profile from the D6 run (blue dashed line. The lower panels show the mean fractional change between the halos in the two runs. The blue dashed line shows the mean and the scatter in the difference in the profiles between D4 and D6 (resolution effect) while the solid red line shows similar difference between the D4 runs (the effect of including the black holes)
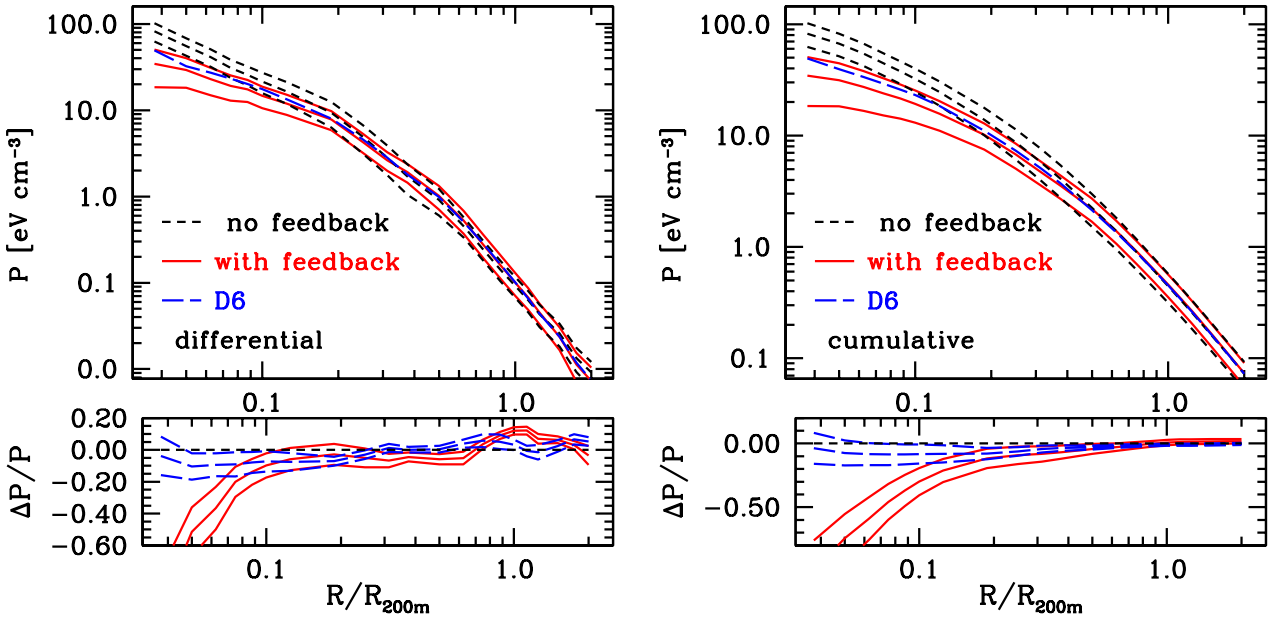
Figure 5.4 Same as in Fig. 5.3, except for pressure.
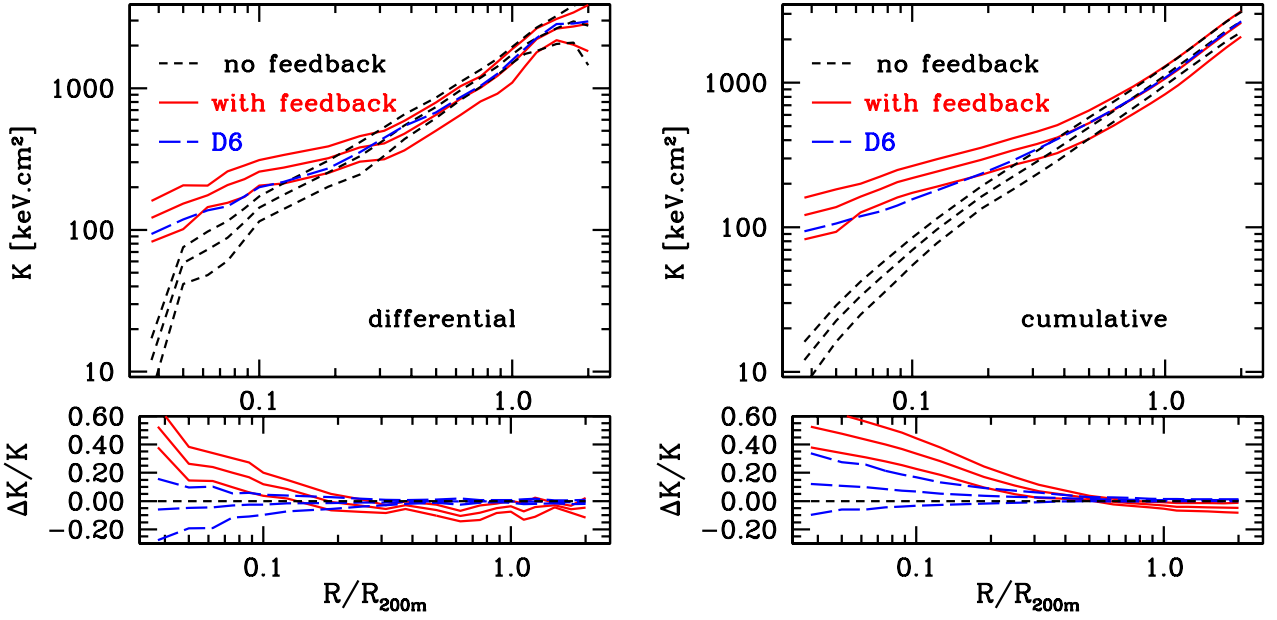
Figure 5.5 Same as in Fig. 5.3, except for entropy.

Ω_b/Ω_m. Figure 5.6 shows the average differential (left) and cumulative (right) distribution of gas and stars. Note the difference in star formation between the simulations with and without quasar feedback is on average 20% to 40% out to radius $R = 0.6R_{200m}$. It is evident that quasar feedback substantially suppresses star formation at all radii; the cumulative star distribution is 30% lower when feedback is included. The feedback mechanism provides enough pressure support that a significant amount of gas fails to collapse and form stars. Comparing differential and cumulative profiles, it is evident that most of the star formation is suppressed in the interior region of the halo.

Quasar feedback has an equally significant effect on the gas distribution. As shown in the top panel of Fig. 5.6, hot gas is being driven out from the internal region of the halo ($R < R_{500m}$) towards the outer region. The gas density is lowered by 20-30% in the core; to compensate for this depletion, gas density is 10% higher at $R > 0.3R_{200m}$ compared to the no-feedback case. As is evident from the cumulative gas distribution, the feedback is not powerful enough to drive the gas from gravitational well of the halo. Note that there is still a difference in total gas mass of around 4% within a radius of $2R_{200m}$ which compensates for the lower star formation in these halos.
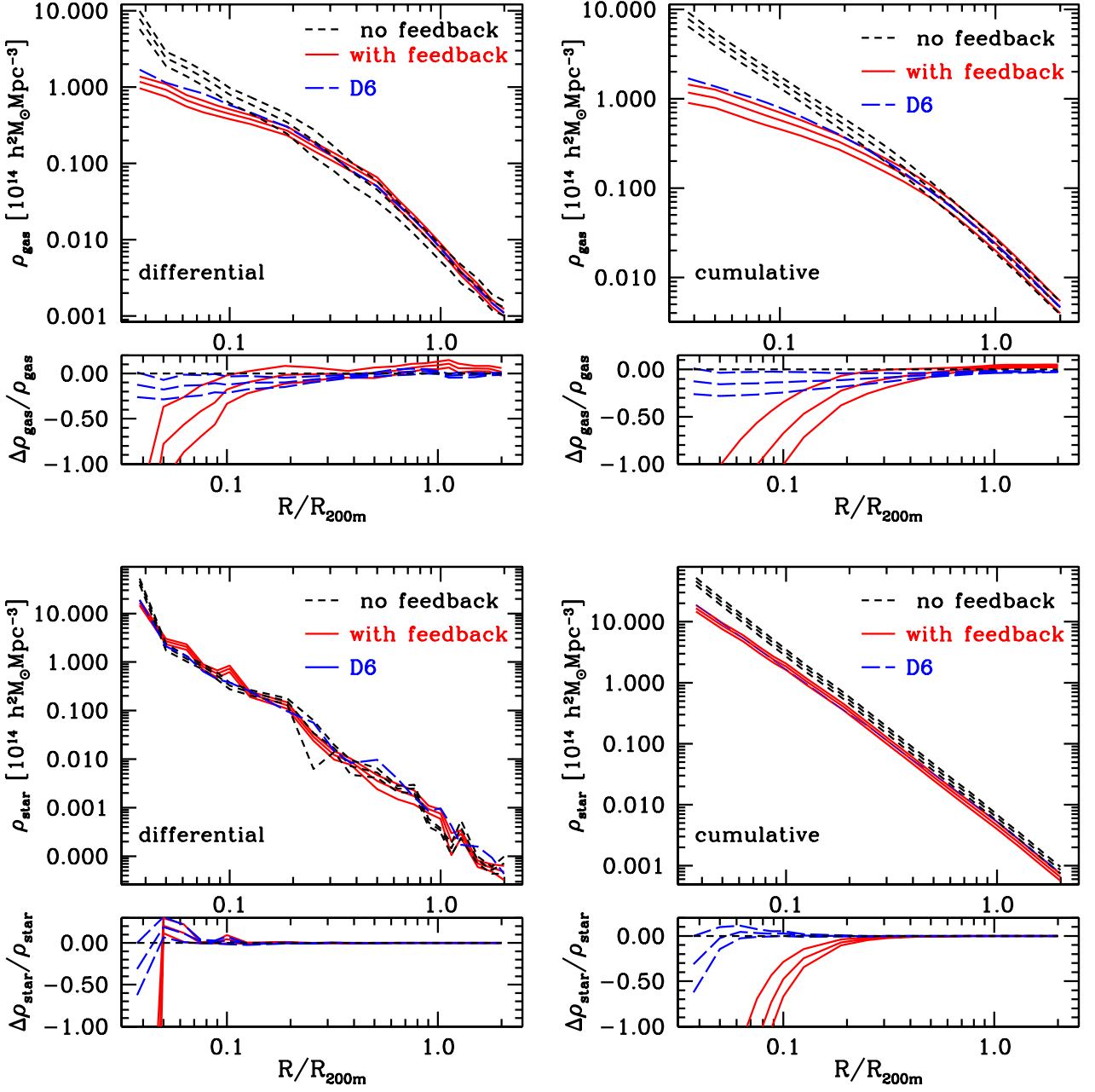
Figure 5.6 Same as in Fig. 5.3, except for gas density (top panels) and star density (lower panels).

71
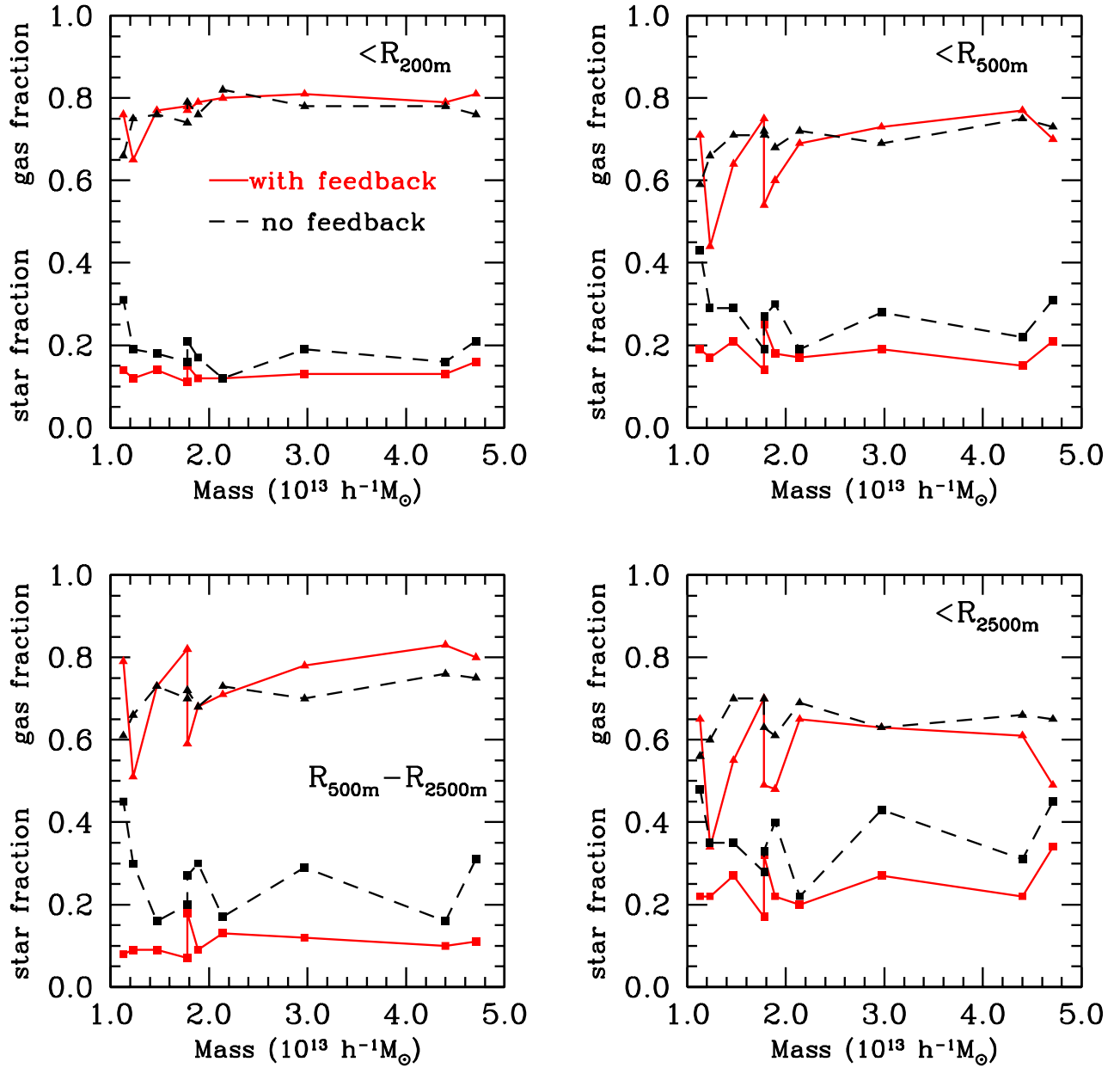
Figure 5.7 Cumulative gas and star fractions for the 10 most massive groups at $z = 1$ measured within a radius $R = R_{200m}$ (top left), $R = R_{500m}$ (top right), and $R = R_{2500m}$ (lower right), and between $R = R_{500m}$ and $R = R_{2500m}$ (lower left). For each panel, squares represents the star fraction and triangles the gas fraction. Solid lines correspond to the simulation including quasar feedback and dotted lines represent the no-feedback case.

Figure 5.7 shows cumulative gas and star fractions as a function of halo mass, measured out to radii R_{200m}, R_{500m}, and R_{2500m}, and also between R_{500m} and R_{2500m}. Table 3 to 6 gives the fractions for individual halos at these radii and also the mean and scatter. On average, cumulative star fractions shows a 30% depletion at all radii $< R_{500m}$ in simulation with quasar feedback; Gas fractions show only mild change at R_{200m} and R_{500m}, although at R_{2500m} the gas fraction is about 15% lower with quasar feedback. When halo cores are excluded (i.e. between R_{500m} and R_{2500m}), the gas fraction is enhanced by about 10% in simulation with feedback. This again shows that gas is driven off from the inner region of the halos to outer region. The gas fraction $< R_{500m}$ displays a slight trend with mass in both simulations, although the star fraction shows no such effect.

Figure 5.8 shows the cumulative ratio of gas to stars. This quantity plays an important role for determining the cosmic matter density (White et al., 1993; Evrard, 1997; Allen et al., 2002; Ettori et al., 2004; Allen et al., 2004). Usually it is assumed that this ratio is fixed at any radius with negligible redshift evolution (Ettori et al., 2006). We find that this assumption does not hold for either of the simulations. Without quasar feedback, the gas mass to stellar mass ratio changes roughly from 2 to 5, a factor of 2.5, between $0.3R_{200m}$ and R_{200m}; for the simulation including quasar feedback the corresponding change in the ratio is slightly larger, from 2 to 7.5, a factor of 3.5. The ratio rises more steeply for the simulation with feedback and continues increasing beyond R_{200m}.

5.3.3 Thermal Sunyaev-Zeldovich Decrements

The thermal Sunyaev-Zeldovich distortion from quasar feedback has been studied previously (see, e.g., Chatterjee and Kosowsky (2007), Scannapieco et al. (2008) and references therein). This effect has a systematic impact on galaxy-group-sized halos. As discussed above, the inaccuracy in the pressure profile due to numerical resolution limitations is on the order of 10% for $R < 0.1R_{200m}$, so we exclude the halo core region when calculating SZ distortions. This does not substantially affect any of our results since the major contribution to the SZ signal comes from the region outside the halo cores (Komatsu and Seljak, 2002). We calculate the mean Compton y-distortion, which we denote as Y, by integrating the gas

Mass	Quasar Feedback		No Quasar Feedback	
$10^{13}\ M_\odot h^{-1}$	f_{gas}	f_{star}	f_{gas}	f_{star}
4.71	0.81	0.16	0.76	0.21
4.40	0.79	0.13	0.78	0.16
2.97	0.81	0.13	0.78	0.19
2.14	0.80	0.12	0.82	0.12
1.89	0.79	0.12	0.76	0.17
1.78	0.77	0.15	0.79	0.21
1.78	0.78	0.11	0.74	0.16
1.47	0.77	0.14	0.76	0.18
1.23	0.65	0.12	0.75	0.19
1.13	0.76	0.14	0.66	0.31
Mean	0.77	0.13	0.76	0.19
Scatter	0.21	0.13	0.20	0.21

Table 5.3 Cumulative fractions of gas and stars out to R_{200m}, both with and without quasar feedback.

Mass	Quasar Feedback		No Quasar Feedback	
$10^{13}~M_\odot h^{-1}$	f_{gas}	f_{star}	f_{gas}	f_{star}
4.71	0.70	0.21	0.73	0.31
4.40	0.77	0.15	0.75	0.22
2.97	0.73	0.19	0.69	0.28
2.14	0.69	0.17	0.72	0.19
1.89	0.60	0.18	0.68	0.30
1.78	0.54	0.25	0.72	0.27
1.78	0.75	0.14	0.71	0.19
1.47	0.64	0.21	0.71	0.29
1.23	0.44	0.17	0.66	0.29
1.13	0.71	0.19	0.59	0.43
Mean	0.66	0.18	0.70	0.28
Scatter	0.31	0.18	0.20	0.25

Table 5.4 Same as in Table 5.3, for R_{500m}.

Mass	Quasar Feedback		No Quasar Feedback	
$10^{13}\ M_\odot h^{-1}$	f_{gas}	f_{star}	f_{gas}	f_{star}
4.71	0.49	0.34	0.65	0.45
4.40	0.61	0.22	0.66	0.31
2.97	0.63	0.27	0.63	0.43
2.14	0.65	0.20	0.69	0.22
1.89	0.48	0.22	0.61	0.40
1.78	0.49	0.32	0.63	0.33
1.78	0.70	0.17	0.70	0.28
1.47	0.55	0.27	0.70	0.35
1.23	0.34	0.22	0.60	0.35
1.13	0.65	0.22	0.56	0.48
Mean	0.56	0.24	0.64	0.36
Scatter	0.11	0.054	0.046	0.081

Table 5.5 Same as in Table 5.3, for R_{2500m}.

Mass	Quasar Feedback		No Quasar Feedback	
$10^{13} \ M_\odot h^{-1}$	f_{gas}	f_{star}	f_{gas}	f_{star}
4.71	0.80	0.11	0.75	0.31
4.40	0.83	0.10	0.76	0.16
2.97	0.78	0.12	0.70	0.29
2.14	0.71	0.13	0.73	0.17
1.89	0.68	0.09	0.68	0.30
1.78	0.59	0.18	0.72	0.27
1.78	0.82	0.07	0.70	0.20
1.47	0.73	0.09	0.73	0.16
1.23	0.51	0.09	0.66	0.30
1.13	0.79	0.08	0.61	0.45
Mean	0.72	0.11	0.70	0.26
Scatter	0.10	0.032	0.04	0.09

Table 5.6 Cumulative fractions of gas and stars between radii R_{500m} and R_{2500m}, both with and without quasar feedback.
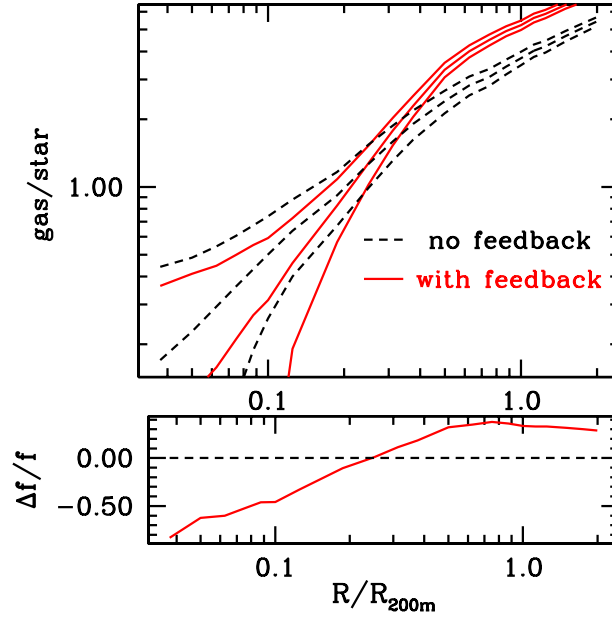
Figure 5.8 The average cumulative fraction of the ratio of gas mass and stellar mass for the ten halos. Solid lines represent the mean and scatter for the sample including quasar feedback, while dotted lines represent the same for the no-feedback case.

pressure along the line of sight for each halo out to a radius of R_{200m} and over the projected cross-section of the cluster in comoving coordinates. Figure 5.9 shows Y versus mass for the halos considered here, both with and without quasar feedback, with the lower panel showing the fractional change in Y. The individual halo Y-parameters are given in Table 5.7. On average, the Y parameter changes by 6% (excluding the mergers) due to quasar feedback in these galaxy groups. Note that the difference in the Y parameter between the run with the feedback and without the feedback are both positive and negetive as a function of mass.

We also give a power law fit to the Y-mass relation of the form

$$Y/E(z)^{2/3} = 10^\beta (M_{200m}/10^{14} M_\odot)^\alpha \tag{5.1}$$

(Sehgal et al., 2007), where α and β are fitting parameters and $E(z) = (\Omega_m(1+z)^3 + \Omega_\Lambda)^{0.5}$ is the redshift evolution of the Hubble parameter. Although the scatter is large, the power-law fits in both simulations given in Table 5.8 are close, and the values are consistent with other studies with larger numbers of halos (Sehgal et al., 2007).

As shown in Komatsu and Seljak (2002), the SZ power spectrum receives a dominant contribution from high redshift halos; especially for $l > 3000$, the contribution to C_l comes mostly from $z > 1$. The halo mass range considered here provides significant contribution to the C_l for $l > 5000$ and non-negligible contribution for $l = 3000$ to 5000. Since $C_l \propto Y^2$, we expect that quasar feedback will lead to a systematic increase in C_l on the order of 10% between $l = 5000$ and 10000.

Note that the difference in Y between the feedback and no-feedback cases does not tend to decrease with mass (Fig. 5.9), although the scatter is too large to claim any statistical significance for this behavior. It is imperative to simulate bigger volumes to quantify the effect of quasar feedback on the Y-mass relation for galaxy clusters, and the corresponding systematic differences in cluster mass estimates. We also emphasize that the effect of quasar feedback generally increases with redshift, so our results at $z = 1$ give conservative estimates for the quasar feedback impact on the SZ signal at earlier times.

M_{200m}	Y (feedback)	Y (no feedback)	$\Delta y/y$
$10^{13} M_{\odot}/h$	$10^{-7}\,\mathrm{Mpc}^2$	$10^{-7}\mathrm{Mpc}^2$	$\%$
4.71	1.91	1.88	0.02
4.40	1.43	2.06	-0.44
2.97	0.71	0.67	0.04
2.14	0.54	0.48	0.12
1.89	0.37	0.37	0.01
1.78	0.26	0.25	0.03
1.78	0.18	0.24	-0.33
1.47	0.21	0.24	-0.11
1.23	0.19	0.21	-0.08
1.13	0.18	0.16	0.11

Table 5.7 The relation between SZ Y-distortion and cluster mass for galaxy groups with and without quasar feedback.

	α	β
with feedback	1.78 ± 0.06	-5.55 ± 0.17
no feedback	1.79 ± 0.05	-5.47 ± 0.13

Table 5.8 Power law fits to the SZ Y-mass relation for galaxy groups with and without quasar feedback, as displayed in Fig. 5.9.
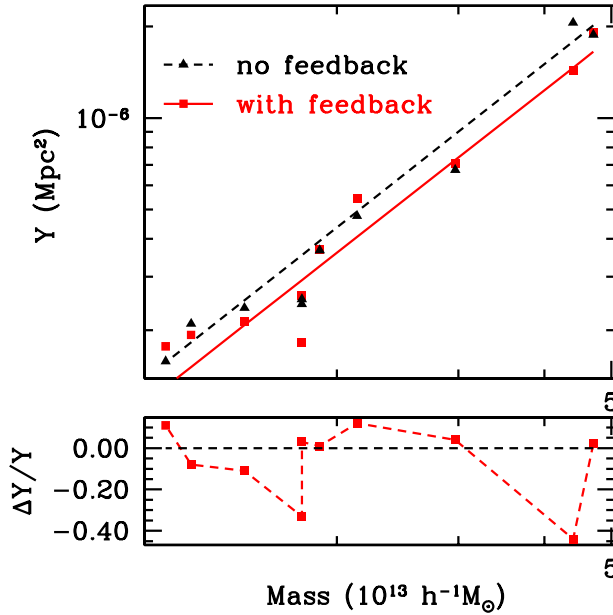
Figure 5.9 SZ Y-distortion versus halo mass for 10 halos, for mass and gas within R_{200m} of the halo center. Squares represent values from simulation D4 including quasar feedback; triangles represent values from simulation D4 without feedback. Lines are the best-fit power law to the Y-mass relation including quasar feedback (solid) and without quasar feedback (dotted). The lower panel shows the fractional change in Y between the two simulations.

5.4 CHAPTER SUMMARY

We study the effect of quasar feedback on distributions of baryons in galaxy groups using high-resolution numerical simulations. We use the entropy-conserving GADGET code that includes gas cooling and star formation, modified to include a physically-based model of quasar feedback. For a sample of ten galaxy-group-sized dark matter halos with masses in the range of 1 to $5 \times 10^{13} M_\odot/h$, star formation is suppressed by more than 50% in the inner regions due to the additional pressure support by quasar feedback, while gas is driven from the inner region towards the outer region of the halos. As a result, the average gas density is 50% lower in the inner region and 10% higher in the outer region in the simulation, compared to a similar simulation with no quasar feedback. Gas pressure is also higher in the outer region, while temperature and entropy are enhanced in the inner region. The total group gas fraction in the two simulations generally differs by less than 10%. We also find a small change of the total thermal Sunyaev-Zeldovich distortion, leading to 10% changes in

the microwave angular power spectrum at angular scales below two arcminutes.

6.0 DISCUSSION

Galaxy cluster radial peculiar velocities, measured directly via the kSZ effect, represent a new route to precision cosmological constraints. We have shown here that if cluster line-of-sight peculiar velocities can be measured with errors of few 100 km/sec, the resulting constraints on several cosmological parameters will be comparable with all current techniques. Such measurements could be important for their constraints on particular parameters, but are likely more valuable as consistency checks on the standard cosmological model. Multiple measurements of each cosmological parameter using independent methods provides our only way to determine whether our universe is actually described by the simple models spanned by the standard cosmological parameter space. The awkward appearance of dark energy on the cosmological stage makes these cross-checks all the more imperative.

Although the current uncertainty in radial peculiar velocity measurements is large with $\sigma_v \approx 1000$ km/s (Benson et al., 2003) for individual clusters, upcoming multi-band experiments like ACT (Kosowsky, 2003) or SPT (Ruhl et al., 2004) with arcminute resolution and few μK sensitivity have the potential to measure radial peculiar velocities with radial peculiar velocity errors of a few hundred km/s for large samples of clusters, opening a new window on the evolution of the universe. We have considered three separate cluster radial peculiar velocity statistics here, computing them using the halo model and comparing with numerical results. For surveys with thousands of cluster radial peculiar velocities with errors of a few hundred km/sec, dark energy constraints competitive with other major techniques (cluster number counts, baryon acoustic oscillations, supernova redshift-distance measurements, and weak lensing) can be obtained from the mean pairwise peculiar velocity v_{ij}, with different systematic errors. Even for radial peculiar velocity errors as large as 1000 km/s for individual clusters, a radial peculiar velocity catalog for several thousand clusters can

improve dark energy constraints from the corresponding cluster number counts by a factor of two.

A potentially even more important advantage to peculiar velocities is the control of systematic errors. It has been appreciated for some time that the comoving number density of clusters above a certain mass limit as a function of redshift depends sensitively on the underlying cosmology: a small increase in the cosmological growth factor leads to a large increase in the number of clusters. Blind SZ surveys will detect all clusters above a certain SZ-distortion threshold in a given direction of the sky, so their signal also depends sensitively on cosmological parameters. But the cluster SZ selection function is not equivalent to a simple mass cutoff, and a small systematic error in understanding this selection function can result in substantial systematic errors in cosmological constraints (Holder et al., 2001; Francis et al., 2005). In contrast, the radial peculiar velocity statistics considered here have little dependence on the cluster selection function, as we show explicitly that 20% variations in the mass selection function give only a few percent change in the radial peculiar velocity statistics.

The radial peculiar velocities inferred from kSZ measurements may also have systematic errors arising from a mis-estimated relation between the cluster X-ray temperature and its gas temperature, or from an incorrect correlation between the tSZ signal and the cluster gas temperature. Either might be used to extract the cluster radial peculiar velocity from three-band microwave measurements. Further complications arise from infrared point sources, which have variable spectral indices and can be substantially correlated with galaxy cluster positions. We have considered a simple toy model which assumes an arbitrary linear relationship between the measured and actual cluster radial peculiar velocity. If this relation is not well understood, we have quantified the bias it can induce in inferred values of cosmological parameters. This bias can be significant compared to the corresponding statistical errors, although reasonable levels of understanding of these correlations will likely reduce the systematic errors to below the level of statistical errors. Self-calibration of the radial peculiar velocity bias using the radial peculiar velocity data itself is another possible route to minimizing the impact of these systematic errors, if their effects can be accurately modeled with a particular assumed function of the cluster radial peculiar velocities.

As a part of understanding the systematic errors associated with the SZ effect, we have also studied the effect of quasar feedback on baryon fractions and on thermodynamics of intracluster medium of intermediate mass halos corresponding to galaxy groups. Quasar feedback redistributes hot gas, driving it from the inner region towards the outer part of the halos. As a result, gas density is 20% less in the inner part and 10% to 15% greater in the outer region when compared to the simulation without feedback. However, the gas fraction in the two simulation differs by only 5% to 10%, and gas fractions tends to increase mildly with increasing halo mass. Pressure decreases by 30% in the inner region and increases by 15% to 20% at radii larger than 0.4 R_{200m} due to the increased gas density in this region. This leads to a change of about 6% in the mean SZ Y-distortion. The resulting SZ angular power spectrum will be larger by around 10% for $l > 5000$. We find little dependence of the SZ enhancement with halo mass.

A number of further lines of work related to cluster radial peculiar velocities are worth pursuing. Here we have considered three different galaxy cluster radial peculiar velocity statistics: the radial peculiar velocity probability distribution function n_v, the mean pairwise peculiar velocity v_{ij}, and the radial peculiar velocity correlation function $\langle v_i v_j \rangle$. Each constrains well a different set of cosmological quantities. We have not attempted a joint analysis, finding the combined cosmological constraints from all three statistics: the correlations between the statistics are complicated, and no clear way to derive them analytically presents itself. Proper joint constraints will require numerical evaluation of the correlations between statistics from sets of large cosmological simulations, which is feasible but demanding. A related question is the extent to which these three statistics, which are convenient from a theoretical and observational point of view, exhaust the useful cosmological information on dark energy constraints: are there other radial peculiar velocity statistics which, when combined with these three using the correct correlations, would further tighten the constraints? This is an open, and challenging, question.

On the numerical front, we have performed limited tests comparing the VIRGO simulation results with the halo-model expressions for the radial peculiar velocity statistics here, finding reasonable agreement for the particular cosmological model the simulation is based on. This is encouraging, but it would be reassuring to have explicit comparisons between

theory and simulation for a wider range of models. Such computations require cosmological simulations over very large volumes, to capture a sufficient number of clusters with large enough masses, but can be done with fairly low mass resolution, since we only care about bulk cluster properties and not internal cluster details. Sets of such simulations are currently in progress.

The kSZ signal does not directly measure cluster radial peculiar velocity, but rather is proportional to a line-of-sight integral of the cluster gas' local radial peculiar velocity times its local density. Thus the kSZ effect is actually proportional to the cluster gas momentum with respect to the cosmic rest frame. We can sidestep the entire difficult observational issue of inferring cluster radial peculiar velocities from kSZ measurements by using cluster momenta instead. We then need theoretical calculations for the cluster momentum statistics corresponding to the radial peculiar velocity statistics considered here. Momentum statistics have the possibility of being just as cosmologically constraining, but easier to compare with observations. We have not found any suitable analytic approximations to the cluster momentum statistics, but this could also be evaluated numerically using large-volume, low-resolution N-body simulations mentioned above. The other related issue is connecting the cluster mass, which is used to evaluate cluster momenta in an N-body simulation, to the cluster gas mass, which gives the SZ signal. We need to understand the extent to which the cluster gas fraction is constant, or the extent to which we can understand its statistical distribution. We have already made initial steps to investigate this issue, finding, among other things, that the gas fraction in galaxy groups is affected non-negligibly by quasar feedback, which heats the gas and suppresses star formation. However, at mass scales substantially below galaxy clusters, the gas fraction appears to be reasonably independent of mass. Probing this relation for clusters is a challenging computational issue, requiring sophisticated hydro-dynamical simulations in much larger volumes to obtain information about galaxy clusters large enough to be of SZ interest.

As with so many cosmological sources of information, the advent of the dark energy era has given a new urgency to precision measurements. Galaxy cluster radial peculiar velocities, obtained via their kinematic Sunyaev-Zeldovich signal, directly probe the growth of structure in the universe via gravitational instability. The signals are small, but the

advantages manifest. We firmly advocate that cluster radial peculiar velocities should be added to the arsenal of tactics now trained on the dark energy issue.

APPENDIX A

ERRORS FOR THE PROBABILITY DENSITY FUNCTION

A.1   POISSON ERROR

Let N_z be the number of halos in redshift bin $z + \delta z$, and N_v be the number of halos in both the redshift bin $z + \delta z$ and the radial peculiar velocity bin $v + \delta v$. In a given radial peculiar velocity bin, the fractional density The observable in the normalized histogram of cluster radial peculiar velocities in a given redshift bin is then $n_v = N_v/N_z$. Thus n_v suffers from uncertainties in both numerator and denominator. We write the uncertainty in n_v as

$$\frac{\delta n_v^2}{n_v^2} = \frac{\delta N_v^2}{N_v^2} + \frac{\delta N_z^2}{N_z^2}$$

Assuming Poisson errors, $\delta N_v = \sqrt{N_v}$ and $\delta N_z = \sqrt{N_z}$ and using $N_v = n_v N_z$. We write

$$
\begin{aligned}
\delta n_v^2/n_v^2 &= \frac{1 + n_v}{n_v N_z} \\
\delta n_v &= \frac{\sqrt{1 + n_v}}{\sqrt{N_z n_v}} n_v \\
&= \sqrt{n_v}/\sqrt{N_z}(1 + 1/2n_v)
\end{aligned}
\tag{A.1}
$$

The last line follows from the expansion: $\sqrt{1 + n_v} = 1 + 1/2n_v + ... \approx 1 + 1/2n_v$ for $n_v << 1$.

A.2 COSMIC VARIANCE ERROR

Write the cosmic covariance between two different bins $[v_i, z_i]$ and $[v_j, z_j]$ as $C^{n_v}_{ij}$; here v_i denotes a particular radial peculiar velocity bin at an epoch of redshift z_i. $C^{n_v}_{ij}$ is defined as

$$C^{n_v}(ij) = \langle (\hat{n}_{vi} - n_{vi})(\hat{n}_{vj} - n_{vj}) \rangle \tag{A.2}$$

where $\hat{n}_v$ denotes the estimated PDF and $n_{vi} = n_v(v_i, z_i)$ etc. Using $n(m, \delta, \mathbf{x}) = (1 + b(m)\delta(\mathbf{x}))\bar{n}(m)$ and $\hat{n}_v = V(r)^{-1}[\int d^3\mathbf{x} \int dm\, mn(m|\bar{\delta}, \mathbf{x})p(v\,|\,m, \delta)]/ \int dm\, mn(m|\delta)$,

$$C^{n_v}(ij) = b(m_i, z_i)b(m_j, z_j)f_i f_j \langle \delta(\mathbf{x}_i, z_i)\delta^*(\mathbf{x}_j, z_j) \rangle \tag{A.3}$$

where $\langle ... \rangle$ denotes the ensemble average over the survey volume V_Ω and can be written as

$$\langle \delta_i \delta_j \rangle = \frac{1}{V_\Omega} \int_{V_\Omega} d^3\mathbf{r} \int\int d^3\mathbf{x} d^3\mathbf{x}' W(x)W(x')\delta(\mathbf{x}, a)\delta(\mathbf{x}', a')\delta_D^3(\mathbf{x} - \mathbf{x}' - \mathbf{r}) \tag{A.4}$$

where

$$\delta(\mathbf{x}, a) \equiv D_a \delta(\mathbf{x}) = D_a \int d^3\mathbf{k}\, \delta(\mathbf{k})e^{i\mathbf{k}\cdot\mathbf{x}}, \tag{A.5}$$

$W(x)$ is the tophat window function defined after Eq. (2.1) and $\delta(\mathbf{x})$ is the field describing linear comoving density perturbations evolved to the present; the three-dimensional Dirac delta distribution is written as $\delta_D^3(\mathbf{x})$. We can then write

$$
\begin{aligned}
\langle \delta_i \delta_j \rangle &= \frac{D_{a_i} D_{a_j}}{V_\Omega} \int_{V_\Omega} d^3\mathbf{r} \int\int d^3\mathbf{x} d^3\mathbf{x}' W(x)W(x')\delta(\mathbf{x})\delta(\mathbf{x}')\delta_D^3(\mathbf{x} - \mathbf{x}' - \mathbf{r}) \\
&= \frac{D_{a_i} D_{a_j}}{V_\Omega} \int d^3\mathbf{r} \int\int d^3\mathbf{k} d^3\mathbf{k}' \delta(\mathbf{k})\delta^*(\mathbf{k}')e^{-i\mathbf{k}\cdot\mathbf{r}}h(\mathbf{k} - \mathbf{k}', \mathbf{r}).
\end{aligned} \tag{A.6}
$$

where we write conventionally (Eisenstein and Zaldarriaga, 2001)

$$h(\mathbf{k}, \mathbf{r}) \equiv \frac{1}{V(r)} \int d^3\mathbf{x} W(x)W(|\mathbf{x} + \mathbf{r}|)e^{i\mathbf{k}\cdot\mathbf{x}}. \tag{A.7}$$

In the limit of a survey region large compared to the scale r, $h(\mathbf{k}, \mathbf{r}) \sim \delta_D^3(\mathbf{k})$, $r \ll R_\Omega$ (Takada and Bridle, 2007; Eisenstein and Zaldarriaga, 2001) with the convenient notation $V_\Omega = 4\pi R_\Omega^3/3$ for a spherical survey volume, giving

$$\int d^3\mathbf{x} W(x)W(|\mathbf{x} + \mathbf{r}|)e^{i(\mathbf{k} - \mathbf{k}')\cdot\mathbf{x}} \int d^3\mathbf{x} W^2(x) \propto \delta_D^3(\mathbf{k} - \mathbf{k}'). \tag{A.8}$$

Then

$$\langle \delta_i \delta_j \rangle = \frac{4\pi R_\Omega^2 D_{ai} D_{aj}}{V_\Omega} \int dk k^2 P(k) j_1(kR_\Omega), \tag{A.9}$$

so $C^{n_v}(ij)$ can be written as

$$C^{n_v}(ij) = \frac{3 D_{a_i} D_{a_j}}{R_\Omega} n_i n_j \int dk k^2 P(k) j_1(kR_\Omega) \tag{A.10}$$

where

$$n_v(v, z) = \frac{\int dm m b(m, a) \bar{n}(m) p(v|m, \delta, a)}{\int dm m \bar{n}(m)} \tag{A.11}$$

which is equivalent to Eq. (3.1). The expression $p(v|m, \delta)$ is defined in Eq. (2.6).

APPENDIX B

ERRORS FOR THE MEAN PAIRWISE PECULIAR VELOCITY

B.1   POISSON ERROR AND MEASUREMENT ERROR

We begin with Eq. (2.15) for the estimator of the mean pairwise peculiar velocity. Assume a particular radial peculiar velocity is measured with an accuracy δv. So the error δv_{ij} in v_{ij} can be written as

$$\frac{\delta v_{ij}}{v_{ij}} = \frac{\delta \Sigma_{ij}[v_i - v_j]}{\Sigma_{ij}[v_i - v_j]} + \frac{\delta n_p}{n_p}, \tag{B.1}$$

so that

$$\delta v_{ij} = \frac{\sqrt{2}\,[\Sigma_i \delta v_i^2]^{1/2}}{n_p} + \frac{v_{ij}}{\sqrt{n_p}} = \frac{1}{\sqrt{n_p}}\left(\sqrt{2}\sigma_v + v_{ij}\right) \tag{B.2}$$

where we have used $\delta n_p = \sqrt{n_p}$ assuming a Poisson distribution, and

$$\delta \Sigma_{ij}\,[v_i - v_j] = \sqrt{2}[\delta v_1^2 + \delta v_2^2 + ... + \delta v_{n_p}^2]^{1/2} = \sqrt{2}\sqrt{n_p}\sigma_v. \tag{B.3}$$

Here the individual radial peculiar velocity errors are added in quadrature and the last line follows from the central limit theorem.

B.2 COSMIC VARIANCE ERROR

The cosmic covariance for mean pairwise peculiar velocity between two separation and redshift bins $[r_p, z_p]$ and $[r_q, z_q]$ can be written as

$$C^{v_{ij}}(pq) \quad = \quad \langle (v_{ij}(p) - \hat{v}_{ij}(p))(v_{ij}(q) - \hat{v}_{ij}(q)) \rangle = \langle \hat{v}_{ij}(p)\hat{v}_{ij}(q) \rangle - v_{ij}(p)v_{ij}(q) \quad \text{(B.4)}$$

where $\hat{v}_{ij}$ is the estimated mean pairwise peculiar velocity from the survey volume and v_{ij} is its cosmic mean value, $\langle \hat{v}_{ij} \rangle = v_{ij}$. In what follows, the superscript "DM" is dropped for brevity. Using the expression for mean pairwise peculiar velocity given in Eq. (2.11), the above expression can be written as

$$C^{v_{ij}}(pq) \quad = \quad \frac{1}{1 + b_{\text{halo}}(a_p)^2 \xi(r_p, a_p)} \left[\frac{2}{3} r_p H(a_p) a_p b_{\text{halo}}(a_p) \left(\frac{d \ln D_a}{d \ln a} \right)_{a_p} \right] \frac{1}{1 + b_{\text{halo}}(a_p)^2 \xi(r_q, a_q)}$$

$$\times \quad \left[\frac{2}{3} r_q H(a_q) a_q b_{\text{halo}}(a_p) \left(\frac{d \ln D_a}{d \ln a} \right)_{a_q} \right] \left[\left\langle \hat{\bar{\xi}}(r_p) \hat{\bar{\xi}}(r_q) \right\rangle - \bar{\xi}(r_p) \bar{\xi}(r_q) \right], \quad \text{(B.5)}$$

where $\hat{\bar{\xi}}$) is an estimator for the volume-averaged dark matter correlation function

$$\bar{\xi}(r) \equiv \frac{1}{V(r)} \int_0^r dr' \, r'^2 \xi(r'). \quad \text{(B.6)}$$

An estimator $\hat{\xi}(r)$ for the two-point correlation function $\xi(r)$ is

$$\hat{\xi} = \frac{1}{V(r)} \int d^3\mathbf{x}' W(x') \int d^3\mathbf{x} W(x) \delta(\mathbf{x}) \delta(\mathbf{x}') \delta_D^3(\mathbf{x} - \mathbf{x}' - \mathbf{r}), \quad \text{(B.7)}$$

so an estimator for the volume-averaged correlation function can be written as

$$\hat{\bar{\xi}}(r) = \frac{1}{V(r)} \int_{V(r)} d^3\mathbf{r}' \frac{1}{V(r')} \int d^3\mathbf{x} W(x) \int d^3\mathbf{x}' W(x') \delta(\mathbf{x}) \delta(\mathbf{x}') \delta_D^3(\mathbf{x} - \mathbf{x}' - \mathbf{r}') \quad \text{(B.8)}$$

where the survey volume is given by $V(r) \equiv \int d^3\mathbf{x} \, W(x) W(|\mathbf{x} + \mathbf{r}|)$ for a normalized window function $\int d^3\mathbf{x} \, W(x) = 1$. Fourier transforming $\delta(x)$, we can write

$$\hat{\bar{\xi}}(r) \quad = \quad \frac{1}{V(r)} \int_{V(r)} d^3\mathbf{r}' \frac{1}{V(r')} \int d^3\mathbf{r}' \int d^3\mathbf{x} W(x) \int d^3\mathbf{x}' W(x') \delta_D^3(\mathbf{x} - \mathbf{x}' - \mathbf{r}')$$

$$\times \quad \int \int d^3\mathbf{k} d^3\mathbf{k}' \delta(\mathbf{k}) \delta^*(\mathbf{k}') e^{i(\mathbf{k}\cdot\mathbf{x} - \mathbf{k}'\cdot\mathbf{x}')}$$

$$= \quad \frac{1}{V(r)} \int_0^r d^3\mathbf{r}' \int \int d^3\mathbf{k} d^3\mathbf{k}' \delta(\mathbf{k}) \delta^*(\mathbf{k}') e^{-i\mathbf{k}\cdot\mathbf{r}'} h(\mathbf{k} - \mathbf{k}', \mathbf{r}') \quad \text{(B.9)}$$

Using $\langle \hat{\bar{\xi}}(r) \rangle = \bar{\xi}(r)$, we can then write

$$
\begin{aligned}
C^{\bar{\xi}}(pq) &= \left[\left\langle \hat{\bar{\xi}}(r_p)\hat{\bar{\xi}}(r_q) \right\rangle - \bar{\xi}(r_p)\bar{\xi}(r_q) \right] \\
&= \frac{1}{V(r_p)V(r_q)} \int_0^{r_p} d^3\mathbf{r}\, e^{-i\mathbf{k}\cdot\mathbf{r}} h(\mathbf{k}-\mathbf{k}',\mathbf{r}) \int_0^{r_q} d^3\mathbf{r}'\, e^{-i\mathbf{k}\cdot\mathbf{r}'} h^*(\mathbf{k}-\mathbf{k}',\mathbf{r}') \\
&\times \int d^3\mathbf{k} \int d^3\mathbf{k}' \int d^3\mathbf{k_1} \int d^3\mathbf{k_1'}[...]
\end{aligned}
\tag{B.10}
$$

The term in brackets can be written as

$$
\begin{aligned}
[...] &= \left[\langle \delta(\mathbf{k})\delta^*(\mathbf{k}')\delta(\mathbf{k_1})\delta^*(\mathbf{k_1'}) \rangle - \langle \delta(\mathbf{k})\delta^*(\mathbf{k}') \rangle \langle \delta(\mathbf{k_1})\delta^*(\mathbf{k_1'}) \rangle \right] \\
&\times \delta_D^3(\mathbf{k}+\mathbf{k_1})P(k)\delta_D^3(\mathbf{k}'+\mathbf{k_1'})P(k') + \delta_D^3(\mathbf{k}-\mathbf{k_1'})P(k)\delta_D^3(\mathbf{k}'-\mathbf{k_1})P(k').
\end{aligned}
\tag{B.11}
$$

Substituting this expression into Eq. (B.10) gives

$$
\begin{aligned}
C^{\bar{\xi}}(pq) &= \frac{1}{V(r_p)V(r_q)} \int d^3\mathbf{k} \int d^3\mathbf{k}' P(k)P(k') \left(e^{i\mathbf{k}\cdot(\mathbf{r}-\mathbf{r}')} + e^{-i\mathbf{k}\cdot\mathbf{r}-i\mathbf{k}'\cdot\mathbf{r}'} \right) \\
&\times \int_0^{r_p} d^3\mathbf{r}\, h(\mathbf{k}-\mathbf{k}',\mathbf{r}) \int_0^{r_q} d^3\mathbf{r}'\, h^*(\mathbf{k}-\mathbf{k}',\mathbf{r}')
\end{aligned}
\tag{B.12}
$$

As in the previous appendix, for large surveys such that $r << R_\Omega = (3V_\Omega/4\pi)^{1/3}$, $h(\mathbf{k}-\mathbf{k}',\mathbf{r}) \sim \delta_D^3(\mathbf{k}-\mathbf{k}')$ and (Takada and Bridle, 2007; Eisenstein and Zaldarriaga, 2001)

$$
hh^* = \frac{\int d^3\mathbf{x}\, W^2(x)W(|\mathbf{x}+\mathbf{r}|)W(|\mathbf{x}+\mathbf{r}'|)}{V(r_p)V(r_q)} \sim \frac{1}{V_\Omega}.
\tag{B.13}
$$

So Eq. (B.12) can be written as

$$
\begin{aligned}
C^{\bar{\xi}}(pq) &= \frac{1}{V_\Omega V(r_p)V(r_q)} \int d^3\mathbf{k}\, |P(k)|^2 \int_0^{r_p} \int_0^{r_q} d^3\mathbf{r}\, d^3\mathbf{r}' \left(e^{i\mathbf{k}\cdot(\mathbf{r}-\mathbf{r}')} + e^{-i\mathbf{k}\cdot(\mathbf{r}+\mathbf{r}')} \right) \\
&= \frac{8\pi}{V_\Omega r_p r_q} \int dk\, k^2 |P(k)|^2 j_1(kr_p) j_1(kr_q)
\end{aligned}
\tag{B.14}
$$

Substituting the above result in Eq (B.5), we obtain the final expression for cosmic covariance as

$$
\begin{aligned}
C^{v_{ij}}(pq) &= \frac{32\pi}{9V_\Omega} \frac{H(a_p)a_p b_{\text{halo}}(a_p)}{1+b_{\text{halo}}(a_p)^2 \xi^{\text{DM}}(r_p,a_p)} \frac{H(a_q)a_q b_{\text{halo}}(a_q)}{1+b_{\text{halo}}(a_q)^2 \xi^{\text{DM}}(r_q,a_q)} \left(\frac{d\ln D_a}{d\ln a} \right)_{a_p} \left(\frac{d\ln D_a}{d\ln a} \right)_{a_q} \\
&\quad \int dk\, k^2 |P(k)|^2 j_1(kr_p) j_1(kr_q).
\end{aligned}
\tag{B.15}
$$

On scales of interest, $\xi^{\text{DM}} \ll 1$, so Eq. (B.15) reduces to Eq. (3.6).

APPENDIX C

ERRORS FOR THE RADIAL PECULIAR VELOCITY CORRELATION FUNCTION

C.1 POISSON ERROR AND MEASUREMENT ERROR

The expression for the perpendicular radial peculiar velocity correlation $\langle v_i v_j \rangle_{\perp}(r)$ for a particular separation r can be written as

$$\langle v_i v_j \rangle(r) = \frac{\Sigma_{ij}[v_i v_j]_{\perp}}{n_p} \tag{C.1}$$

where we abbreviate $[v_i v_j]_{\perp} \equiv ([\mathbf{r_i} - \mathbf{r_j}] \times \mathbf{v}_i) \cdot ([\mathbf{r_i} - \mathbf{r_j}] \times \mathbf{v}_j)$ the product of the radial peculiar velocity components perpendicular to the direction connecting the two positions. As before, $\mathbf{v}_i$ is the radial peculiar velocity of halo i, which is measured with a normal error in its magnitude of δv, and n_p is the number of pairs in the survey volume for a given separation distance r. For the rest of the appendix, we drop the perpendicular subscript for convenience. So the measurement error in $\langle v_i v_j \rangle$ can be written as

$$
\begin{aligned}
\langle v_i v_j \rangle + \delta \langle v_i v_j \rangle &= \frac{1}{n_p} \Sigma_{ij}[v_i v_j + 2v_j \delta v_i + \delta v_i \delta v_j] \\
\delta \langle v_i v_j \rangle &= \frac{1}{n_p} \Sigma_{ij}[2v_j \delta v_i + \delta v_i \delta v_j] \\
&= \frac{1}{n_p} \Sigma[\delta(v^2) + (\delta v)^2] \tag{C.2}
\end{aligned}
$$

Similarly, the Poisson error is $\langle v_i v_j \rangle[\delta n_p/n_p] = \langle v_i v_j \rangle/\sqrt{n}_p$.

C.2   COSMIC VARIANCE ERROR

The cosmic covariance for the radial peculiar velocity correlation function between two bins $[r_p, z_p]$ and $[r_q, z_q]$, one of separation r_p at epoch z_p and the other of separation r_q at redshift z_q, can be written as

$$
\begin{aligned}
C^{\langle v_i v_j \rangle}(pq) &= \langle ((\langle v_i v_j \rangle (p) - \langle \langle \widehat{v_i v_j} \rangle \rangle (p)) (\langle v_i v_j \rangle (q) - \langle \widehat{v_i v_j} \rangle (q))) \rangle \\
&= \langle \widehat{v_i v_j} \rangle (p) \langle \widehat{v_i v_j} \rangle (q) - \langle v_i v_j \rangle (p) \langle v_i v_j \rangle (q) \quad \text{(C.3)}
\end{aligned}
$$

As in the case of $v_{ij}(r)$, we first derive an estimator for $v_i v_j(r)$. In linear theory, $v(k) = \delta(k)/k$, so $v(x) = \int d^3\mathbf{k}[\delta(k)/k]\exp(i\mathbf{k}\cdot\mathbf{x})$. Then an estimator $\widehat{v_i v_j}(r)$ measured at a separation $\mathbf{r}$ is

$$
\begin{aligned}
\widehat{v_i v_j}(r) &= \frac{1}{V(r)} \int d^3\mathbf{x}' W(x') v\mathbf{x}' \int d^3\mathbf{x} W(x) v(\mathbf{x}') \delta_D^3(\mathbf{x} - \mathbf{x}' - \mathbf{r}) \\
&= \int\int d^3\mathbf{k} d^3\mathbf{k}' \frac{\delta(\mathbf{k})\delta^*(\mathbf{k}')}{kk'} e^{-i\mathbf{k}\cdot\mathbf{r}'} h(\mathbf{k} - \mathbf{k}'). \quad \text{(C.4)}
\end{aligned}
$$

The only difference between Eq. (C.4) and Eq. (B.9) is the added factor of kk' in the denominator.

The expression for the radial peculiar velocity correlation function given in Eq. (2.20) consists of two terms, expressions for which are given in Eqs. (2.21) and (2.22). For simplicity, here we derive the cosmic covariance of the first term using the linear theory expression for the radial peculiar velocity correlation, Eq. (C.4); the derivation can be easily extended to the halo model expression for $\langle v_i v_j \rangle$ given in Eq. (2.20). As argued before, the second term in Eq. (2.20) can be neglected compared to the first term because $\xi(r)$ is negligible at separations of interest for $r > 30$ Mpc. The linear theory counterpart for Eq. (2.20) can be written as

$$
\langle \hat{T}_1 \rangle (r, a) = \left[H(a) \frac{d\ln D_a}{d\ln a} a D_a \right]^2 \frac{1}{3V(r)} \int_0^r d^3\mathbf{r}' \int\int d^3\mathbf{k} d^3\mathbf{k}' \frac{\delta(\mathbf{k})\delta^*(\mathbf{k}')}{kk'} e^{-i\mathbf{k}\cdot\mathbf{r}'} h(\mathbf{k} - \mathbf{k}', \mathbf{r}').
$$

$$\text{(C.5)}$$

Note that this integrand is similar to that in to Eq. (2.20), apart from the halo number density and bias factors. The factor of $1/3$ in Eq. (C.5), compared to Eq. (B.9), is because

only the radial peculiar velocity components are considered. Proceeding analogously to Eqs. (B.9) to (B.12), we obtain

$$C^{T_1}(pq) = a_p^2 a_q^2 D_{a_p}^2 D_{a_q}^2 H^2(a_p) H^2(a_q) \left[\frac{d\ln D_a}{d\ln a}\right]_{a_p}^2 \left[\frac{d\ln D_a}{d\ln a}\right]_{a_q}^2 \frac{64\pi^2}{V_\Omega^2} \int dk P(k)^2 \frac{j_1(kr_p)}{kr_p} \frac{j_1(kr_q)}{kr_q}$$

$$(C.6)$$

This is the cosmic covariance for the linear theory counterpart of Eq. (2.20). Including the extra halo model factors gives Eq. (3.8).

BIBLIOGRAPHY

N. Aghanim, K. M. Górski, and J.-L. Puget. How accurately can the SZ effect measure peculiar cluster velocities and bulk flows? *A&A*, 374:1–12, July 2001.

N. Aghanim, S. H. Hansen, and G. Lagache. Trouble for cluster parameter estimation from blind SZ surveys? *A&A*, 439:901–912, September 2005.

N. Aghanim, S. H. Hansen, S. Pastor, and D. V. Semikoz. Extraction of cluster parameters with future Sunyaev Zel'dovich observations. *Journal of Cosmology and Astro-Particle Physics*, 5:7–+, May 2003.

A. Albrecht, G. Bernstein, R. Cahn, W. L. Freedman, J. Hewitt, W. Hu, J. Huth, M. Kamionkowski, E. W. Kolb, L. Knox, J. C. Mather, S. Staggs, and N. B. Suntzeff. Report of the Dark Energy Task Force. *ArXiv Astrophysics e-prints*, September 2006.

S. W. Allen, R. W. Schmidt, H. Ebeling, A. C. Fabian, and L. van Speybroeck. Constraints on dark energy from Chandra observations of the largest relaxed galaxy clusters. *MNRAS*, 353:457–467, September 2004.

S. W. Allen, R. W. Schmidt, and A. C. Fabian. Cosmological constraints from the X-ray gas mass fraction in relaxed lensing clusters observed with Chandra. *MNRAS*, 334:L11–L15, August 2002.

J. M. Bardeen, J. R. Bond, N. Kaiser, and A. S. Szalay. The statistics of peaks of Gaussian random fields. *ApJ*, 304:15–61, May 1986.

B. A. Benson, S. E. Church, P. A. R. Ade, J. J. Bock, K. M. Ganga, J. R. Hinderks, P. D. Mauskopf, B. Philhour, M. C. Runyan, and K. L. Thompson. Peculiar Velocity Limits from Measurements of the Spectrum of the Sunyaev-Zeldovich Effect in Six Clusters of Galaxies. *ApJ*, 592:674–691, August 2003.

S. Bhattacharya and A. Kosowsky. Cosmological Constraints from Galaxy Cluster Velocity Statistics. *ApJ*, 659:L83–L86, April 2007.

J. J. Bialek, A. E. Evrard, and J. J. Mohr. Effects of Preheating on X-Ray Scaling Relations in Galaxy Clusters. *ApJ*, 555:597–612, July 2001.

J. R. Bond and G. Efstathiou. Cosmic background radiation anisotropies in universes dominated by nonbaryonic dark matter. *ApJ*, 285:L45–L48, October 1984.

H. Bondi. On spherically symmetrical accretion. *MNRAS*, 112:195–+, 1952.

H. Bondi and F. Hoyle. On the mechanism of accretion by stars. *MNRAS*, 104:273–+, 1944.

S. Borgani, F. Governato, J. Wadsley, N. Menci, P. Tozzi, T. Quinn, J. Stadel, and G. Lake. The effect of non-gravitational gas heating in groups and clusters of galaxies. *MNRAS*, 336:409–424, October 2002.

S. Borgani, G. Murante, V. Springel, A. Diaferio, K. Dolag, L. Moscardini, G. Tormen, L. Tornatore, and P. Tozzi. X-ray properties of galaxy clusters and groups from a cosmological hydrodynamical simulation. *MNRAS*, 348:1078–1096, March 2004.

C. Borys, S. Chapman, M. Halpern, and D. Scott. The Hubble Deep Field North SCUBA Super-map - I. Submillimetre maps, sources and number counts. *MNRAS*, 344:385–398, September 2003.

S. Chatterjee and A. Kosowsky. The Sunyaev-Zel'dovich Effect from Quasar Feedback. *ApJ*, 661:L113–L116, June 2007.

K. Coble, M. Bonamente, J. E. Carlstrom, K. Dawson, N. Hasler, W. Holzapfel, M. Joy, S. LaRoque, D. P. Marrone, and E. D. Reese. Radio Sources toward Galaxy Clusters at 30 GHz. *AJ*, 134:897–905, September 2007.

A. Cooray and R. Sheth. Halo models of large scale structure. *Phys. Rep.*, 372:1–129, December 2002.

K. Coppin, E. L. Chapin, A. M. J. Mortier, S. E. Scott, C. Borys, J. S. Dunlop, M. Halpern, D. H. Hughes, A. Pope, D. Scott, S. Serjeant, J. Wagg, D. M. Alexander, O. Almaini, I. Aretxaga, T. Babbedge, P. N. Best, A. Blain, S. Chapman, D. L. Clements, M. Crawford, L. Dunne, S. A. Eales, A. C. Edge, D. Farrah, E. Gaztañaga, W. K. Gear, G. L. Granato, T. R. Greve, M. Fox, R. J. Ivison, M. J. Jarvis, T. Jenness, C. Lacey, K. Lepage, R. G. Mann, G. Marsden, A. Martinez-Sansigre, S. Oliver, M. J. Page, J. A. Peacock, C. P. Pearson, W. J. Percival, R. S. Priddey, S. Rawlings, M. Rowan-Robinson, R. S. Savage, M. Seigar, K. Sekiguchi, L. Silva, C. Simpson, I. Smail, J. A. Stevens, T. Takagi, M. Vaccari, E. van Kampen, and C. J. Willott. The SCUBA Half-Degree Extragalactic Survey - II. Submillimetre maps, catalogue and number counts. *MNRAS*, 372:1621–1652, November 2006.

J. H. Croston, M. J. Hardcastle, and M. Birkinshaw. Evidence for radio-source heating of groups. *MNRAS*, 357:279–294, February 2005.

M. Davis and P. J. E. Peebles. On the integration of the BBGKY equations for the development of strongly nonlinear clustering in an expanding universe. *ApJS*, 34:425–450, August 1977.

S. DeDeo, D. N. Spergel, and H. Trac. The kinetic Sunyaev-Zel'dovitch effect as a dark energy probe. *ArXiv Astrophysics e-prints*, November 2005.

T. Di Matteo, J. Colberg, V. Springel, L. Hernquist, and D. Sijacki. Direct Cosmological Simulations of the Growth of Black Holes and Galaxies. *ApJ*, 676:33–53, March 2008.

T. Di Matteo, R. A. C. Croft, V. Springel, and L. Hernquist. Black Hole Growth and Activity in a Λ Cold Dark Matter Universe. *ApJ*, 593:56–68, August 2003.

T. Di Matteo, V. Springel, and L. Hernquist. Energy input from quasars regulates the growth and activity of black holes and their host galaxies. *Nature*, 433:604–607, February 2005.

A. Diaferio, S. Borgani, L. Moscardini, G. Murante, K. Dolag, V. Springel, G. Tormen, L. Tornatore, and P. Tozzi. Measuring cluster peculiar velocities with the Sunyaev-Zel'dovich effect: scaling relations and systematics. *MNRAS*, 356:1477–1488, February 2005a.

A. Diaferio, M. J. Geller, and K. J. Rines. Caustic and Weak-Lensing Estimators of Galaxy Cluster Masses. *ApJ*, 628:L97–L100, August 2005b.

J. Dunkley, E. Komatsu, M. R. Nolta, D. N. Spergel, D. Larson, G. Hinshaw, L. Page, C. L. Bennett, B. Gold, N. Jarosik, J. L. Weiland, M. Halpern, R. S. Hill, A. Kogut, M. Limon, S. S. Meyer, G. S. Tucker, E. Wollack, and E. L. Wright. Five-Year Wilkinson Microwave Anisotropy Probe (WMAP) Observations: Likelihoods and Parameters from the WMAP data. *ArXiv e-prints*, 803, March 2008.

G. Efstathiou, J. R. Bond, and S. D. M. White. COBE background radiation anisotropies and large-scale structure in the universe. *MNRAS*, 258:1P–6P, September 1992.

D. J. Eisenstein and M. Zaldarriaga. Correlations in the Spatial Power Spectra Inferred from Angular Clustering: Methods and Application to the Automated Plate Measuring Survey. *ApJ*, 546:2–19, January 2001.

V. R. Eke, J. F. Navarro, and C. S. Frenk. The Evolution of X-Ray Clusters in a Low-Density Universe. *ApJ*, 503:569–+, August 1998.

S. Ettori, S. Borgani, L. Moscardini, G. Murante, P. Tozzi, A. Diaferio, K. Dolag, V. Springel, G. Tormen, and L. Tornatore. Evolution at $z >= 0.5$ of the X-ray properties of simulated galaxy clusters: comparison with observational constraints. *MNRAS*, 354:111–122, October 2004.

S. Ettori, K. Dolag, S. Borgani, and G. Murante. The baryon fraction in hydrodynamical simulations of galaxy clusters. *MNRAS*, 365:1021–1030, January 2006.

A. E. Evrard. Formation and evolution of X-ray clusters - A hydrodynamic simulation of the intracluster medium. *ApJ*, 363:349–366, November 1990.

A. E. Evrard. The intracluster gas fraction in X-ray clusters - Constraints on the clustered mass density. *MNRAS*, 292:289–+, December 1997.

A. E. Evrard, T. J. MacFarland, H. M. P. Couchman, J. M. Colberg, N. Yoshida, S. D. M. White, A. Jenkins, C. S. Frenk, F. R. Pearce, J. A. Peacock, and P. A. Thomas. Galaxy Clusters in Hubble Volume Simulations: Cosmological Constraints from Sky Survey Populations. *ApJ*, 573:7–36, July 2002.

A. C. Fabian, J. S. Sanders, S. Ettori, G. B. Taylor, S. W. Allen, C. S. Crawford, K. Iwasawa, R. M. Johnstone, and P. M. Ogle. Chandra imaging of the complex X-ray core of the Perseus cluster. *MNRAS*, 318:L65–L68, November 2000.

P. G. Ferreira, R. Juszkiewicz, H. A. Feldman, M. Davis, and A. H. Jaffe. Streaming Velocities as a Dynamical Estimator of Omega. *ApJ*, 515:L1–L4, April 1999.

A. Finoguenov, T. H. Reiprich, and H. Böhringer. Details of the mass-temperature relation for clusters of galaxies. *A&A*, 368:749–759, March 2001.

M. R. Francis, R. Bean, and A. Kosowsky. Impact of systematic errors in Sunyaev Zel'dovich surveys of galaxy clusters. *Journal of Cosmology and Astro-Particle Physics*, 12:1–+, December 2005.

W. L. Freedman, B. F. Madore, B. K. Gibson, L. Ferrarese, D. D. Kelson, S. Sakai, J. R. Mould, R. C. Kennicutt, Jr., H. C. Ford, J. A. Graham, J. P. Huchra, S. M. G. Hughes, G. D. Illingworth, L. M. Macri, and P. B. Stetson. Final Results from the Hubble Space Telescope Key Project to Measure the Hubble Constant. *ApJ*, 553:47–72, May 2001.

C. S. Frenk, S. D. M. White, P. Bode, J. R. Bond, G. L. Bryan, R. Cen, H. M. P. Couchman, A. E. Evrard, N. Gnedin, A. Jenkins, A. M. Khokhlov, A. Klypin, J. F. Navarro, M. L. Norman, J. P. Ostriker, J. M. Owen, F. R. Pearce, U.-L. Pen, M. Steinmetz, P. A. Thomas, J. V. Villumsen, J. W. Wadsley, M. S. Warren, G. Xu, and G. Yepes. The Santa Barbara Cluster Comparison Project: A Comparison of Cosmological Hydrodynamics Solutions. *ApJ*, 525:554–582, November 1999.

K. Gorski. On the pattern of perturbations of the Hubble flow. *ApJ*, 332:L7–L11, September 1988.

M. G. Haehnelt and M. Tegmark. Using the Kinematic Sunyaev-Zeldovich effect to determine the peculiar velocities of clusters of galaxies. *MNRAS*, 279:545–+, March 1996.

T. Hamana, I. Kayo, N. Yoshida, Y. Suto, and Y. P. Jing. Modelling peculiar velocities of dark matter haloes. *MNRAS*, 343:1312–1318, August 2003.

S. H. Hansen. Cluster temperature profiles and Sunyaev-Zeldovich observations. *MNRAS*, 351:L5–L8, June 2004.

S. Heinz, Y.-Y. Choi, C. S. Reynolds, and M. C. Begelman. Chandra ACIS-S Observations of Abell 4059: Signs of Dramatic Interaction between a Radio Galaxy and a Galaxy Cluster. *ApJ*, 569:L79–L82, April 2002.

C. Hernández-Monteagudo, L. Verde, R. Jimenez, and D. N. Spergel. Correlation Properties of the Kinematic Sunyaev-Zel'dovich Effect and Implications for Dark Energy. *ApJ*, 643: 598–615, June 2006.

L. Hernquist and V. Springel. An analytical model for the history of cosmic star formation. *MNRAS*, 341:1253–1267, June 2003.

D. W. Hogg. Distance measures in cosmology. *ArXiv Astrophysics e-prints*, May 1999.

G. Holder, Z. Haiman, and J. J. Mohr. Constraints on Ω_m, Ω_K, and σ_8 from Galaxy Cluster Redshift Distributions. *ApJ*, 560:L111–L114, October 2001.

G. P. Holder. Measuring Cluster Peculiar Velocities and Temperatures at Centimeter and Millimeter Wavelengths. *ApJ*, 602:18–25, February 2004.

F. Hoyle and R. A. Lyttleton. The effect of interstellar matter on climatic variation. In *Proceedings of the Cambridge Philosophical Society*, volume 35 of *Proceedings of the Cambridge Philosophical Society*, pages 405–+, 1939.

A. Jenkins, C. S. Frenk, S. D. M. White, J. M. Colberg, S. Cole, A. E. Evrard, H. M. P. Couchman, and N. Yoshida. The mass function of dark matter haloes. *MNRAS*, 321: 372–384, February 2001.

N. N. Jetha, T. J. Ponman, M. J. Hardcastle, and J. Croston. AGN heating in galaxy groups: A statistical study. *ArXiv Astrophysics e-prints*, December 2006.

N. Kaiser. Evolution of clusters of galaxies. *ApJ*, 383:104–111, December 1991.

N. Katz, D. H. Weinberg, and L. Hernquist. Cosmological Simulations with TreeSPH. *ApJS*, 105:19–+, July 1996.

S. T. Kay, P. A. Thomas, and T. Theuns. The impact of galaxy formation on X-ray groups. *MNRAS*, 343:608–618, August 2003.

A. Khalatyan, A. Cattaneo, M. Schramm, S. Gottlöber, M. Steinmetz, and L. Wisotzki. Is AGN feedback necessary to form red elliptical galaxies? *MNRAS*, 387:13–30, June 2008.

L. Knox, G. P. Holder, and S. E. Church. Effects of Submillimeter and Radio Point Sources on the Recovery of Sunyaev-Zel'dovich Galaxy Cluster Parameters. *ApJ*, 612:96–107, September 2004.

E. Komatsu and U. Seljak. The Sunyaev-Zel'dovich angular power spectrum as a probe of cosmological parameters. *MNRAS*, 336:1256–1270, November 2002.

A. Kosowsky. The Atacama Cosmology Telescope. *New Astronomy Review*, 47:939–943, December 2003.

A. Kosowsky. The Atacama Cosmology Telescope project: A progress report. *New Astronomy Review*, 50:969–976, December 2006.

M. Lima and W. Hu. Self-calibration of cluster dark energy studies: Counts in cells. *Phys. Rev. D*, 70(4):043504–+, August 2004.

M. Lima and W. Hu. Self-calibration of cluster dark energy studies: Observable-mass distribution. *Phys. Rev. D*, 72(4):043006–+, August 2005.

M. Lima and W. Hu. Photometric Redshift Requirements for Self-Calibration of Cluster Dark Energy Studies. *ArXiv e-prints*, 709, September 2007.

Y.-T. Lin and J. J. Mohr. Radio Sources in Galaxy Clusters: Radial Distribution, and 1.4 GHz and K-band Bivariate Luminosity Function. *ApJS*, 170:71–94, May 2007.

L. M. Lubin, R. Cen, N. A. Bahcall, and J. P. Ostriker. The Baryon Fraction and Velocity-Temperature Relation in Galaxy Clusters: Models versus Observations. *ApJ*, 460:10–+, March 1996.

S. Majumdar and J. J. Mohr. Self-Calibration in Cluster Studies of Dark Energy: Combining the Cluster Redshift Distribution, the Power Spectrum, and Mass Measurements. *ApJ*, 613:41–50, September 2004.

M. Maturi, L. Moscardini, P. Mazzotta, K. Dolag, and G. Tormen. The importance of merging activity for the kinetic polarization of the Sunyaev-Zel'dovich signal from galaxy clusters. *A&A*, 475:71–81, November 2007.

C. A. Metzler and A. E. Evrard. A simulation of the intracluster medium with feedback from cluster galaxies. *ApJ*, 437:564–583, December 1994.

J. J. Mohr, B. Mathiesen, and A. E. Evrard. Properties of the Intracluster Medium in an Ensemble of Nearby Galaxy Clusters. *ApJ*, 517:627–649, June 1999.

J. J. Monaghan. Smoothed particle hydrodynamics. *ARA&A*, 30:543–574, 1992.

O. Muanwong, P. A. Thomas, S. T. Kay, and F. R. Pearce. The effect of cooling and preheating on the X-ray properties of clusters of galaxies. *MNRAS*, 336:527–540, October 2002.

D. Nagai, A. V. Kravtsov, and A. Kosowsky. Effect of Internal Flows on Sunyaev-Zeldovich Measurements of Cluster Peculiar Velocities. *ApJ*, 587:524–532, April 2003.

D. Nagai, A. V. Kravtsov, and A. Vikhlinin. Effects of Galaxy Formation on Thermodynamics of the Intracluster Medium. *ApJ*, 668:1–14, October 2007.

B. B. Nath and S. Roychowdhury. Heating of the intracluster medium by quasar outflows. *MNRAS*, 333:145–155, June 2002.

J. F. Navarro, C. S. Frenk, and S. D. M. White. Simulations of X-ray clusters. *MNRAS*, 275:720–740, August 1995.

P. E. J. Nulsen, B. R. McNamara, M. W. Wise, and L. P. David. The Cluster-Scale AGN Outburst in Hydra A. *ApJ*, 628:629–636, August 2005.

A. Peel and L. Knox. Using galaxy cluster peculiar velocities to constrain cosmological parameters. *Nuclear Physics B Proceedings Supplements*, 124:83–86, July 2003.

A. C. Peel. Mass selection bias in galaxy cluster peculiar velocities from the kinetic Sunyaev-Zel'dovich effect. *MNRAS*, 365:1191–1202, February 2006.

E. Pointecouteau, M. Arnaud, and G. W. Pratt. The structural and scaling properties of nearby galaxy clusters. I. The universal mass profile. *A&A*, 435:1–7, May 2005.

T. J. Ponman, A. J. R. Sanderson, and A. Finoguenov. The Birmingham-CfA cluster scaling project - III. Entropy and similarity in galaxy systems. *MNRAS*, 343:331–342, July 2003.

P. Popesso, A. Biviano, H. Böhringer, M. Romaniello, and W. Voges. RASS-SDSS galaxy cluster survey. III. Scaling relations of galaxy clusters. *A&A*, 433:431–445, April 2005.

M. Righi, C. Hernández-Monteagudo, and R. A. Sunyaev. The clustering of merging star-forming haloes: dust emission as high frequency arcminute CMB foreground. *A&A*, 478: 685–700, February 2008.

K. Rines, M. J. Geller, M. J. Kurtz, and A. Diaferio. CAIRNS: The Cluster and Infall Region Nearby Survey. I. Redshifts and Mass Profiles. *AJ*, 126:2152–2170, November 2003.

M. Roncarelli, L. Moscardini, S. Borgani, and K. Dolag. The Sunyaev-Zel'dovich effects from a cosmological hydrodynamical simulation: large-scale properties and correlation with the soft X-ray signal. *MNRAS*, 378:1259–1269, July 2007.

D. H. Rudd, A. R. Zentner, and A. V. Kravtsov. Effects of Baryons and Dissipation on the Matter Power Spectrum. *ApJ*, 672:19–32, January 2008.

J. Ruhl, P. A. R. Ade, J. E. Carlstrom, H.-M. Cho, T. Crawford, M. Dobbs, C. H. Greer, N. w. Halverson, W. L. Holzapfel, T. M. Lanting, A. T. Lee, E. M. Leitch, J. Leong, W. Lu, M. Lueker, J. Mehl, S. S. Meyer, J. J. Mohr, S. Padin, T. Plagge, C. Pryke, M. C. Runyan, D. Schwan, M. K. Sharp, H. Spieler, Z. Staniszewski, and A. A. Stark. The South Pole Telescope. In C. M. Bradford, P. A. R. Ade, J. E. Aguirre, J. J. Bock, M. Dragovan, L. Duband, L. Earle, J. Glenn, H. Matsuhara, B. J. Naylor, H. T. Nguyen, M. Yun, and J. Zmuidzinas, editors, *Millimeter and Submillimeter Detectors for Astronomy II. Edited by Jonas Zmuidzinas, Wayne S. Holland and Stafford Withington Proceedings of the SPIE, Volume 5498, pp. 11-29 (2004).*, volume 5498 of *Presented at the Society of Photo-Optical Instrumentation Engineers (SPIE) Conference*, pages 11–29, October 2004.

A. J. R. Sanderson, A. Finoguenov, and J. J. Mohr. Possible AGN Shock Heating in the Cool-Core Galaxy Cluster Abell 478. *ApJ*, 630:191–205, September 2005.

A. J. R. Sanderson, T. J. Ponman, A. Finoguenov, E. J. Lloyd-Davies, and M. Markevitch. The Birmingham-CfA cluster scaling project - I. Gas fraction and the $M - T_X$ relation. *MNRAS*, 340:989–1010, April 2003.

E. Scannapieco, J. Silk, and R. Bouwens. AGN Feedback Causes Downsizing. *ApJ*, 635: L13–L16, December 2005.

E. Scannapieco, R. J. Thacker, and H. M. P. Couchman. Measuring AGN Feedback with the Sunyaev-Zel'dovich Effect. *ApJ*, 678:674–685, May 2008.

K. S. Scott, J. E. Austermann, T. A. Perera, G. W. Wilson, I. Aretxaga, J. J. Bock, D. H. Hughes, Y. Kang, S. Kim, P. D. Mauskopf, D. B. Sanders, N. Scoville, and M. S. Yun. AzTEC millimetre survey of the COSMOS field - I. Data reduction and source catalogue. *MNRAS*, 385:2225–2238, April 2008.

N. Sehgal, A. Kosowsky, and G. Holder. Constrained Cluster Parameters from Sunyaev-Zel'dovich Observations. *ApJ*, 635:22–34, December 2005.

N. Sehgal, H. Trac, K. Huffenberger, and P. Bode. Microwave Sky Simulations and Projections for Galaxy Cluster Detection with the Atacama Cosmology Telescope. *ApJ*, 664: 149–161, July 2007.

N. I. Shakura and R. A. Syunyaev. Black holes in binary systems. Observational appearance. *A&A*, 24:337–355, 1973.

R. K. Sheth and A. Diaferio. Peculiar velocities of galaxies and clusters. *MNRAS*, 322: 901–917, April 2001.

R. K. Sheth, A. Diaferio, L. Hui, and R. Scoccimarro. On the streaming motions of haloes and galaxies. *MNRAS*, 326:463–472, September 2001a.

R. K. Sheth, L. Hui, A. Diaferio, and R. Scoccimarro. Linear and non-linear contributions to pairwise peculiar velocities. *MNRAS*, 325:1288–1302, August 2001b.

D. Sijacki, V. Springel, T. di Matteo, and L. Hernquist. A unified model for AGN feedback in cosmological simulations of structure formation. *MNRAS*, 380:877–900, September 2007.

D. N. Spergel, R. Bean, O. Doré, M. R. Nolta, C. L. Bennett, J. Dunkley, G. Hinshaw, N. Jarosik, E. Komatsu, L. Page, H. V. Peiris, L. Verde, M. Halpern, R. S. Hill, A. Kogut, M. Limon, S. S. Meyer, N. Odegard, G. S. Tucker, J. L. Weiland, E. Wollack, and E. L. Wright. Three-Year Wilkinson Microwave Anisotropy Probe (WMAP) Observations: Implications for Cosmology. *ApJS*, 170:377–408, June 2007.

D. N. Spergel, L. Verde, H. V. Peiris, E. Komatsu, M. R. Nolta, C. L. Bennett, M. Halpern, G. Hinshaw, N. Jarosik, A. Kogut, M. Limon, S. S. Meyer, L. Page, G. S. Tucker, J. L.

Weiland, E. Wollack, and E. L. Wright. First-Year Wilkinson Microwave Anisotropy Probe (WMAP) Observations: Determination of Cosmological Parameters. *ApJS*, 148:175–194, September 2003.

V. Springel. The cosmological simulation code GADGET-2. *MNRAS*, 364:1105–1134, December 2005.

V. Springel and L. Hernquist. Cosmological smoothed particle hydrodynamics simulations: a hybrid multiphase model for star formation. *MNRAS*, 339:289–311, February 2003a.

V. Springel and L. Hernquist. Cosmological smoothed particle hydrodynamics simulations: a hybrid multiphase model for star formation. *MNRAS*, 339:289–311, February 2003b.

R. A. Sunyaev and I. B. Zeldovich. Microwave background radiation as a probe of the contemporary structure and history of the universe. *ARA&A*, 18:537–560, 1980.

E. Tago, J. Einasto, E. Saar, E. Tempel, M. Einasto, J. Vennik, and V. Müller. Groups of galaxies in the SDSS Data Release 5. A group-finder and a catalogue. *A&A*, 479:927–937, March 2008.

M. Takada and S. Bridle. Probing dark energy with cluster counts and cosmic shear power spectra: including the full covariance. *ArXiv e-prints*, 705, May 2007.

M. Tegmark, M. Zaldarriaga, and A. J. Hamilton. Towards a refined cosmic concordance model: Joint 11-parameter constraints from the cosmic microwave background and large-scale structure. *Phys. Rev. D*, 63(4):043007–+, February 2001.

R. J. Thacker, E. Scannapieco, and H. M. P. Couchman. Quasars: What Turns Them Off? *ApJ*, 653:86–100, December 2006.

P. Valageas and J. Silk. The entropy history of the universe. *A&A*, 350:725–742, October 1999.

R. Valdarnini. Iron abundances and heating of the intracluster medium in hydrodynamical simulations of galaxy clusters. *MNRAS*, 339:1117–1134, March 2003.

A. Vikhlinin, A. Kravtsov, W. Forman, C. Jones, M. Markevitch, S. S. Murray, and L. Van Speybroeck. Chandra Sample of Nearby Relaxed Galaxy Clusters: Mass, Gas Fraction, and Mass-Temperature Relation. *ApJ*, 640:691–709, April 2006.

S. D. M. White, J. F. Navarro, A. E. Evrard, and C. S. Frenk. The Baryon Content of Galaxy Clusters - a Challenge to Cosmological Orthodoxy. *Nature*, 366:429–+, December 1993.

J. P. Willis, F. Pacaud, I. Valtchanov, M. Pierre, T. Ponman, A. Read, S. Andreon, B. Altieri, H. Quintana, S. D. Santos, M. Birkinshaw, M. Bremer, P.-A. Duc, G. Galaz, E. Gosset, L. Jones, and J. Surdej. Erratum: The XMM Large-Scale Structure survey: an initial

sample of galaxy groups and clusters to a redshift $z < 0.6$. *MNRAS*, 364:751–752, December 2005.

G. W. Wilson, I. Aretxaga, D. Hughes, H. Ezawa, J. E. Austermann, S. Doyle, I. Hernandez-Curiel, R. Kawabe, T. Kitayama, K. Kohno, A. Kuboi, H. Matsuo, P. D. Mauskopf, Y. Murakoshi, A. Montana, P. Natarajan, T. Oshima, N. Ota, T. Perera, J. Rand, K. S. Scott, K. Tanaka, M. Tsuboi, C. C. Williams, and M. S. Yun. An ultra-bright, dust-obscured, millimeter-galaxy beyond the Bullet Cluster (1E0657-56). *ArXiv e-prints*, 803, March 2008.

A. R. Zentner. The Excursion Set Theory of Halo Mass Functions, Halo Clustering, and Halo Growth. *International Journal of Modern Physics D*, 16:763–815, 2007.